Single-photon metrology with superconducting nanowire single-photon detectors

Catherine Rose Fitzpatrick

A thesis submitted for the qualification of

Doctor of Engineering

Heriot-Watt University

School of Engineering and Physical Sciences

September 2013

Abstract

Single-photon sources and detectors underpin the development of quantum photonic technologies. This thesis presents research into single-photon devices with a focus on telecom wavelengths.

A two-channel superconducting nanowire single-photon detector (SNSPD) system was constructed and characterised. It provides free-running single-photon detection at telecom wavelengths with low dark counts and timing jitter below 90 ps FWHM. The system detection efficiency at 1310 nm is 1 % with a 1 kHz dark count rate, which was competitive when the SNSPD was built in 2009. In this work, the low timing jitter of the SNSPD was beneficial to the development of a two-photon interference experiment.

Experiments were carried out with single-photon sources based on self-assembled InAs/GaAs quantum dots in micropillar cavities. Preliminary measurements of the second-order correlation function gave $g^{(2)}(\tau = 0) = 0.12 \pm 0.04$ with above-band excitation and $g^{(2)}(\tau = 0) = 0.07 \pm 0.05$ with near-resonant excitation. These values agree with recent papers reporting improved measurements with near-resonant excitation. Irreparable damage to the sample prevented further investigation.

This thesis also presents the design, construction and characterisation of a high-resolution single-photon spectrometer for telecom wavelengths. The instrument, a scanning Fabry-Pérot interferometer, was optimised for the characterisation of quantum photonic sources. It has a spectral resolution of ~ 550 MHz and a free spectral range of (119.0 ± 0.4) GHz.

Acknowledgements

The work presented in thesis would not have been possible without the advice and support of several people. I would like to express my deepest gratitude to:

Prof. Robert Hadfield, whose insights and positive outlook over the last four years enabled me to overcome many challenging obstacles;

Dr. Alastair Sinclair, whose persistent attention to detail taught me how to back problems into a corner and improved my approach to both lab work and scientific writing;

Dr. Chandra Mouli Natarajan, for invaluable guidance and practical advice while I was building the SNSPD system for NPL;

Dr. Mike Tanner, for useful discussions about photon detection and for facing the challenge of proofreading this thesis!

Dr. Jessica Cheung, for spending time with me in the lab and helping me to keep smiling with her cheerful encouragement;

Dr. Stephen Webster, for his patience and clarity in our discussions on cavity stabilisation and temperature control;

The numerous staff at NPL and Heriot-Watt University who have helped me design, construct, repair, purchase or locate innumerable pieces of equipment;

All the people whose friendship and support have brought me here with my sanity (relatively) intact, notably my EngD compatriots Lucy and Mhairi, with whom I have shared many ups, downs and interesting cocktails. The last four years have been a unique period of learning and development; thanks to these people and many more, I am proud of what I have achieved and am looking forward to the next adventure.

ACADEMIC REGISTRY
Research Thesis Submission

Name*:*	Catherine Rose Fitzpatrick		
School/PGI:	Engineering and Physical Sciences		
Version: *(i.e. First, Resubmission, Final)*	Final	Degree Sought (Award **and** Subject area)	Doctor of Engineering in Optics and Photonics

Declaration

In accordance with the appropriate regulations I hereby submit my thesis and I declare that:

1) the thesis embodies the results of my own work and has been composed by myself
2) where appropriate, I have made acknowledgement of the work of others and have made reference to work carried out in collaboration with other persons
3) the thesis is the correct version of the thesis for submission and is the same version as any electronic versions submitted*.
4) my thesis for the award referred to, deposited in the Heriot-Watt University Library, should be made available for loan or photocopying and be available via the Institutional Repository, subject to such conditions as the Librarian may require
5) I understand that as a student of the University I am required to abide by the Regulations of the University and to conform to its discipline.

* *Please note that it is the responsibility of the candidate to ensure that the correct version of the thesis is submitted.*

Signature of Candidate*:*		Date:	

Submission

Submitted By *(name in capitals):*	
Signature of Individual Submitting:	
Date Submitted:	

For Completion in the Student Service Centre (SSC)

Received in the SSC by *(name in capitals):*			
Method of Submission *(Handed in to SSC; posted through internal/external mail):*			
*E-thesis Submitted (**mandatory for final theses)***			
Signature:		Date:	

Please note this form should bound into the submitted thesis.

Updated February 2008, November 2008, February 2009, January 2011

Contents

List of Figures

List of Tables

List of Abbreviations

cps	Counts per second
CTE	Coefficient of thermal expansion
CW	Continuous wave (laser emission)
FSR	Free spectral range
FWHM	Full width at half maximum
PTFE	Polytetrafluoroethylene
QD	Quantum dot
QKD	Quantum key distribution
SFPI	Scanning Fabry-Pérot interferometer
SNSPD	Superconducting nanowire single-photon detector
SPAD	Single-photon avalanche diode
SPDC	Spontaneous parametric downconversion

List of Symbols

D	Dark count rate
$\eta_{absorption}$	Photon absorption efficiency
$\eta_{coupling}$	Coupling efficiency (*e.g.* coupling light to active area of detector)
$\eta_{collection}$	Photon collection efficiency
$\eta_{emission}$	Photon emission efficiency
η_{QE}	Quantum efficiency
η_{source}	Source efficiency ($= \eta_{emission} \times \eta_{collection}$)
η_{SDE}	System detection efficiency ($= \eta_{absorption} \times \eta_{coupling} \times \eta_{QE}$)
F	Cavity finesse
L	Cavity length
$\Delta\nu$	Spectral linewidth
R	Reflectivity
Rc	Radius of curvature of spherical mirror
λ	Wavelength

Chapter 1

Introduction

Quantum technology seeks to exploit quantum mechanics in a range of high-impact applications. Revolutionary proposals have inspired fields of research including quantum key distribution [1], quantum computing [2] and quantum metrology [3]. Progress is being made; a practically useful quantum computer might lie in the future, but systems that implement quantum key distribution (QKD) are commercially available today [4]. A wide variety of quantum systems are being investigated for their potential use in quantum technologies, including trapped atoms [5], quantum dots [6] and photons [7]. The work in this thesis focuses on photonic quantum technologies.

Figure 1.1 illustrates the explosion of activity in this research area over the last two decades. The importance of photons is indicated by the concurrent increase in publications concerning quantum technologies and single-photon devices. Photons provide unconditionally secure encryption in quantum key distribution [1], facilitate linear optical quantum computing [8] and surpass the classical limits on uncertainty in quantum metrology [3]. While specific requirements vary, most photonic quantum technologies need high-performance sources and detectors that operate at the single-photon level. The role of single-photon metrology is to assess that performance and therefore the suitability of devices for specific applications. The need for a standardised measurement framework to support the commercial adoption of QKD has been recognised in recent literature [9]; other quantum technologies will also

benefit from the development of clear standards as they mature and approach the marketplace. The work presented in this thesis contributes to the development of single-photon metrology at NPL.

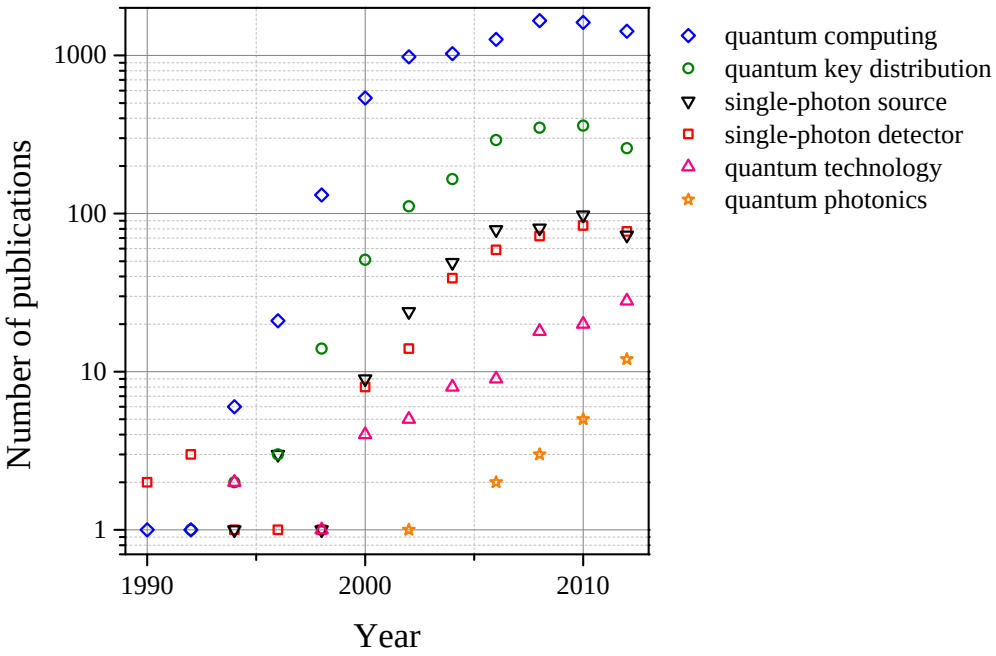

Figure 1.1: **Publication trends in quantum technology.** Plots show the annual publication yield for specific ISI Web of Knowledge search terms. The increase in publications on quantum computing and quantum key distribution over the last twenty years is concurrent with a rise in the number of papers about single-photon devices. The prevalence of newer terms 'quantum photonics' and 'quantum technology' has also increased over the last decade.

1.1 Motivation: Photonic quantum technologies

The development of high-performance single-photon sources and detectors has been driven by the goal of realising photonic quantum technologies. The efficiency and timing characteristics of these devices directly affect the accuracy and speed with which quantum information can be processed. A range of other properties specific either to sources or detectors can also be crucial, including the similarity between photons successively emitted by a source or the probability of false events in the detector. The following sections outline key applications of quantum photonics with a focus on the performance they require from single-photon devices.

1.1.1 Quantum key distribution

At a time when 10 % of UK retail purchases are made online [10], encryption is an assumed and integral part of modern society. The security of most modern encryption is based on the difficulty of factorising extremely large numbers (*e.g.* RSA encryption [11]). This could potentially be compromised by sufficiently powerful computers [12]. Superior security can be achieved with the 'one time pad' cipher; proposed by Vernam in 1926, it employs a single-use key that is as long as the message itself [1]. This is the only method of encryption that is provably secure - as long as the key itself is secure [1]. For information of the utmost secrecy, the key can be transported via courier. However, couriers can be be corrupted or intercepted, and are not practical for all situations (*e.g.* supplying keys to a satellite). QKD is an attractive alternative because it can distribute secure keys through optical fibre or free space by encoding bits on single photons. The security of this method is based on the quantum no cloning theorem, which states that it is not possible to make a perfect copy of an unknown quantum state [13]. To determine the value of a bit, an eavesdropper must measure the photon and transmit another in its place, but the measurement process introduces errors. QKD utilises this property to detect eavesdroppers and therefore verify that generated keys that are known only by the sender and receiver [1].

Proposed in 1984 by Bennett and Brassard [14], QKD associates binary integers with intrinsic properties such as a photon's phase or polarisation. A secure key can be distilled from transmitted photons using a number of different protocols [1]. The first protocol, now referred to as BB84, is best explained with a simple example. Two parties, Alice and Bob, decide to share a secure quantum key using polarisation-encoded photons. They agree on a scheme that assigns binary values to polarisation states in two non-orthogonal bases, as shown in Figure 1.2. Either basis can then be used for encoding. The value of a polarisation-encoded photon can be determined by placing detectors at both outputs of a polarising beam splitter, as shown in Figure 1.3. The photons must be encoded and measured in the same basis to accurately determine the value; when the incorrect basis is used, the photon has equal probability of registering as zero or one.

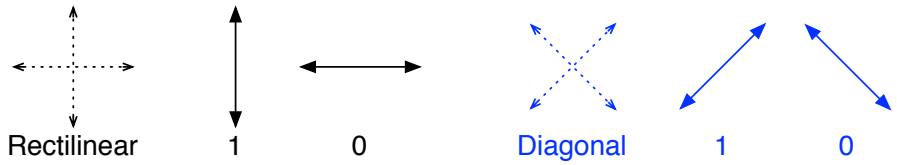

Figure 1.2: **Example of QKD encoding assignments.** Rectlinear and diagonal bases can be used in polarisation-encoded QKD. The two orthogonal states in each basis are assigned binary values for use in key generation.

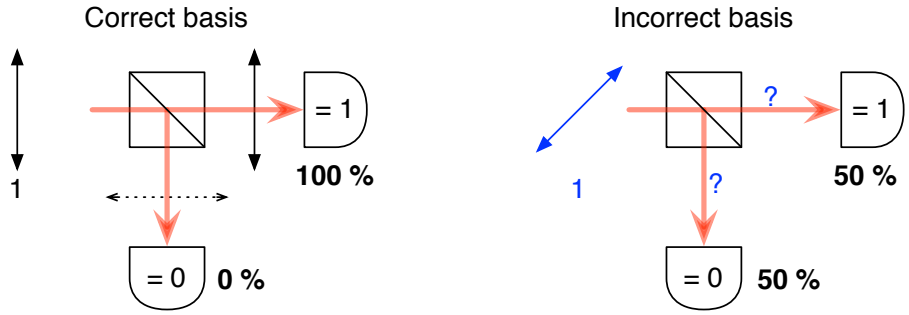

Figure 1.3: **Measurement of polarisation-encoded photons.** A polarising beam splitter enables Bob to determine the encoded values based on where photons are detected. This is only accurate when the measurement is conducted in the correct basis. When the incorrect basis is used, the photon enters either detector with equal probability.

Alice and Bob share a secure key using the process shown in Figure 1.4. Alice encodes bits onto individual photons and sends them to Bob, randomly selecting one of the two bases each time. Bob measures the photons to determine the bit values, also randomly selecting a basis. At first this seems like a bad idea; Bob will select the opposite basis to Alice half of the time, and when he does half of those measurements will be wrong, producing a 25 % error rate in the raw key. However, Alice and Bob communicate over a classical channel after the photons have been transmitted and compare the bases they used. This allows them to throw away any bits that were not measured in the same basis. Under perfect conditions, the retained bits (referred to as the 'sifted key') would be identical. In practice, imperfect conditions result in a non-zero error rate, which can be measured by comparing and discarding a subset of the detected bits over a classical channel. The error rate can be accounted for by determining the contributions made by system components. For example, bits can be lost due to imperfect photon transmission and detection, and incorrect values can be caused by false detection events. While security can be preserved in

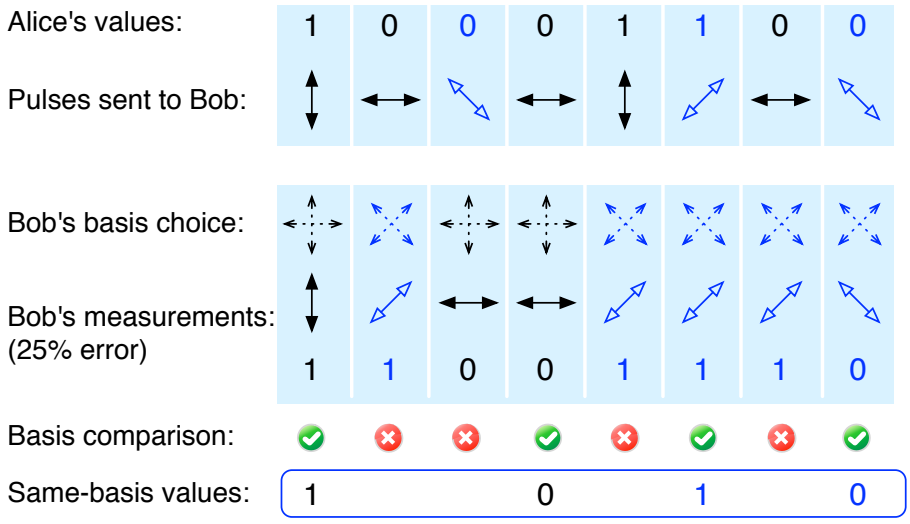

Figure 1.4: **QKD example with polarised photons.** Alice sends encoded photons to Bob, who measures each one with a random choice of the two bases. The values where Alice and Bob used the same basis are retained to form a sifted key.

these scenarios, part of the key must be sacrificed for error correction so the cost is a lower secure key transmission rate [15]. Eavesdropping also introduces errors; like Bob, an eavesdropper (Eve) must select a measurement basis and has a 25 % chance of measuring incorrect values. She then sends photons encoded with these values onwards to Bob. The resulting increase in error rate alerts Alice and Bob to her presence, allowing them to discard the values instead of using them to generate a key. It can be shown [1] that if the error rate is below 11 %, Alice and Bob can be confident that the values have not been compromised by an eavesdropper. This is achievable; several QKD experiments have achieved error rates below 5 % [16, 17, 18].

If the bits were encoded on multi-photon pulses, Eve could pick off part of the pulse with a beamsplitter and send the rest to Bob without any additional errors. This is called a 'photon-splitting attack'. Initially, it was thought that the only way to protect against this was to use single-photon sources [19]. However, the more recent decoy state protocol achieves unconditional security using attenuated laser pulses with different mean photon numbers around the level of 0.5 photons per pulse [20, 21]. While single-photon detectors are still required in these systems, this simplification of the source requirements is attractive for commercial implementations.

Since its proposal in 1984, QKD has been successfully demonstrated in free space and optical fibre both with attenuated lasers [17, 22] and single-photon sources [23, 24]. QKD experiments have been carried out at visible [25, 26] and telecom wavelengths [16, 17] and with several different protocols [14, 20, 27, 28]. The ultimate goal is to distribute a secure key quickly, accurately and over large distances. Secure key rates above 1 Mbit/s over 20 km of optical fibre have been achieved [17], but the rate decreases with fibre length due to increased attenuation. In addition to improving detection efficiency and reducing error rates, routes to increasing transmission distance include the use of satellites [26, 29] and quantum repeaters [30]. Current designs for quantum repeaters require single-photon sources [31], which could affect the suitability of attenuated lasers for long-distance QKD and increase the demand for high-performance single-photon sources.

One requirement that is common to all practical implementations of QKD is a precise understanding of the performance of the components. This is especially important for commercial systems. Current efforts to develop unified international standards for QKD security and associated device characterisation are described in Ref. [9]. To detect eavesdroppers and provide usable keys, the contributions made by apparatus to bit error rates need to be characterised and minimised. For example, the rate of false events in the detector needs to be known. Timing properties are important for achieving rapid key transmission. Detection efficiency can also affect the key rate because missing bits increases the time required to produce a specific key length. It is also important to understand and account for the possibility of 'blinding attacks', where an eavesdropper could potentially control the bit stream received by Bob's detectors using tailored bright illumination [32]. It must also be ensured that encoding techniques do not unintentionally affect other properties of the photons, for example their spectra; information must not leak into side channels as this would compromise the security of the transmitted key by providing the eavesdropper with an alternative route to gaining information about the key [30]. In summary, accurate device characterisation is crucial to ensuring that practical QKD systems achieve unconditional security.

1.1.2 Quantum computing

Quantum computing represents a paradigm shift for algorithm optimisation; the replacement of classical bits with quantum equivalents ('qubits') allows a system to exist in multiple states simultaneously. This changes the way that algorithms scale such that some can be achieved exponentially faster [13]. Shor's factoring algorithm is an important example of this because the ability to rapidly factorise large numbers would compromise much of current encryption [15]. Progress in quantum computing therefore also drives the development of QKD. This section briefly describes quantum computing in relation to photonic devices.

The main resource that is used in quantum computing is entanglement. Entangled objects are correlated in such a way that measuring one reveals the state of the other. In quantum mechanical terms, this means that the wavefunction describing the two objects is not separable [33]. This is memorably illustrated by the famous thought experiment about Schrödinger's cat (see Figure 1.5); by placing a cat in a box with a radioactive source that is connected to a cyanide trigger, radioactive decay and felicide become inextricably linked [15]. Before lifting the lid, the state inside the box can only be described as a probabilistic combination of both eventualities - an entangled state. Once opened, it is possible to determine if the source has decayed by observing the condition of the cat.

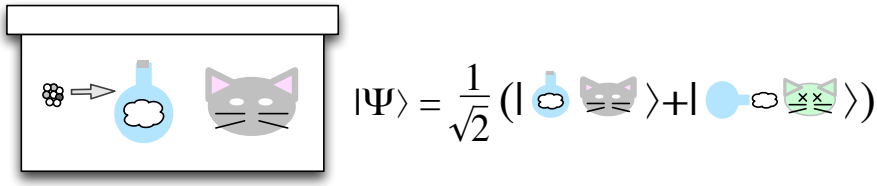

Figure 1.5: **Schrödinger's entangled cat.** In this famous thought experiment, a cat is placed in a box with a radioactive source whose decay triggers the release of cyanide. This entangles the state of the cat with that of the source; at the point where there is a 50 % probability that the source has decayed, the state $|\Psi\rangle$ takes the illustrated form.

Under the right conditions, entangled photon pairs can be generated by radiative cascades from excited quantised systems. Conservation requirements can produce cascades of two photons that are always opposite in polarisation, but where the polarisation of the individual photons varies randomly. The polarisations of the two

photons are therefore correlated - the polarisation of one photon can be determined by measuring the other. Similarly to the state depicted in Figure 1.5, this could be expressed in the rectilinear basis as:

$$|\Psi\rangle = \frac{1}{\sqrt{2}}(|H_1V_2\rangle + |V_1H_2\rangle) \tag{1.1}$$

where subscripts 1 and 2 refer to each of the two photons. The entangled state in Equation 1.1 exists in both polarisation configurations with equal probability until it is measured. If binary integers were to be associated with the two polarisations, then Equation 1.1 would represent a two-qubit state containing equal components of the configurations $|10\rangle$ and $|01\rangle$. This is a simple illustration of how qubits made from entangled states can simultaneously exist in multiple configurations.

The theoretical development of quantum computing extends far beyond what is currently possible in the laboratory [13]. The conditions required to make a real quantum computer are an enormous technical challenge; several candidate systems are being intensively researched, but it is not clear if any will achieve computation on a sufficiently large scale to be useful [2]. Nevertheless, photons are one of the main contenders for realising a practical, scalable quantum computer [34], as their speed and minimal interaction with the environment helps to preserve entanglement.

In addition to entanglement, another requirement of many quantum computing schemes is the ability to make qubits interact at specific junctures; this was a major obstacle for photonic schemes until linear optical quantum computing was proposed in 2001 [8]. Instead of forcing photons to interact at a specific point (which is difficult, perhaps impossible [2]), this scheme uses specific paths between single-photon sources and detectors to allow the required states to be post-selected based on detection events. Systems employing this technique are being developed; the most advanced demonstrations of Shor's factoring algorithm to date with linear optical systems have successfully factorised N = 15 [35] and N = 21 [36]. It is clear that significant progress is required before photonic quantum factoring algorithms pose a serious threat to current encryption techniques.

The main obstacle to achieving scalable photonic quantum computing is the probabilistic nature of post-selection. There is also the technical challenge of increasing numbers of single-photon sources and detectors. Inefficient sources and detectors produce errors, which can only be accommodated up to an error-correction threshold which depends on the specific techniques being employed. The lowest reported requirement is for a combined source and detector efficiency greater than two-thirds [37], which means exceeding 82.5 % efficiency with two equally-efficient devices. This is an extremely daunting benchmark to achieve with current single-photon technologies. Optimised timing performance is a clear benefit because it determines the rate at which operations can be performed. Additionally, linear optical quantum computing requires indistinguishable photons; these are described in Section 2.2. Recent developments and the current state of the art in single-photon production and detection are reviewed in Sections 2.1 and 2.2.

1.1.3 Single-photon devices and optical fibre

The development of fibre-based quantum photonic systems enables them to be integrated with existing fibre telecommunications networks. Optical fibre is flexible and robust, and allows communication between points which cannot be connected via free space links. In order for quantum photonic applications to make the best use of standard silica glass fibre, experiments need to be conducted at wavelengths that experience low loss; 1.31 μm and 1.55 μm (shown in Figure 1.6).

Single-photon detection at telecom wavelengths is a significant challenge; the small photon energy (~ 1 eV $= 1.6 \times 10^{-19}$ J) lies beyond the spectral sensitivity of established, silicon-based single-photon detectors [38]. Single-photon detectors operating at telecom wavelengths tend to have poorer performance [39], but these devices have progressed rapidly over the last decade [40]. The development of single-photon detectors and the current state of the art in photon detection are reviewed in Section 2.1. Chapter 3 details the construction and characterisation of a superconducting nanowire single-photon detector system.

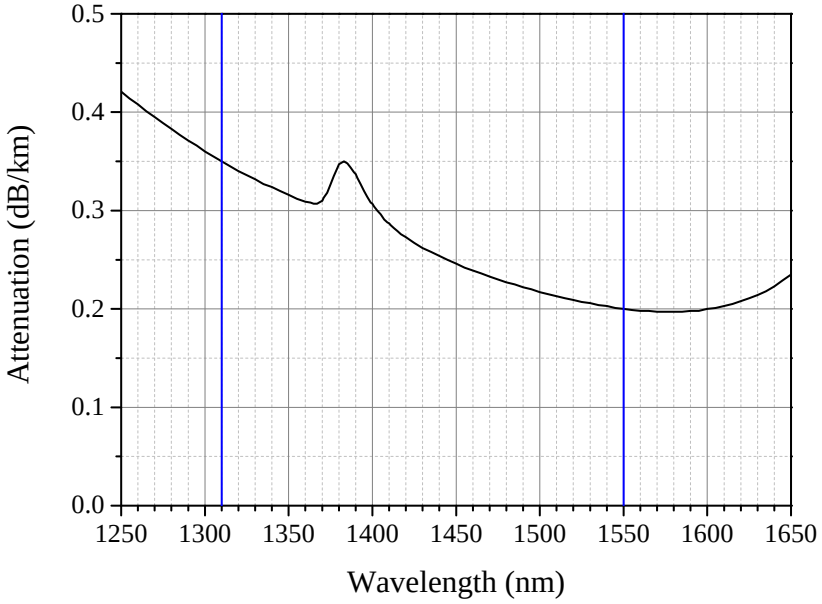

Figure 1.6: **Loss versus wavelength in standard SMF28 optical fibre [41]**

Sources that operate at the single-photon level can be produced with attenuated lasers, nonlinear optical processes and single quantum emitters [39]. Any practical source must have both high generation and collection efficiencies, and be able to match the emission rate required by the intended application. Telecom wavelength sources are relatively straightforward to realise with attenuated lasers and nonlinear optical techniques. These sources can be used in some applications, but neither source can guarantee the production of a single photon at a specific time. Single quantum emitters have the potential to achieve this goal, but producing high-performance sources at these wavelengths remains a challenge. Self-assembled III-V semiconductor quantum dots are promising candidates for single-photon generation at 1.3 μm [42, 43]. The development of single-photon sources is reviewed in Section 2.2. Chapter 4 describes the single-photon source experiment at NPL, which is based on self-assembled InAs/GaAs quantum dots in micropillar cavities with emission at wavelengths around 900 nm.

It is important to determine and minimise the probability of multi-photon emission from sources because some applications specifically require single-photon states. This can be characterised by measuring the second-order correlation function with a Hanbury Brown and Twiss interferometer [44]. In this experiment, single-photon emission is confirmed by the lack of simultaneous detection events from two out-

put ports of a beam splitter. This measurement is described in Section 2.2.2 and performed in Section 4.4.

The ability to quantify photon indistinguishability is also important because it is required in linear optical quantum computing. Indistinguishability can be measured with a Hong-Ou-Mandel experiment [45], which overlaps two identically-polarised photons on a beamsplitter and correlates detection events on the two output ports. Two-photon interference causes indistinguishable photons to exit from one port together, which prevents simultaneous detection events. Section 2.2.3 describes this measurement in more detail, and Section 4.5 presents the design and characterisation of a Hong-Ou-Mandel experiment.

High-resolution spectral measurement plays an important role in source characterisation. One application is investigating the degeneracy of transitions from quantum emitters with a view to producing entangled photon states [46]. As mentioned in Section 1.1.1, spectral characterisation can also be used in QKD systems to verify that information is not leaked into side channels. Scanning Fabry-Pérot interferometers (SFPIs) have been used to perform high-resolution single-photon spectroscopy on quantum dots with emission wavelengths around 900 nm [46, 47, 48]. To facilitate the characterisation of fibre-compatible sources, a telecom-wavelength SFPI system has been designed and constructed, and forms the subject of Chapter 5.

1.2 Summary of presented work

This thesis reports on three interlinked projects, spanning single-photon production, detection and spectral characterisation. Their common goal is the development of quantum photonic measurement systems, with a focus on the use of a superconducting nanowire single-photon detector (SNSPD). Chapter 2 provides an overall review of the relevant literature, then each project and its results is presented separately in a self-contained chapter.

Chapter 3 reports on the construction and characterisation of a SNSPD system. This instrument enables telecom wavelength single photons to be detected with excellent timing resolution and a low dark count rate. Chapter 4 describes measurements made on quantum-dot single-photon sources, including the design and characterisation of a Hong-Ou-Mandel experiment to measure photon indistinguishability. Chapter 5 presents the design, construction and characterisation of a scanning Fabry-Pérot interferometer (SFPI) that, in conjunction with the new SNSPD system, can perform high-resolution single-photon spectroscopy at telecom wavelengths. The capacity to perform these measurements is important for assessing quantum photonic sources, and extends the capabilities of the single-photon metrology group at NPL.

Chapter 2

Approaches to generating and detecting single photons

2.1 Single-photon detectors

In addition to quantum photonics, single-photon detectors are relevant in fields as diverse as time-of-flight ranging [49], biophysics [50] and ground-to-space communications [29]. This is because they are used to detect weak optical signals as well as true single-photon emission. Applications place a range of demands on detectors; Section 2.1.1 describes the main detector performance characteristics. Section 2.1.2 introduces some common and high-performance single-photon detectors and their differing capabilities. A superconducting nanowire single-photon detector (SNSPD) system was constructed as part of this work (detailed in Chapter 3). Section 2.1.3 therefore concludes with a detailed account of the operation and development of SNSPDs.

2.1.1 Detector performance characteristics

The main characteristics for assessing detector performance can be defined as follows:

- **Jitter (Δt):** Jitter describes the timing uncertainty in the output signal from a detector, which broadens features in a temporal correlation histogram. It is defined as the full width at half maximum (FWHM) of a correlation peak where the detector is the only significant source of timing uncertainty. Measurements of detector jitter are reported in Section 3.3.3.

- **Reset time:** A single-photon detector is often insensitive to incoming photons while a detection event is occurring. This period is commonly called the reset time ($\tau_{detector}$). There is also a finite inactive period associated with timing electronics ($\tau_{electronics}$). The longer of the two periods limits the maximum photon detection rate.

- **Efficiency:** The overall system detection efficiency (η_{SDE}) is defined as the proportion of incoming photons that result in detection events. It is a product of the coupling efficiency to the active area of the detector ($\eta_{coupling}$), the absorption efficiency of the active material ($\eta_{absorption}$), and the quantum efficiency (η_{QE}) - the efficiency with which absorbed photons are converted to output pulses.

  $$\eta_{SDE} = \eta_{coupling} \times \eta_{abs} \times \eta_{QE} \tag{2.1}$$

  This separation of terms is useful for assessing emerging detection technologies, where the coupling and absorption factors may not yet be optimised.

- **Dark count rate (D) and afterpulsing:** Dark counts are false detection events. They can be caused by thermal or electrical fluctuations falsely triggering the detection mechanism. The noise in a signal due to dark counts can be reduced by gating, which involves only switching the detector on when photons are expected.

Afterpulses are false events that occur after a true detection event. In semiconductor detectors, they can be caused by the delayed release of a trapped electron. Gating can also be used to reduce the detection of afterpulsing events.

- **Photon number resolution:** Detectors with single-photon sensitivity often respond the same way when there are multiple incident photons. Single-photon detection is verified by carefully calibrating an attenuated test source. Some types of detectors can resolve the number of incident photons. This is an important property in quantum photonics applications that use multi-photon states [51], and facilitates the extension of optical metrology down to the single-photon level [52].

- **Spectral range:** The sensitivity of a detector at low photon energies determines the longest wavelength at which it can detect single photons. Detector properties commonly vary with wavelength, so it is important to consider detector specifications at the wavelength of interest.

It is not useful to consider any of these properties in isolation; the detector with the highest efficiency might also have the highest dark count rate, which is problematic for QKD and quantum computing. A figure of merit tailored to quantum information applications was proposed by Hadfield in 2009 [40] and has been adopted in subsequent articles [39, 53]:

$$H = \frac{\eta_{SDE}}{D\Delta t} \tag{2.2}$$

This quantity, H, scales the detection efficiency by the number of dark counts D in the smallest possible gate period, which is set by the jitter of the detector Δt. This therefore represents the best possible ratio of signal to dark counts that can be achieved with the detector.

2.1.2 Photon detection mechanisms

The first detector to record single photons was the photomultiplier tube in the 1940s [38]. Still in use today, the photomultiplier tube is based on cathode ray tube technology and the photoelectric effect; a photon incident on a cathode releases an electron, which is accelerated across a potential to a series of dynodes. The energy of one electron hitting a dynode releases a cascade of secondary electrons, which are then accelerated to the next dynode. This charge multiplication process results in a measurable current pulse at the anode [54]. Photomultiplier tubes can provide excellent timing resolution (jitter $\sim$ 20 ps [38]). Efficiency and spectral range depend on the choice of photocathode material. Materials that can detect at telecom wavelengths have quite low efficiencies, achieving around 2 % system detection efficiency at 1550 nm, with a 1 kHz dark count rate [40]. As photomultiplier tubes are housed under vacuum, they are large and fragile compared to the semiconductor-based detectors that were later developed.

Avalanche photodiodes are solid-state photodetectors that use semiconductor materials for charge production and amplification. Photons incident on a reverse biased p-n junction excite electron-hole pairs in the depletion region, which are then accelerated towards the bias electrodes. The accelerating charges excite further electron-hole pairs, creating an avalanche that results in a measurable pulse. In the 1960s, it was found that biasing an avalanche photodiode beyond its breakdown voltage resulted in sensitivity to single photons [55]. Devices operated in this way were differentiated with the name 'single-photon avalanche diodes' (SPADs). The minimum detectable photon energy is determined by the semiconductor band gap; silicon SPADs have been developed into very successful single-photon detectors for wavelengths shorter than 1 μm, but materials with smaller band gaps such as InGaAs are required to reach longer wavelengths. While InGaAs SPADs perform well on individual characteristics, they suffer considerable performance trade-offs compared to their silicon counterparts [56]. A recently reported silicon SPAD achieved 73.8 % system detection efficiency at λ = 600 nm with a 2.2 kHz dark count rate [57]. For InGaAs SPADs, system detection efficiencies up to 45 % at λ = 1310 nm

have been achieved by increasing the overbias voltage, which also increases the dark count rate [56]. Recent efforts to improve timing performance and lower dark counts used quenching resistors to reduce the avalanche charge and sophisticated electronics to read out the smaller pulses, achieving 10 % system detection efficiency at $\lambda = 1550$ nm with a jitter of 30 ps FWHM and a 100 Hz dark count rate [58].

Visible light photon counters emerged in the late 1990s, offering much higher detection efficiency than the available silicon SPADs: 88 % at $\lambda = 694$ nm [59]). Also based on silicon, these detectors have separate absorption and charge multiplication areas, are operated at cryogenic temperatures (~ 7 K) and offer photon number resolution [60]. Drawbacks of visible light photon counters include high dark count rates (~ 20 kHz [59]) , long reset times (~ 100 ns [59]) and being limited to sub-micron wavelengths [61].

The superior performance of silicon-based single-photon detectors led to the development of upconversion systems to address their wavelength limitation. These systems induce sum-frequency generation with a strong pump laser to convert near-infrared photons to visible wavelengths [62, 63]. Early implementations suffered high dark count rates; pump photons that underwent spontaneous parametric downconversion were converted to visible wavelengths for detection alongside the true photon signal. More recent detector systems have addressed this problem by using pump wavelengths longer than the wavelength of interest. This means that downconverted pump photons are outside the phase matched bandwidth for upconversion and so do not contribute to the dark count rate [64]. While dark counts remain a drawback of this type of detector, system detection efficiencies up to 59 % have been achieved [39].

Superconductors can also be used to detect single photons. The energy gap between superconducting and normal ground states is a few meV, which means it can easily be disrupted by the ~ 1 eV energy of telecom-wavelength photons [65]. Transition edge sensors and superconducting nanowire single-photon detectors are two examples of successful infrared single-photon detectors based on superconductors. Transition edge sensors operate at the critical temperature of the superconducting

material. When a photon is absorbed, a small active area maintained at the transition temperature experiences a measurable change in resistance. With a voltage bias across the active area, this causes a dip in current flow that scales with photon energy, facilitating photon number resolution [66, 67]. Transition edge sensors have been developed to resolve up to 1000 photons, which provides scope for linking quantum metrology with conventional radiometry [68]. This type of detector is also exceptionally efficient when embedded in an optical cavity, with recent devices yielding 98 % system detection efficiency at 850 nm [69] and 95 % at 1550 nm [70]. Drawbacks of transition edge sensors include long reset times, high jitter and low operating temperature ($\sim$ 100 mK), but they currently offer the highest system detection efficiency [39].

The superconducting nanowire single-photon detector (SNSPD) is triggered by exceeding the critical current density rather than critical temperature. In operation, a superconducting nanowire is biased very close to its critical current - the absorption of a single photon creates a resistive hotspot which momentarily perturbs the current distribution and generates a fast voltage pulse [65]. SNSPDs exhibit excellent timing performance, including jitter below 30 ps FWHM [71] and reset times below 10 ns [72]. Early devices with NbN nanowires had $\eta_{SDE} < 1$ %, but more recently efficiencies of $\eta_{SDE} > 23$ % at telecom wavelengths have been reported for NbTiN nanowires on oxidised silicon substrates [73]. Additionally, the recent development of devices based on WSi nanowire has provided a breakthrough in efficiency, increasing η_{SDE} to $\sim$ 90 % with cavity-enhanced devices [74, 75].

Superconducting detectors already offer impressive performance; continuing reports of improvement indicate that they are yet to reach technical maturity. However, they require operating temperatures below 10 K which limits their utility in some applications. While closed-cycle cryocoolers can be used to produce practical detector systems [76], InGaAs SPADs operate at room temperature or with Peltier cooling, and are also continuing to improve [77]. While there are still trade-offs between efficiency, timing and dark counts, detector technologies are moving towards simultaneous high performance in these areas. As commercial systems emerge and application requirements become more diverse, future trade-offs are likely to pertain

to operating temperature and the development of low-noise, large area, multi-pixel arrays. An exhaustive account of infrared single-photon detector development is beyond the scope of this review; references [39] and [40] address the topic in detail with great clarity. This section continues with a more in-depth examination of SNSPDs.

2.1.3 Superconducting nanowire single-photon detectors

Fast photon detection with superconducting nanowires was proposed in the mid-1990s [78, 79] and demonstrated in 2001 [65]. The absorption of a photon can cause the nanowire to become resistive for a short period, after which the superconducting state is restored without the need for an active reset mechanism. This process results in a measurable voltage pulse [79].

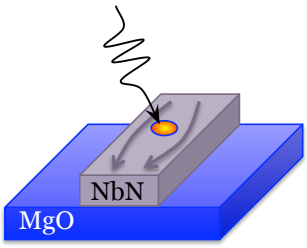

Figure 2.1: **The SNSPD photon detection mechanism.** An incident photon creates a local 'hot spot' where the Cooper pairs in the material are broken for a short time period. During this time, the bias current flows around the hot spot, which increases the local current density. If this exceeds the critical current density, a short-lived resistive region forms across the width of the wire, resulting in a measurable output pulse.

The SNSPD photon detection mechanism is illustrated in Figure 2.1. A bias current that is close to the nanowire's critical current is applied. The local heating caused by photon absorption creates a resistive 'hot spot' on the wire, which the current diverts around. If the diverted current exceeds the critical current density, an entire cross section of the wire becomes resistive until the energy is dissipated. This process produces a measurable voltage pulse [80]. As the mechanism is not based on the superconducting transition temperature, the nanowires are typically maintained several degrees below their critical temperature using liquid helium or a closed-cycle refrigerator.

From the outset, SNSPDs were noted for their excellent timing properties. Their

fast switching and natural recovery mechanism result in low timing jitter (< 30 ps FWHM [71]) and a short reset time (< 10 ns [72]), while the small energy gap between superconducting and resistive ground states means that their single-photon sensitivity extends to wavelengths of several microns [81]. Their low dark count rate (< 1 kHz, bias dependent) facilitates free-running operation, which enables photoluminescence lifetime studies that are not limited by a gate window. Recent developments in device geometry [82] and material [83] have yielded devices with extremely low dark count rates, which benefits quantum information applications.

Achieving high system detection efficiencies with SNSPDs posed a considerable challenge because the superconducting active area is necessarily very small and thin. To increase the coupling efficiency, nanowire geometries have evolved from a single straight wire [65] to much longer wires in meander designs covering square [84, 85] and circular areas [73] (shown in Figure 2.2). The production of larger meanders is limited by the increased occurrence of imperfections in the wire during fabrication. They are referred to as constrictions and have a lower critical current density relative to the rest of the wire. This reduces the maximum bias current that can be applied, which lowers the detection efficiency [86] and results in a spatially non-uniform response [87]. Approaches to increasing device area include the development of grids of parallel nanowires and arrays of shorter nanowires (also illustrated in Figure 2.2) [88, 89]. Additionally, major improvements in system detection efficiency have been achieved by using optical cavities and anti-reflection coatings to increase the photon absorption efficiency [90, 91]. Using these approaches, η_{SDE} has improved from below 1 % to greater than 23 % at 1310 nm with a 1 kHz dark count rate [73, 92, 93].

The optimal selection of superconductor and substrate materials has also been investigated. The first devices were made from NbN [65], which is still used in SNSPD systems [72], aided by improvements in thin film deposition methods [84]. NbTiN devices have also been successful, exhibiting comparable efficiency to NbN with lower dark count rates [94]. Sapphire was initially a common substrate [65, 95]; this was an obstacle for the development of integrated photonic circuits because the high fabrication temperatures ($\sim$ 900 ^{o}C) that were typically used can cause outgassing in some materials [96]. This led to the use of MgO [84, 96], Si [91] and $LiNbO_3$

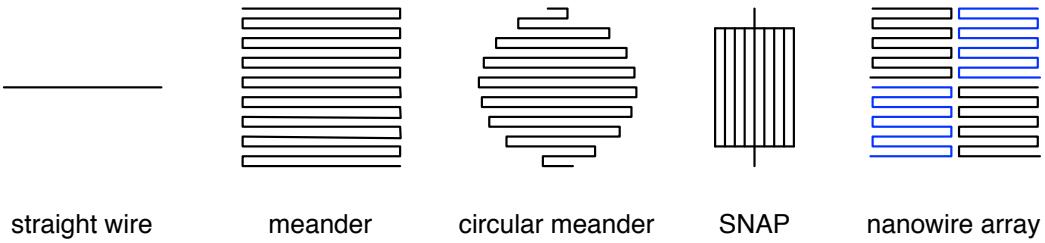

Figure 2.2: **Development of nanowire geometries.** In order to increase coupling efficiency, nanowire designs evolved from a straight wire to meanders covering square and circular areas. The superconducting nanowire avalanche photodiode, or SNAP, is a parallel nanowire array whose shorter wires provide a faster reset time. Nanowire arrays also have a faster recovery than a single meander, facilitating the development of larger-area devices.

[97] as alternative substrate materials; nanowires have also been directly integrated with Si_3N_4 waveguide structures [98]. The efficiency of NbN and NbTiN devices has recently been surpassed by nanowires made from an amorphous WSi alloy. Simple meander devices have achieved system detection efficiencies from 19 % to 40 %, with saturated efficiency above a certain bias point observed across wavelengths from 672 nm to 1850 nm. This is thought to be due to saturated internal quantum efficiency, and relaxes the fabrication requirements for optimised devices [83]. More complex devices based on this material have recently achieved a significant improvement to $\eta_{SDE} > 90$ % at 1550 nm, with a reset time of 40 ns and jitter of 150 ps FWHM, at operating temperatures ≤ 2 K [75]. With efficiency maximised, these systems exhibit dark count rates ≤ 1 kHz [75]. This is attributed to fibre-coupled blackbody radiation because the dark count rate drops below 1 Hz when no fibre is present near the nanowire device [74]. While the jitter and reset time are larger than for typical niobium-based SNSPDs, the timing properties of WSi nanowires are considerably better than transition edge sensors, which are the only other detector to offer $\eta_{SDE} > 90$ % at 1550 nm. It is anticipated that improvements in the cavity and nanowire designs will yield devices with efficiencies approaching 100 % [74].

The 'wire grid' structure of a nanowire meander causes polarisation-dependent photon absorption [99]. This effect becomes stronger with increasing wavelength [100] and decreasing fill factor, where fill factor is the fraction of the active area covered by the nanowire [99]. Polarisation dependence can be reduced by using spiral meanders or orthogonally-oriented panels of nanowires at the cost of a lower, averaged efficiency across all input polarisations [94]. More recently, stacking orthogonal

nanowire meanders was demonstrated to reduce polarisation dependence to the 2 % level without compromising efficiency [74].

The SNSPD reset time depends on the dissipation of the absorbed photon energy and the recovery of the initial bias current distribution in the superconducting nanowire. While the hotspot region typically grows and disappears in under a nanosecond [101], kinetic inductance limits the rate at which the current can recover to its full bias level [102]. The kinetic inductance scales linearly with wire length, which means that devices aiming to improve efficiency with longer wires covering larger areas also recover more slowly, limiting the maximum detection rate [102]. It is therefore a challenge to develop faster SNSPD devices while improving or at least maintaining the detection efficiency. One approach is to cover the same area with a shorter nanowire (*i.e.* with a lower fill factor), then increase the absorption efficiency by using an integrated nano-antenna to enhance the field strength in the active area [72]. Another approach is to use an an array of shorter nanowires [103] (illustrated in Figure 2.2). Multi-pixel devices achieve the same efficiency as equivalent single-wire meanders with a higher maximum count rate, but require more complex readout electronics [71]. Such devices have been used to resolve photon number [71] and to conduct beamsplitter-free multi-photon correlation measurements [104].

An alternative approach to making faster devices without compromising detection efficiency is to connect adjacent wires in parallel (see Figure 2.2). When a photon is absorbed in one nanowire, the current diverts into the other nanowires and they all become resistive, triggering an output pulse [88]. These devices are referred to as superconducting nanowire avalanche photodetectors (SNAPs), and have successfully demonstrated reset times of 3.3 ns while maintaining $\eta_{SDE} = 20$ % at 1550 nm [105].

To summarise, SNSPDs have intrinsically excellent timing properties, low dark counts and wide spectral sensitivity. Developments over the last few years have increased system detection efficiencies from below 1 % to around 90 % [75]. With a number of companies now selling commercial SNSPD systems [106], SNSPDs are highly competitive single-photon detectors for optical quantum information processing at telecom wavelengths.

2.2 Single-photon sources

Quantum photonics puts the investigation of photon emission in a new context. In addition to revealing the underlying structure of an emitter, photons can be characterised to determine their suitability for a range of applications. In fact, photonic sources are being specifically developed for quantum information applications. Section 2.2.1 describes the key properties that need to be optimised, followed by a more detailed discussion of photon characterisation in Sections 2.2.2 and 2.2.3. Photon production mechanisms are briefly reviewed in Section 2.2.4, then Section 2.2.5 describes quantum dot (QD) single-photon sources, which form the subject of the experimental work presented in Chapter 4.

2.2.1 Source performance characteristics

A perfect source of single photons would have the following properties [39]:

- Photon emission when triggered, with negligible timing jitter
- 100 % efficiency (photon emission at every trigger)
- Exclusive single-photon emission (no multi-photon events)
- Emission of indistinguishable photons
- Optimised repetition rate (negligible reset time)

Real photon sources are assessed with reference to this ideal and compared with the requirements of specific applications; the appropriate central wavelength and spectral bandwidth is application-dependent, as is the tolerance of imperfections. Three mechanisms are commonly used in quantum photonics to produce light at the single-photon level:

1. Attenuation of laser pulses
2. Non-linear processes
3. Excitation of systems with discrete, quantised energy states

Photonic sources can be categorised in several ways; Eisaman *et al.* consider nonlinear sources to be 'probabilistic single-photon sources', quantised systems to be 'deterministic single-photon sources' and do not review attenuated laser sources [39], while Lounis *et al.* refer to lasers and nonlinear sources together as 'macroscopic sources' and quantised systems as 'microscopic single-photon sources' [107]. Other reviews of single-photon sources exclusively consider quantised systems and subcategorise based on emission control techniques [108] or the strength with which the system is coupled to an emission-enhancing cavity [109]. This review considers photonic sources grouped by production mechanism according to the above list.

The term 'deterministic' is used to encompass both unit emission efficiency and emission at a well-defined point in time. Sources based on attenuated lasers or nonlinear processes cannot be deterministic because their photon emission obeys Poisson statistics and therefore cannot occur with unit emission efficiency [15, 109, 110]. Sources based on single quantum emitters have the potential to approach the deterministic ideal; a common technique is to prepare a single emitter in an excited state that relaxes by emitting a single photon. The jitter of such a source is typically limited by the lifetime of the radiative state [108], but can be reduced by introducing a competing non-radiative decay channel [111]. A technique that provides more precise control over photon emission is stimulated Raman scattering involving adiabatic passage (STIRAP) [112]. This technically challenging approach facilitates the production of single anti-Stokes photons into a single cavity mode with unit emission efficiency, negligible timing jitter and the possibility of tuning the properties of the photon wavepacket [113].

In practice, sources with unit emission efficiency cannot deliver photons perfectly deterministically due to collection losses. The overall efficiency of a source (η_{source}) depends on the efficiencies with which photons are emitted ($\eta_{emission}$) and collected for delivery to an experiment ($\eta_{collection}$):

$$\eta_{source} = \eta_{emission} \times \eta_{collection} \tag{2.3}$$

The collection efficiency is often taken to be the fraction of emitted light that is collected by the first lens after the source [114]. Collection efficiency can be improved

with the use of cavities, lenses and waveguides [7]. High-finesse cavities designed for STIRAP have achieved directional emission such that $\eta_{collection} = 89$ % [115], while a state-of-the-art source based on a quantum dot in a tapered nanowire cavity has achieved $\eta_{source} = 72$ % [116]. With nonlinear sources, heralding efficiencies as high as 85 % [117] have been reported; this is the efficiency with which a photon is delivered after detection of the heralding signal. In this experiment, the probability of producing a pair of photons in a given pump pulse was 0.001 [117].

2.2.2 Photon emission statistics

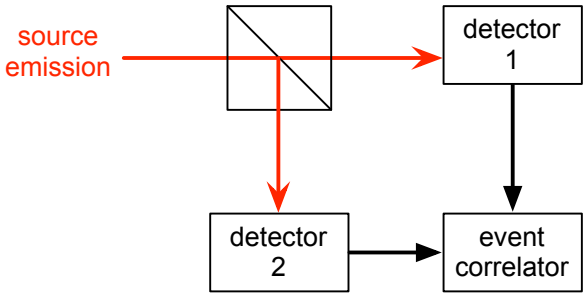

Figure 2.3: **Hanbury Brown and Twiss intensity interferometer.** A light source is incident on a beamsplitter and detected at both output ports. A correlator measures time delays between events at the two detectors and creates a histogram of those time delays. In the diagram, red paths are optical and black paths are electrical.

The Hanbury Brown and Twiss experiment provides information about a light source by correlating the intensities at two photodetectors. It was originally used to measure the angular diameter of stars by correlating intensities at different positions [44]. In quantum optics, the detectors are fixed as shown in Figure 2.3 and detection events are correlated as a function of time delay, τ. This temporal correlation histogram represents the second-order correlation function of the source, $g^{(2)}(\tau)$, which can be written in terms of the intensity measured by each detector, $I_{1,2}(t)$:

$$g^{(2)}(\tau) = \frac{\langle I_1(t) I_2(t+\tau) \rangle}{\langle I_1(t) \rangle \langle I_2(t+\tau) \rangle} \tag{2.4}$$

For coherent laser light, which has a constant intensity and Poissonian photon number distribution, correlation events occur at all time delays with equal probability.

This is illustrated in Figure 2.4 a). Sources with fluctuating intensities exhibit a correlation maximum at $\tau = 0$. This is due to a higher proportion of photons being emitted in the periods of high intensity, which increases the probability of measuring two photons close together in time. Emission with this property is referred to as 'bunched', and the specific form of the feature can be Lorentzian or Gaussian depending on the dominant spectral broadening mechanism [118]. These cases are illustrated in Figure 2.4 alongside another interesting case: antibunching.

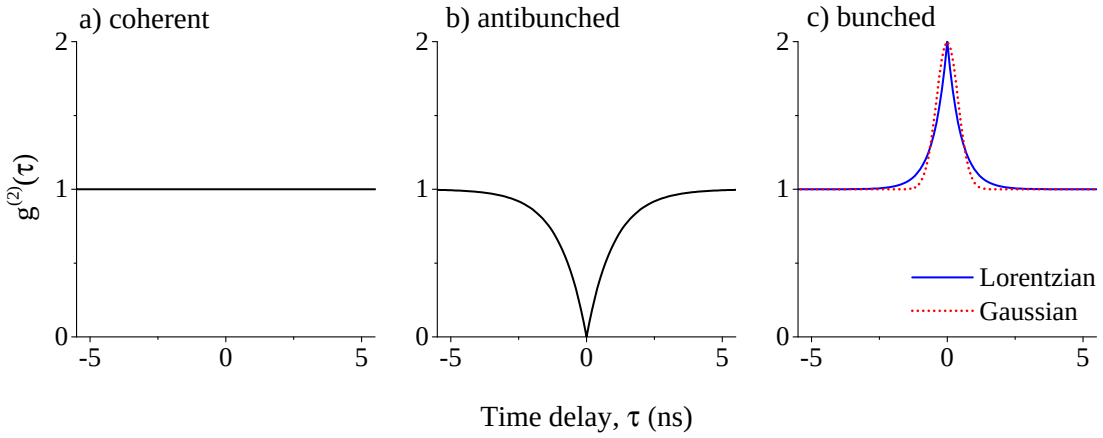

Figure 2.4: **Photon emission statistics.** a) Coherent emission has a flat correlation histogram as a function of time delay; b) Perfect antibunching (calculated for lifetime-limited emission with a 1 ns lifetime [119]); c) Bunched light sources with Gaussian and Lorentzian broadening (calculated using 1 ns time constants in equations from [15]).

An ideal single-photon source produces perfectly antibunched light, meaning that $g^{(2)}(\tau = 0) = 0$. When a source never simultaneously emits more than one photon, the two detectors cannot fire simultaneously. Consequently, at $\tau = 0$ either $I_1(t)$ or $I_2(t)$ must be zero, which makes $g^{(2)}(\tau = 0) = 0$. As a classical wave is always divided equally at a 50:50 beamsplitter, this result cannot be explained without treating light as a quantised stream of photons [120].

The first observations of antibunching were in the radiative emission of excited atoms [120, 121]. This provided evidence that transitions between quantised states release single photons, which made the notion of a single-photon source a real possibility. The potential impact of photons in quantum information applications (which was discussed in Section 1.1.2) drove extensive research into making such sources a reality. Near-perfect antibunching has been reported for sources based on trapped

ions [122], atoms [123] and quantum dots [124]. Excellent antibunching has also been produced with heralded SPDC-based sources ($g^{(2)}(\tau = 0) = 0.0014$ [125]), but this can only be achieved with low emission efficiency because the probability of generating multiple photon pairs increases with pump power.

2.2.3 Photon indistinguishability

Photon indistinguishability is utilised in optical quantum computing [8] and more generally in the production of entangled states [126]. It describes the similarity between photons; perfect indistinguishability means that the wavepackets are identical. In this case, it is not possible to tell them apart if they overlap with aligned polarisations; this results in two-photon interference, which can be measured using a Hong-Ou-Mandel interferometer [45]. The visibility of two-photon interference provides a quantified measure of the extent of indistinguishability. This can be thought of as measuring the overlap integral between the two photons.

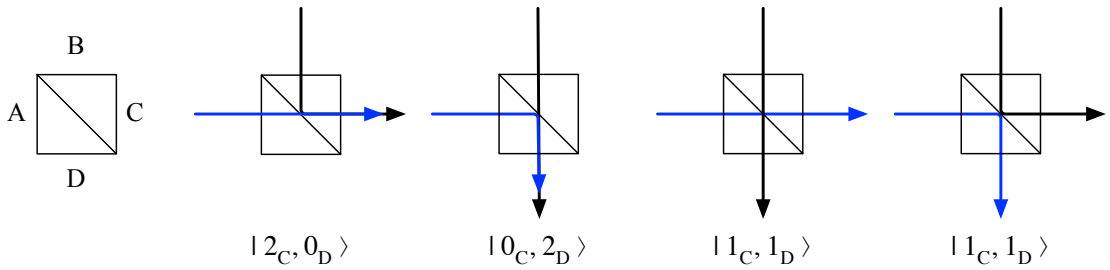

Figure 2.5: **Two photons at a beam splitter.** The four possible output configurations are illustrated. If the two photons are indistinguishable, the probabilities for cases $|1_C, 1_D\rangle$ interfere destructively and the photons always exit from one port together.

In the Hong-Ou-Mandel experiment, a photon is directed to each input port of a beamsplitter and the detection events on the output ports are correlated as a function of time. With the ports labelled as shown in Figure 2.5, the action of the beamsplitter can be expressed in terms of creation operators as follows [127]:

$$\hat{a}_A^\dagger = t\hat{a}_C^\dagger + r\hat{a}_D^\dagger \tag{2.5}$$

$$\hat{a}_B^\dagger = r\hat{a}_C^\dagger + t\hat{a}_D^\dagger \tag{2.6}$$

where the reflection and transmission coefficients R and T are $|r^2|$ and $|t^2|$ respectively. When two indistinguishable photons overlap at a beamsplitter, the state at the exit of the beamsplitter (denoted $|\Psi\rangle$) can be written as follows [127]:

$$\begin{aligned} |\Psi\rangle &= \hat{a}_A^\dagger \hat{a}_B^\dagger |0\rangle \\ &= (t\hat{a}_C^\dagger + r\hat{a}_D^\dagger)(r\hat{a}_C^\dagger + t\hat{a}_D^\dagger)|0\rangle \\ &= \left[(t^2+r^2)\hat{a}_C^\dagger \hat{a}_D^\dagger + rt\hat{a}_C^\dagger \hat{a}_C^\dagger + rt\hat{a}_D^\dagger \hat{a}_D^\dagger\right]|0\rangle \\ &= (t^2+r^2)|1_C, 1_D\rangle + \sqrt{2}rt|2_C, 0_D\rangle + \sqrt{2}rt|0_C, 2_D\rangle \end{aligned} \tag{2.7}$$

A 50:50 beamsplitter has $t = \frac{1}{\sqrt{2}}$ and $r = \frac{i}{\sqrt{2}}$, so the $|1_C, 1_D\rangle$ component in Equation 2.7 goes to zero and the photons always exit together. This provides a clear experimental signature that can be observed by correlating detection events while varying the arrival time of the two photons; only one detector will fire when the photons enter the beamsplitter simultaneously. If two photons have orthogonal polarisations but are identical in every other respect, interference does not occur. Instead, the photons become entangled because their polarisations are correlated and they have equal probability of exiting from each output port. This means that a source of indistinguishable photons can be used to generate entangled states [15].

Hong-Ou-Mandel experiments have successfully measured two-photon interference in the emission of a range of single-photon sources including single molecules [128], trapped ions [122] quantum dots [129] and nonlinear photonic sources [130, 131]. An experiment to measure the two-photon interference visibility of the emission from a quantum dot single-photon source is described in Section 4.5.

2.2.4 Single-photon production mechanisms

Attenuated laser sources

The simplest way to produce a source that emits an average of one photon per pulse (denoted $\mu = 1$) is to attenuate a pulsed laser to the single-photon level. Such sources can operate at a wide range of wavelengths and at repetition rates in excess of 1 GHz [17]. The drawback is that photon number follows a Poisson distribution, so attenuation to $\mu = 1$ results in an 18 % probability of two-photon pulses and a 36 % probability that a pulse will contain no photons at all. This can be problematic - true single-photon emission is essential in quantum computing, while in the context of QKD, empty pulses limit the maximum key transmission rate and multi-photon pulses can make data vulnerable to photon-splitting attacks [19]. Techniques such as the decoy state protocol allow key integrity to be preserved using sources that exhibit multi-photon emission [20, 21]. This has enabled QKD experiments to be performed with attenuated laser sources [18, 22, 17, 132].

Sources based on nonlinear optical processes

The discovery of spontaneous parametric downconversion (SPDC), a second-order nonlinear process in which a photon is split into two lower energy photons, provided another route to single-photon generation [133]. In 1986, an experiment successfully used SPDC to produce localised one-photon states at 659 nm and 746 nm by detecting one photon in a pair to herald the presence of the other [134]. Sources based on nonlinear materials can be designed to produce photons at specific wavelengths over a wide spectral range including the telecoms region [125, 135], and can be pumped with ultrafast lasers to produce photons with negligible timing jitter [136]. There is a trade-off between the rates of true and accidental coincident photon pairs that can be achieved, that depends on factors including the pump power and acceptance bandwidth. As with attenuated lasers, the production of photon pairs via SPDC follows a Poisson distribution, limiting the maximum single-pair rate that can be achieved while simultaneously minimising multi-pair events. A recent experiment achieved a pair production rate of 2.6×10^6 pairs/s/mW with a true-to-accidental coincidence rate of 4:1 [137]. While the downconversion pro-

cess is inherently probabilistic, the probability of delivering a photon at a specific point in time can be increased by holding the heralded photon in a storage loop until it is required [138]. Another method multiplexes the output from of several simultaneously-pumped crystals and uses a triggered switch to select one path that contains a photon [139]. Such techniques bring these sources closer to deterministic performance.

Four-wave mixing is a third-order ($\chi^{(3)}$) nonlinear process that can also be used to generate single photons. Two pump photons are converted into a pair of correlated photons, within the constraints of energy and momentum conservation. These photon pairs can be produced by pumping an optical fibre that has the required $\chi^{(3)}$ optical nonlinearity, and can be used as a photon pair source [140, 141] or to produce heralded single photons [142]. Sources have been demonstrated at wavelengths ranging from 650 nm [142] to 1550 nm [141]. One recent experiment reports telecom-wavelength photon pair generation at a rate of 10 MHz with a signal-to-noise ratio of 100 [143]. The confinement of the generated photons in optical fibre improves their spatial mode compared to direct emission into free space, which in turn improves the collection efficiency. Similarly, the use of waveguide structures with SPDC-based sources has also been demonstrated to improve collection efficiency [137]. Correlated photons from nonlinear processes can also directly provide polarisation- or frequency-entangled photon pairs [126, 130]. Entangled photons are crucial in optical quantum computing [34]; as such, the use of nonlinear materials to create entangled photon sources is also an active field of research.

Sources based on quantised systems

Single-photon sources can be made using isolated quantum emitters by exciting a radiative state and selecting the subsequently-emitted photon with a spectral filter. This process can be controlled with higher timing resolution than the free-space lifetime of the state by coupling the emitter to a resonant cavity [144, 112] (emitter-cavity coupling is discussed in more detail in Section 2.2.5). Producing high-performance single-photon sources from quantum emitters is a considerable challenge; consequently, the majority of quantum photonics experiments are car-

ried out with nonlinear sources [42]. Nevertheless, applications such as quantum computing need truly deterministic single-photon sources in order to be successful; single atoms [145], ions [146] and molecules [147], quantum dots [148] and solid-state defects [149] have all been investigated for this purpose.

A single-photon source based on a single trapped ion was first demonstrated in 1987 [150]. Compared to neutral atoms, ions can be positioned and isolated more accurately [39] and trapped for longer periods [146]. A single-photon source based on a single neutral atom was reported in 2004 [145]. With high efficiencies and repetition rates, it is possible to trap a single atom for a sufficient period to be useful in quantum information applications, despite their shorter trapped duration [151]. The difficulty of integrating cavities into ion trapping experiments make single atoms better suited to experiments that employ cavity enhancement techniques [152]. The coupling of a radiative transition to the mode of an optical cavity enhances photon emission rates in the weak coupling regime [144]. In the strong coupling regime, photons can be produced via a process called STIRAP (stimulated Raman scattering involving adiabatic passage), in which a photon is deterministically created in a specific cavity mode [112, 145, 152]. Single ions have been successfully used to probabilistically produce indistinguishable photons [122], entangled ion-photon systems [153] and single photons with highly controlled properties [154]. Recent publications report 17 % overall source efficiency at 780 nm with a 10 MHz repetition rate using a single ^{85}Rb atom [155], and use of a single trapped ^{40}Ca ion to deliver 866 nm photons to a detector with 11 % efficiency [152].

Single photons can also be generated with single molecules isolated in solid state structures, which is much more straightforward than using trapping techniques [156]. A room temperature single-photon source based on a single molecule was demonstrated in 2000 [157]. The downside of molecular structures is that they photobleach - this means that after a period of repeated excitation, the structure changes such that emission at the selected wavelength ceases. However, the lifetime of single molecule-based sources is comparable to the achievable trapping times for sources based on single ions [128]. Single molecules can generate photons with unit efficiency at MHz rates, and collection efficiencies greater than 90 % are achievable with solid

immersion lenses [158]. Single molecule-based sources are being investigated for quantum information applications [158], in addition to widespread application in single-molecule spectroscopy [50].

Defect states in solids can be used to produce single photons and unlike molecules, they do not photobleach. One commonly-used defect is the nitrogen vacancy (NV) centre, a defect in diamond where a nitrogen atom and vacant site replace two carbon atoms [149]. Antibunching from the 637 nm zero-phonon line of a NV centre was first demonstrated in 1997 [159], and a room temperature single-photon source was reported in 2000 [160]. However, the broad linewidth at room temperature means that sources based on NV centres are commonly operated at cryogenic temperatures [161]. Another obstacle to producing sources with NV centres is the high refractive index of diamond, which hinders photon collection efficiency [162]. Approaches to increasing the photon collection efficiency include producing NV centres in diamond nanocrystals [162] and nanowire structures [163], and fabricating integrated lenses [164]; these experiments achieve photon count rates on the order of 10^5 counts per second (cps).

The intrinsic energetic structure of natural quantum emitters fixes their emission characteristics. Such sources can therefore produce photons at specific wavelengths with high repeatability, but those wavelengths are limited to suitable naturally-occurring transitions, which are seldom in the telecoms region. Self-assembled quantum dots (QDs) are semiconductor nanostructures with emission wavelengths that are not limited by an intrinsic underlying structure. They are often referred to as 'artificial atoms' because they have quantised energy states that can be excited to produce single photons at discrete wavelengths. The emission wavelength depends on the size of the QD, which has enabled the fabrication of QDs that can emit at telecom wavelengths for fibre-based quantum information applications [165, 166]. QD-based single-photon sources have been reported operating at a repetition rate of 0.5 GHz [167], while separate experiments have achieved overall source efficiencies around 73 % [116]. QDs are being extensively investigated as photonic sources for quantum information applications [42] and are described in more detail in the next section.

2.2.5 Quantum dot single-photon sources

Self-assembled semiconductor quantum dots (QDs) are leading candidates for producing high-performance telecom-wavelength single-photon sources [42, 43]. Sources exhibiting near-perfect antibunching [124], high efficiency [116] and low timing jitter [111] have been reported, and their integration into solid-state cavity and waveguide structures is increasingly common.

Quantum dots are embedded 'dots' of one semiconductor material inside another semiconductor with a larger band gap energy. At sizes on the order of tens of nanometers [168], the resulting confinement potential has a discrete density of states. QDs can therefore be made into single-photon sources in the same way as natural quantum emitters such as atoms and molecules. Figure 2.6 depicts a GaAs/InAs QD structure; increasing the size of the InAs region will reduce the electron-hole recombination energy, increasing the wavelength of the emitted photons.

The most common way of producing QDs is by self-assembly. Layers of material are deposited by molecular beam epitaxy or chemical vapour deposition onto a lattice-mismatched substrate, for example InAs onto GaAs. The strain between the two materials increases as successive layers are added until the top material breaks up into small 'dots' at random positions on the substrate. Another layer of the substrate material is then deposited to create a three-dimensional confinement potential. This is referred to as the Stranski-Krastanov growth mode [168].

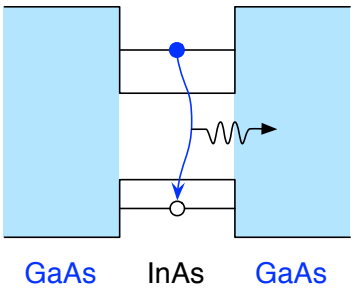

Figure 2.6: **Energy structure of quantum dot.** A confinement potential is produced by surrounding a nanoscale piece of semiconductor with another that has a larger band gap. The small physical size of the potential results in quantised energy states; the excitation and subsequent recombination of electron-hole pairs, or excitons, produces photons at discrete wavelengths.

Two drawbacks of self-assembled QDs are their size distribution and random positioning on the substrate. Early photoluminescence studies inferred a size variation of ±10 % from the spread in emission wavelengths [168]. It has since been shown that annealing processes can reduce size variation [169]. However, mixing between the QD and substrate materials increases the size of the QD and creates a shallower confinement potential, which increases the energy of the emitted photons [169]; this is detrimental to telecom-wavelength source development. Recent experiments have attempted to control the size of QDs by lithographically defining them instead of using self-assembly. Measurements of antibunching indicate single-photon emission [170], but these sources are yet to yield results comparable to self-assembled QDs. Another approach being investigated is the use of downconversion to shift photons to telecom wavelengths after they have been emitted [171, 172].

The random positioning of QDs on a substrate makes isolating a single emitter a considerable challenge. It was found in early experiments that the density of QDs could be controlled by altering the growth conditions [168]. To improve the probability of isolating one QD, samples with a low QD density were grown and small regions were isolated with apertured masks [173] or micropillar structures [114]. This approach also increases the probability of isolating regions that do not contain QDs, but has nevertheless produced a number of successful single-photon sources [42]. More recently, the location of QDs has been controlled by etching small holes in the substrate prior to QD growth [174], and techniques have been developed that not only control the position, but also the size and shape of the QDs to produce more uniform and symmetric emitters [175].

A common technique for operating QD single-photon sources involves optically exciting electron-hole pairs in the bulk semiconductor, which drift into the QD potential and recombine to emit photons at specific wavelengths [148]. This is referred to as above band pumping. It is also possible to excite electron-hole pairs directly within the QD potential (*i.e.* near resonantly), which can reduce background emission and source jitter [129]. A comparison of photon emission with above-band and near-resonant pumping is presented in Chapter 4. Photon emission can also be achieved by electrically injecting carriers, which drift into the QD and recombine [166, 176].

One problem with using QDs (or any quantum emitters) as single-photon sources is that they emit into 4π steradians, which makes efficient photon collection difficult. The situation can be improved considerably by embedding the QD in a cavity [173, 177, 178]. The theory of emission enhancement with cavity structures was reported by Purcell in 1946, and is therefore referred to as the Purcell effect [179]. The magnitude of the emission enhancement is given by the Purcell factor, F_P [15] :

$$F_P = \frac{3Q(\lambda/n)^3}{4\pi^2 V_0} \tag{2.8}$$

where λ = wavelength, n = refractive index, V_0 = cavity mode volume and $Q = \Delta\lambda/\lambda$ = cavity Q (quality) factor. This means that in order to achieve a significant Purcell enhancement, the dimensions of the cavity need to approach that of the emission wavelength. Higher Q factors further increase the enhancement, which occurs when the emitter is resonant with a mode of the cavity; coupling between the cavity and the emitter reduces the lifetime of the radiative state by increasing the density of states into which the photon can be emitted. The emission is also concentrated along the axis of the cavity. Preferential emission in one specific direction can be achieved by making one cavity mirror more reflective than the other. So, the Purcell effect increases both the photon emission rate and the collection efficiency compared to emitters without cavities; using a cavity with equally reflective mirrors, one experiment reported an increase in the efficiency of a QD source from $\sim$0.5 % to 9.6 %, and a four-fold reduction in the lifetime of the radiative state [180].

Santori *et al.* [173] and Michler *et al.* [148] were among the first to report triggered single-photon sources based on a QD in an optical microcavity. A caveat to the benefits of cavity structures is that the radiative transition must be resonant with the cavity. The different thermal expansion coefficients of a QD and the surrounding material allow a certain amount of tuning by changing the temperature of the sample [181]. An alternative technique involves applying an electric field to invoke a Stark shift in the energy structure [48]. More recently, an approach has been demonstrated that provides broadband emission enhancement, circumventing the need for thermal or electrical tuning. A cavity made from a 1-D nanowire has been demonstrated to

provide emission enhancement over tens of nanometers and has achieved the highest overall source efficiency of a QD-based single-photon source (72.0 ± 0.9) % collection into the first lens after the source [116]).

The development of QD single-photon sources has made impressive progress since this project started in 2008. The sample investigated in this work is an array of semiconductor micropillars containing a layer of randomly-positioned, self-assembled InAs/GaAs QDs. The experiments conducted with this source are described in Chapter 4.

2.3 Spectral characterisation techniques

Spectral characterisation provides essential information about quantum photonic sources. As discussed in the previous sections, it can be used to isolate single quantum emitters, identify specific molecules, or assess the suitability of a source for a specific application. Grating spectrometers with electron-multiplying charged coupled devices can be used to record spectra at the single-photon level across a wide range of wavelengths, but do not always provide the high resolution and low loss required to investigate individual quantum emitters [43, 182]. The scanning Fabry-Pérot interferometer (SFPI) provides superior resolution at a cost of limited scan range. In this section, the current state of the art and the trade-offs involved in selecting a spectrometer are discussed.

The purpose of a spectrometer is to record the intensity of a light source as a function of wavelength. This is most commonly achieved with a grating spectrometer, which records the intensity profile of diffracted light on a detector array. The SFPI is an alternative that involves coupling light into a tuneable optical cavity, scanning its resonant frequency and measuring the transmitted intensity [183]. In both cases, the photodetector is selected to match the required spectral range of the measurements.

The main factors that differentiate the two approaches are spectral range and resolution. In grating spectrometers, the maximum spectral range that can be continuously characterised depends on the focal length of the spectrometer, the line density

of the grating and the size of the detector's active area. The spectral resolution of grating spectrometers also depends on focal length and line density, and on the size of the individual pixels in the detector at the focal plane. While spectral range is not generally a limiting factor, a number of experiments have reported resolution-limited linewidths in photonic source characterisation with grating spectrometers [43, 182].

The SFPI is almost opposite in its attributes; the maximum scan range is limited by the free spectral range (FSR) of the cavity, which is inversely proportional to cavity length (L):

$$\mathrm{FSR} = \frac{c}{2L} \tag{2.9}$$

This means that to span 10 nm about a central wavelength of 900 nm, which would be straightforward with a grating spectrometer, would require the very short cavity length of 40 μm. It is evident then that the range that can be displayed in one spectrum is a limiting factor for SFPIs. The benefit is that they can far surpass the resolution of grating spectrometers for localised spectral features; the resolution depends on the cavity linewidth, which in turn depends on the reflectivity of the mirrors. With the high-reflectivity dielectric coatings that are commercially available, resolutions less than 1 picometer ($\equiv$ 1.5 μeV $\equiv$ 0.37 GHz) have been achieved [47, 46]. An additional consideration is the duration of the measurement; while grating spectrometers can take a simultaneous snapshot of all wavelengths in the spectrum, SFPIs scan the wavelengths sequentially, which requires significantly longer.

Table 2.1 quotes the spectral resolution achieved in various photon characterisation experiments. While these specifications surpass those of many commercial products at at telecom wavelengths (1310 nm and 1550 nm) [184], use of a SFPI could improve the resolution by two orders of magnitude. It is clear that both approaches have relative merits and offer complementary capabilities for the spectral characterisation of photonic sources.

λ	Instrument Resolution			Reference	Instrument Type
(nm)	μeV	GHz	pm		
914	1.24	0.3	0.84	[185]	SFPI
910	0.70	0.17	0.47	[47]	SFPI
920	0.06	0.015	0.04	[186]	SFPI
880	0.31	0.074	0.19	[46]	SFPI
850	0.02	0.004	0.01	[132]	SFPI
935	245	59	160	[187]	Grating spectrometer
920	70	17	47	[148]	Grating spectrometer
750	30	7.5	14	[188]	Grating spectrometer
926	29	7	20	[189]	Grating spectrometer
900	27	6.7	18	[190]	Grating spectrometer
920	20	4.8	14	[191]	Grating spectrometer
1300	36	8.7	49	[182]	Grating spectrometer
1300	30	7.3	41	[165]	Grating spectrometer
1550	51	12.1	97	[192]	Grating spectrometer

Table 2.1: **Spectral resolution of recent QD characterisation experiments.** Values from experiments at a range of wavelengths are quoted alongside the type of instrument used.

Chapter 3

Construction and characterisation of a superconducting nanowire single-photon detector system

3.1 Introduction

The goal of this project was to build and characterise an SNSPD system for use in NPL's single-photon metrology programme. The specification was for a two-channel system with at least 1 % system detection efficiency at 1 kHz dark count rate for a 1310 nm source. This is comparable to other SNSPDs reported around 2008 [193], when the project was commissioned. A system was constructed based on a prototype from NIST [194] that was further developed at Heriot-Watt University [195]. The nanowire devices were housed in a custom-built cryostat with a closed-cycle refrigerator providing a 3 K operating temperature. Each SNSPD device was packaged with optical and electrical connections to produce a practical system for use in a research laboratory.

This chapter describes the construction and characterisation of the SNSPD system, and reports on measurements that demonstrate its beneficial timing properties and low dark count rate compared to the existing single-photon detectors at NPL.

3.2 System construction

3.2.1 Nanowire devices

The nanowire devices used in this system were fabricated by S. Miki and coworkers at NICT, Japan [84]. A thin film of NbN (4 nm) was grown epitaxially on a room-temperature MgO substrate using sputtering-based deposition. The nanowire meander was etched using electron beam lithography, covering half of a 20 μm by 20 μm area with 100 nm-wide wires.

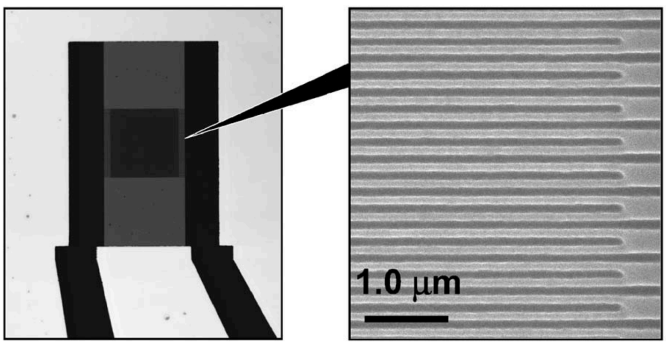

Figure 3.1: **Scanning electron micrograph of SNSPD.** *Left:* The nanowire meander (central square) embedded in a 50 Ω coplanar waveguide structure. *Right:* The inset shows the meander structure at a higher magnification (Image: Ref [84])

3.2.2 Optical and electrical connections

Light is delivered to the nanowires with an optical fibre that enters the cryostat via a custom-made vacuum flange. This improves shielding from room temperature blackbody radiation which could lead to an elevated operating temperature and increased dark count rate. Figure 3.2 shows the nanowire sample mount, which consists of two halves that are screwed together. One half of the mount holds the nanowire device and connects to it electrically while the other half holds the optical fibre. Some of the light from the fibre is transmitted straight through the nanowire device; a through hole in the sample mount allows this light to be observed with a camera. To align the optical fibre with the nanowire meander, the transmitted

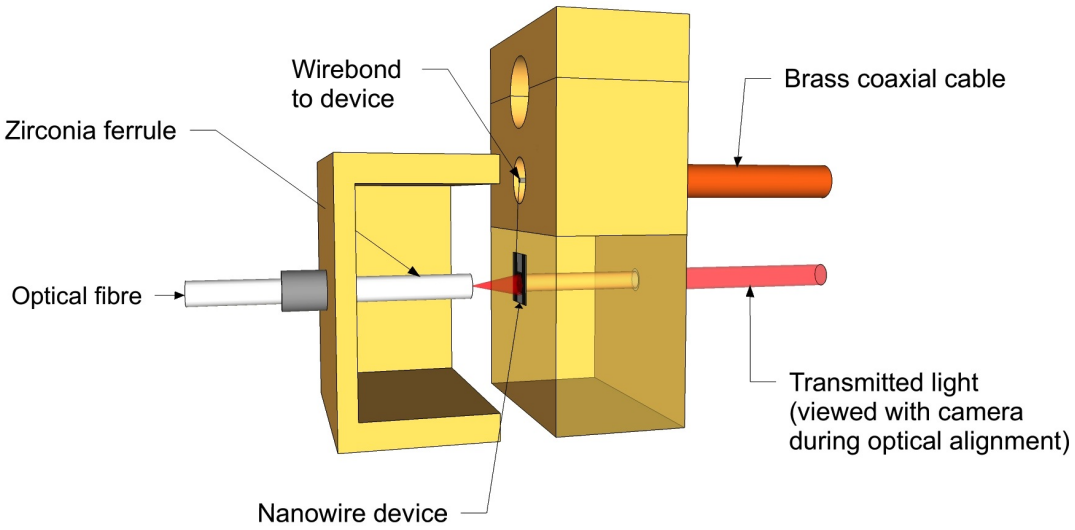

Figure 3.2: **Schematic of mounted SNSPD device.** Light is delivered to the nanowires via a single mode optical fibre; a through hole allows light that is transmitted through the nanowire device to exit the packaging and be observed with a camera during the alignment process. A wirebond connects the nanowires to a brass coaxial cable for bias current supply and event readout.

light was observed while the two halves of the sample mount were carefully screwed together. Images recorded with the camera during alignment are shown in Figure 3.3. Additionally, the separation between the fibre and the device was adjusted to match the beam spot area with that of the meander. The separation was adjusted using shims with thicknesses down to 25 μm and measured with white light interferometry using reflections from the device and the end of the fibre [196]. The measured separation was $\sim$ 40 μm at the system operating temperature (T = 3 K).

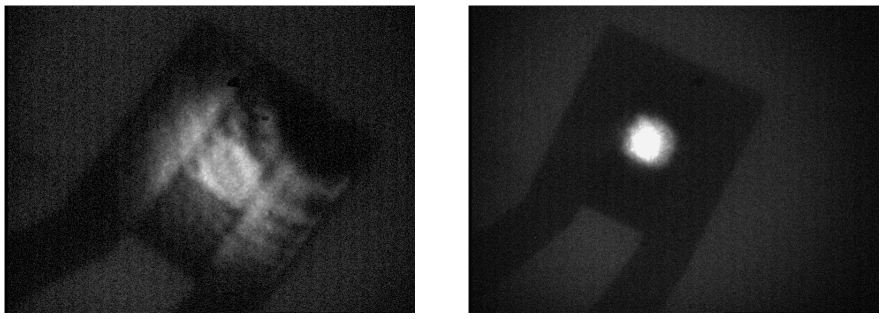

Figure 3.3: **Fibre alignment images.** Images of the nanowire device viewed from the position indicated in Figure 3.2. In the left image, the beam is misaligned and the fibre end is further away from the meander than in the final aligned position. The scattered light highlights the meander area in the centre of the device. In the right image, the beam is aligned with the meander area, which is a 20 μm by 20 μm square.

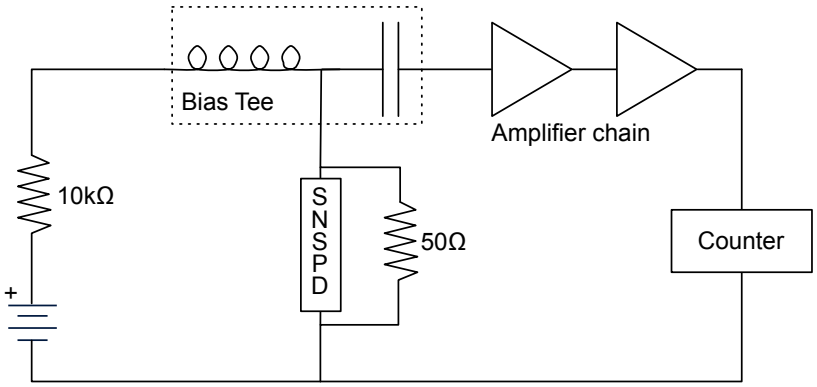

Figure 3.4: **SNSPD electrical circuit.** A 10 kΩ resistor and a stable voltage source provide bias current on the μA scale through the inductive arm of the bias tee, while the capacitive arm is used for event readout. The signal is amplified before proceeding to counting electronics. A 50 Ω shunt resistor in parallel with the nanowires provides an alternative path for current to flow while the nanowire recovers from a detection event, preventing latching.

Electrical connections between the cold nanowire devices and room temperature were made with brass coaxial cables. Brass was selected for its high electrical and low thermal conductivity to limit the heat load on the cold stage. Similarly, room temperature amplifiers placed just outside the cryostat were used to avoid the additional heat load of putting low-temperature amplifiers inside the cryostat. The electrical circuit is shown in Figure 3.4; a Picosecond Pulse Labs 5575A bias tee permits simultaneous bias supply through its inductive arm and event readout through its capacitive arm. Output pulses were amplified using two room temperature RF Bay amplifiers in series, one LNA-580 (23 dB gain from 10 MHz to 580 MHz) and one LNA-1000 (33 dB gain from 10 MHz to 1 GHz). A 50 Ω shunt resistor in parallel with the nanowire device provides a passive reset mechanism; as the resistance in the triggered nanowire increases, more of the current flows through the shunt resistor instead of the nanowire, which allows the nanowire to cool down and return to its superconducting state.

3.2.3 Cryostat system

In order to detect photons, the nanowires must be cooled to below their superconducting critical temperature ($\sim$ 12 K [84]). This was achieved with a closed cycle refrigerator (Sumitomo RDK-101D Gifford-McMahon cold head and CNA11C

compressor) - a practical solution that eliminates liquid cryogen handling and can cool several devices simultaneously [76, 194]. The cryostat arrangement is shown in Figure 3.5. The devices are mounted on the 3 K stage of the cold head, on top of a lead spacer to improve the temperature stability of the devices. To reduce dark counts due to blackbody radiation, the packaged devices are surrounded by a radiation shield that is mounted on the 40 K stage of the cold head. The assembly is enclosed in a vacuum chamber and evacuated to $\sim 1 \times 10^{-6}$ mbar. Once cold, the cryostat vacuum can be maintained for extended periods because any small gas leaks condense onto the cold head. Electrical and optical fibre feedthrough flanges were made in-house to provide the required connections to the nanowire devices.

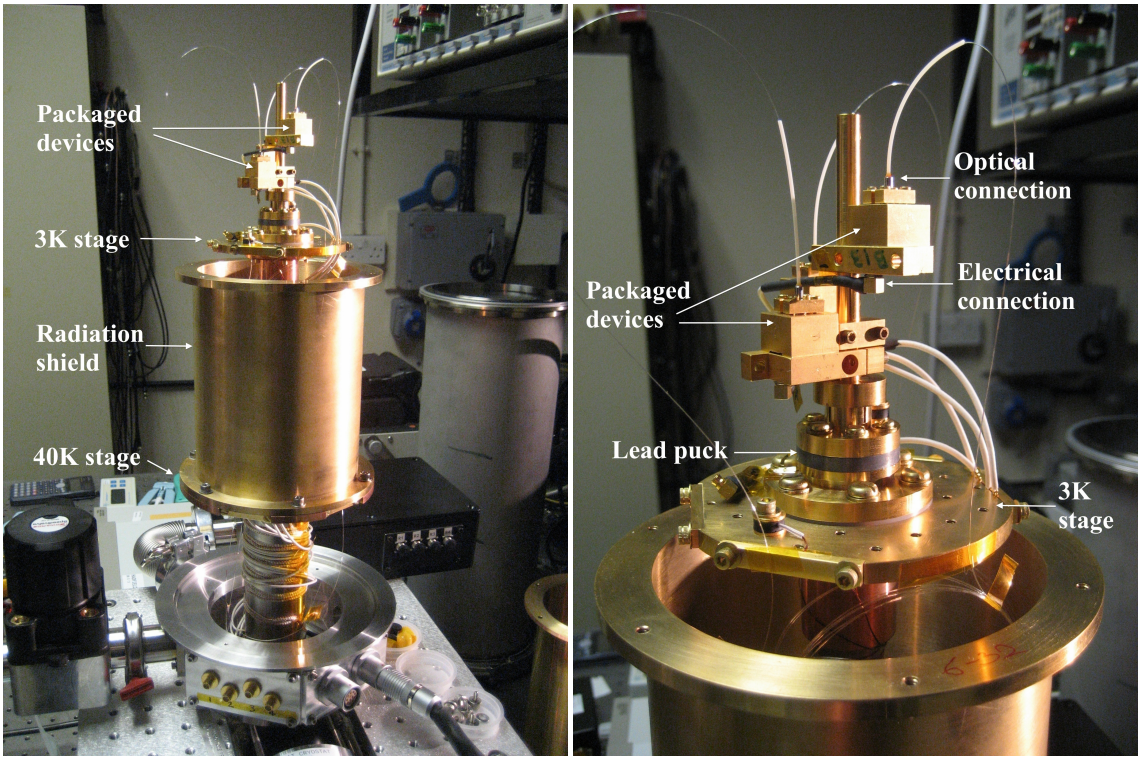

Figure 3.5: **Photographs of SNSPD cryostat assembly.** The packaged nanowire devices are mounted on the 3 K stage of a Sumitomo RDK 101D Gifford-McMahon cold head, surrounded by radiation shielding that is attached to the 40 K stage of the cold head. The nanowire temperature is stabilised by separating it from the cold stage with a lead puck, which has a long thermal time constant.

3.3 Characterisation experiments

The experiments described in this section characterise four key detector performance characteristics: jitter, reset time, detection efficiency and dark count rate. Measurements were performed at wavelengths of 830 nm, 1310 nm and 1550 nm. Two NbN nanowire devices (referred to as devices A and B) were mounted in the cryostat.

3.3.1 I-V characteristics

The current-voltage (I-V) characteristics of the nanowire devices were measured to determine their superconducting critical currents. The critical current is used as a reference for setting the bias current, as the efficiency of a device increases as the critical current is approached. Additionally, a critical current that is low compared to other devices with the same geometry can indicate constrictions, which limit the maximum detection efficiency [86, 87]. The I-V characteristics of device A are shown in Figure 3.6. The critical current was measured to be ∼17 μA for this device, and ∼15 μA for device B. These are reasonable values for devices with this geometry; the maximum recorded for similar devices was 20 μA [53].

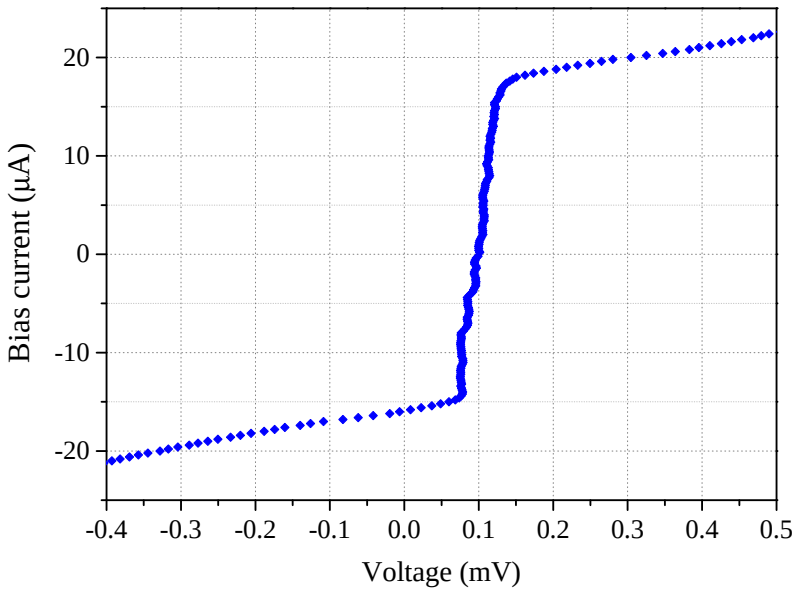

Figure 3.6: **SNSPD Device A - I-V characteristics.** The critical current is ∼17 μA. The low voltage region is non-zero due to the resistance of the wires used in the two-wire measurement arrangement.

3.3.2 System detection efficiency

For each device, the system detection efficiency was measured using the calibrated light source method [40]: The detector count rate was recorded for a range of calibrated levels of photon flux. When the photon flux is varied, the recorded count rate S takes the form

$$S = D + P_{rep}(1 - e^{-\eta\mu}) \tag{3.1}$$

where S is the count rate, D is the dark count rate, P_{rep} is the laser pulse repetition rate, μ is the average number of photons per pulse and η is the system detection efficiency, including optical coupling losses [40, 194].

The experimental arrangement that was used to deliver a known photon flux is shown in Figure 3.7; the average power from a gain-switched laser diode was measured with a calibrated power meter, then passed through calibrated optical attenuators (2 x Agilent 8156A, 120 dB total attenuation) and a polarisation rotator before reaching the nanowire device. Rotating the polarisation enabled the light to be aligned to the maximum and minimum absorption orientation for each device. Laser diodes at three operating wavelengths (830 nm, 1310 nm and 1550 nm) were gain-switched with a 1 μs repetition period to prevent the 10 ns detector dead time from limiting the results, and with a pulse duration of 10 ns to prevent multiple detection events being produced by the same pulse.

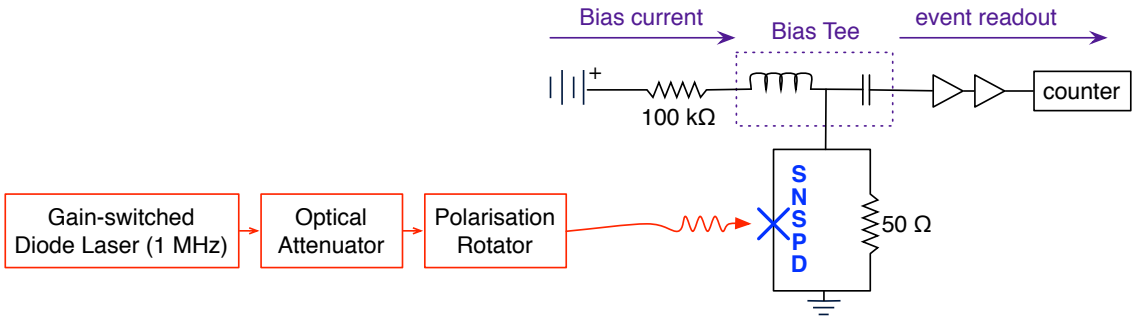

Figure 3.7: **Experimental arrangement to measure system detection efficiency.** An attenuated pulsed diode laser with a 1 MHz repetition rate was delivered to the nanowire device. The count rate was recorded as a function of increasing photon flux for a range of bias currents, using an Agilent 53131A universal counter/timer. Values for efficiency and dark count rate were obtained by fitting the data to Equation 3.1.

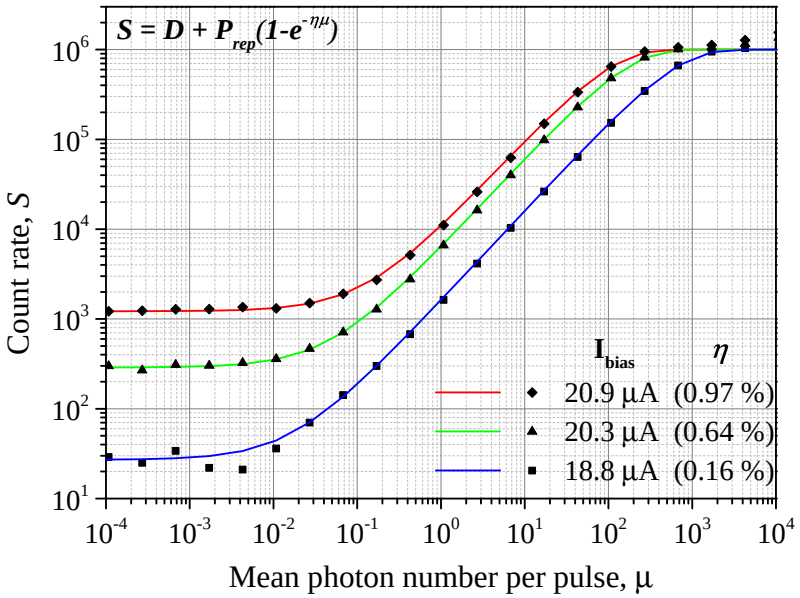

Figure 3.8: **SNSPD count rate versus incident photon flux at three bias currents.** Detection of single photons is shown by the order of magnitude increase in photon flux causing an order of magnitude increase in count rate. The detection efficiency increases with increasing bias current.

Figure 3.8 shows the variation of count rate with mean photon flux at three bias currents. Values for system detection efficiency and dark count rate at each bias point were obtained by fitting the data to Equation 3.1. The single-photon response of the detector is indicated by the slope in the central region of these plots; an order of magnitude increase in photon flux causes an order of magnitude increase in count rate. (If the detector required two photons to trigger an output pulse, the slope on this log-log plot would be halved). The saturation observed at high photon flux is the limit where detection events are recorded at the same rate as photon pulses are incident on the detector.

The three data sets shown in Figure 3.8 show clearly that the efficiency and dark count rate depend on bias current. Figures 3.9 and 3.10 show efficiency versus dark count rate measured at 30 bias currents and 3 wavelengths for both devices. These plots show that the dark count rate can be reduced from 1000 Hz to 100 Hz without incurring a proportional drop in efficiency, which can be useful in applications that prioritise a low dark count rate. Figures 3.9 and 3.10 also show that the target of 1 % efficiency at 1310 nm and 1 kHz dark count rate is met by both devices.

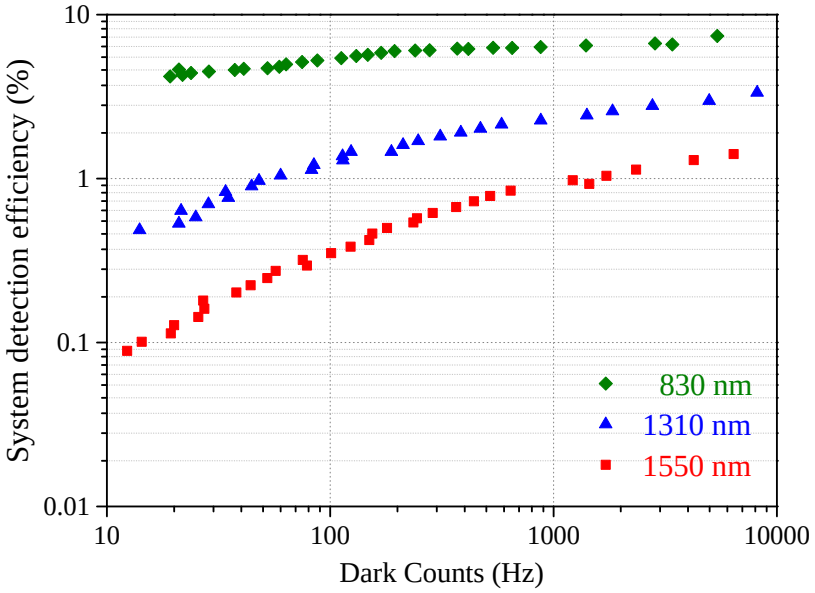

Figure 3.9: **Device A - System detection efficiency versus dark counts.** $\eta_{SDE} \approx 2.2$ % at λ =1310 nm and $D = 1$ kHz.

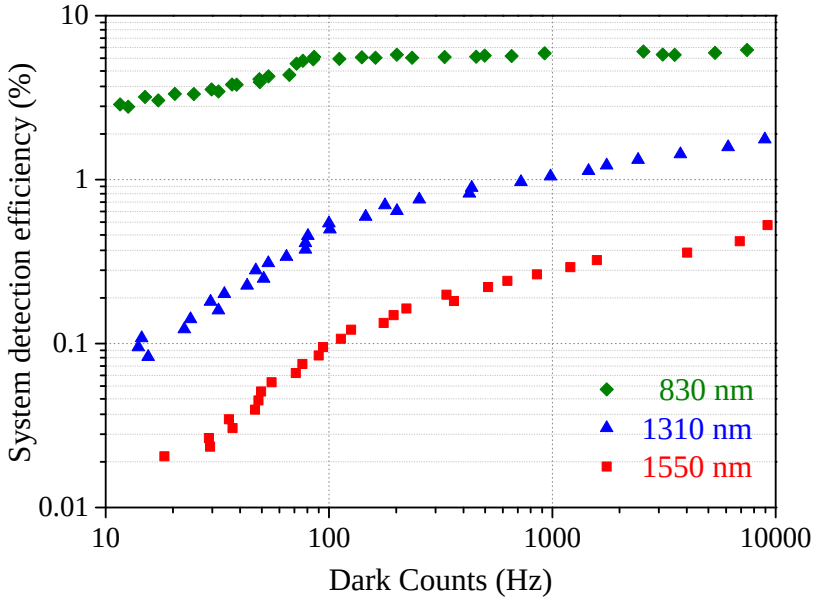

Figure 3.10: **Device B - System detection efficiency versus dark counts.** $\eta_{SDE} \approx 1.0$ % at λ =1310 nm and $D = 1$ kHz.

3.3.3 Reset time and timing jitter

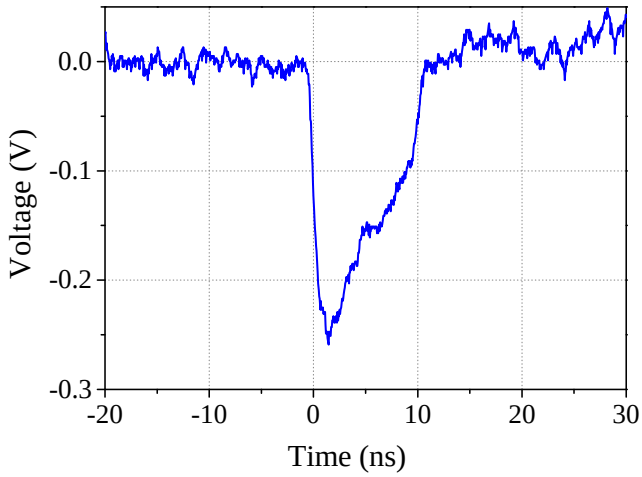

Figure 3.11: **Output pulse from SNSPD Device B.** The 10 ns pulse width limits the maximum count rate to 100 MHz; timing jitter is due to fluctuation in the leading edge.

A typical output pulse from the SNSPD system is shown in Figure 3.11. The reset time of the detector is estimated from the full width of the pulse to be $\sim$ 10 ns, making the maximum count rate $\sim$ 100 MHz. The timing jitter is much smaller than the pulse width because it only depends on the leading edge, which is triggered on to record detection events. The timing jitter of each device was measured using the arrangement shown in Figure 3.12. The output from a pulsed diode laser with a wavelength of 1550 nm and pulse duration below 50 ps (PicoQuant LDH-P-C-1550) was attenuated to the single-photon level and delivered to the SNSPD. Output pulses

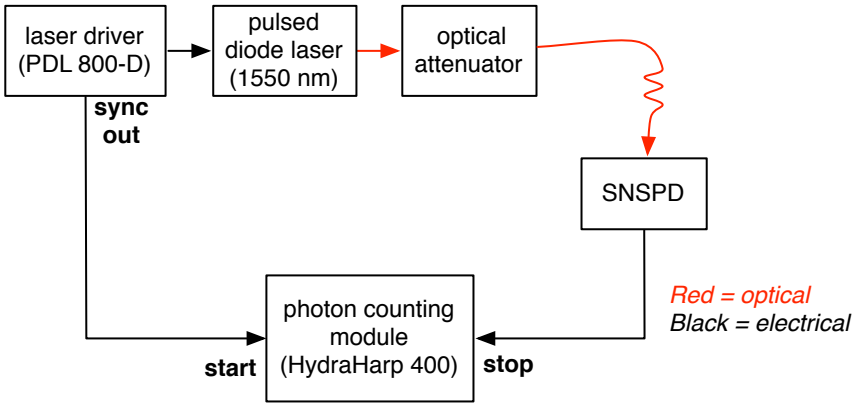

Figure 3.12: **Experimental arrangement to measure detector jitter.** A pulsed diode laser (PicoQuant LDH-P-C-1550) was attenuated and delivered to the nanowire device under test. Output pulses from the SNSPD were correlated with the electrical synchronisation signal from the laser driver using a PicoQuant HydraHarp 400 photon counting module.

from the SNSPD were correlated with the electrical synchronisation signal from the laser driver (PicoQuant PDL-800-D, electrical jitter < 20 ps) using a PicoQuant HydraHarp 400 photon counting module. Gaussian fits to the correlation histograms (shown in Figure 3.13) gave jitter values of 84 ps and 88 ps FWHM for devices A and B respectively. This includes a contribution from the laser and electronics; deconvolution indicated that the true values could be as low as 63 ps and 69 ps.

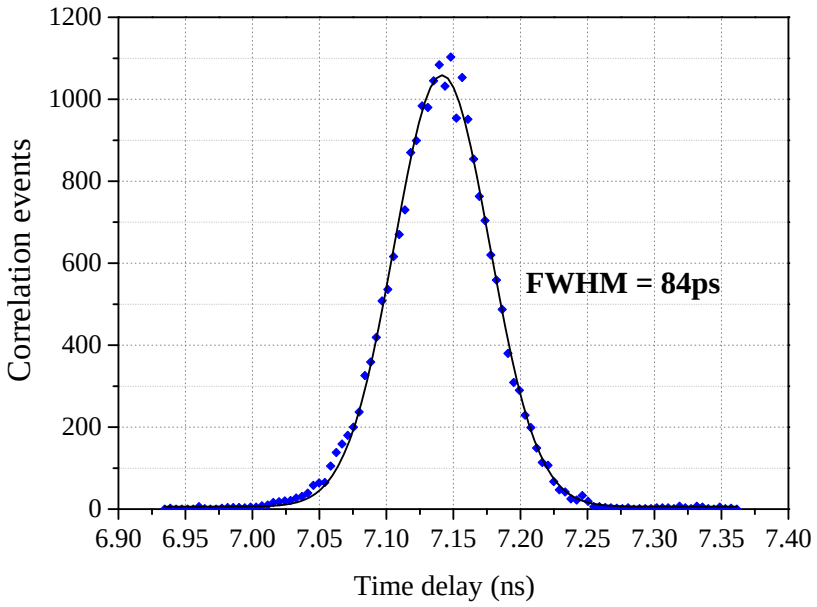

Figure 3.13: **Device A - Timing jitter.** A total jitter of 84 ps FWHM was measured using a Gaussian fit. This is primarily due to the jitter of the detector, with some contribution from the laser and correlation hardware.

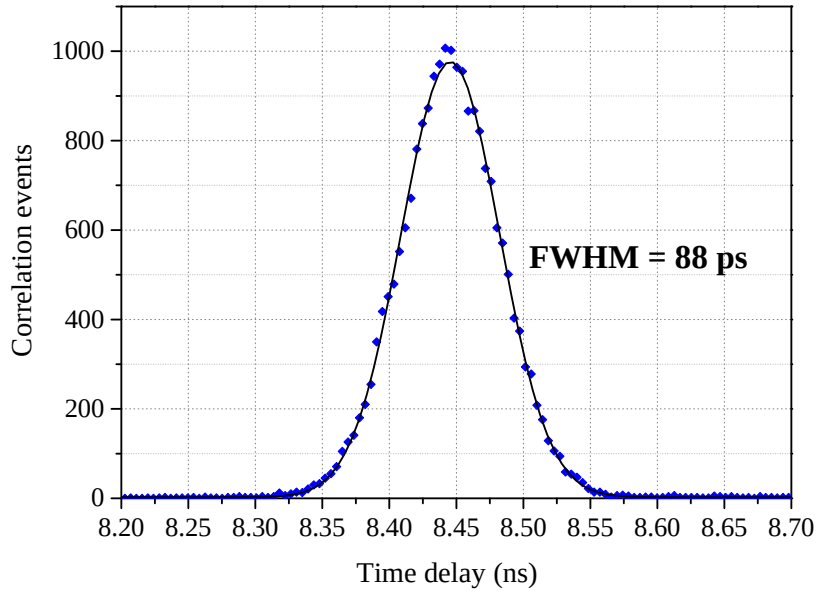

Figure 3.14: **Device B - Timing jitter.** A total jitter of 88 ps FWHM was measured using a Gaussian fit. This is primarily due to the jitter of the detector, with some contribution from the laser and correlation hardware.

3.4 Comparison of SPAD & SNSPD timing jitter

A key feature of SNSPD systems is their excellent timing resolution. To demonstrate their low jitter relative to the existing silicon SPADs at NPL, a comparison experiment was conducted. The experimental arrangement is shown in Figure 3.15; a pulsed optical signal was sent simultaneously to two detectors using a directional coupler, and detection events were correlated using a PicoQuant HydraHarp 400 photon counting module. The attenuated optical pulses were provided by an 82 MHz mode-locked Tsunami Ti:Sapphire laser operating at a wavelength of 905 nm with a 3 ps pulse duration. The HydraHarp has electrical timing jitter < 12 ps and was used to compile histogram data into 1 ps time bins. The measured correlation maxima all had widths greater than 100 ps, which was attributed to the convolved jitter of the two detectors.

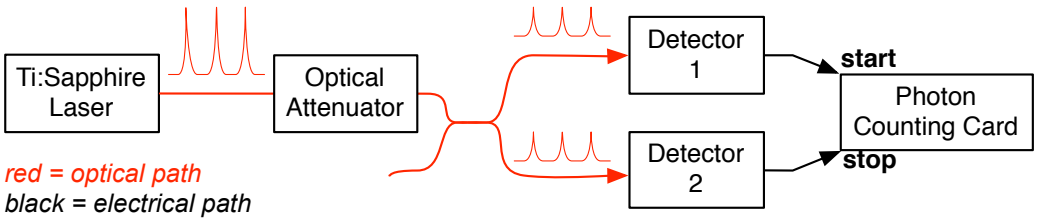

Figure 3.15: **Experimental arrangement to compare the jitter of two detectors.** Pulses from a Ti:Sapphire laser were attenuated and sent to both detectors using a fibre beam splitter. The events recorded on the two detectors were correlated using a PicoQuant HydraHarp photon counting module.

Three Perkin Elmer SPCM-AQRH silicon SPADs (numbered 1 to 3), were compared with each other and with the two nanowire devices in the SNSPD system. The results in Figure 3.16 show that the combinations containing SPAD 1 have considerably worse timing resolution. Deconvolution provided individual jitter values of 990 ps, 420 ps and 510 ps FWHM for SPADs 1, 2 and 3 respectively. Figure 3.17 shows the two best SPADs paired with an SNSPD device, and a measurement of the two SNSPD devices together. The improvement in timing resolution provided by the SNSPD system is clearly demonstrated.

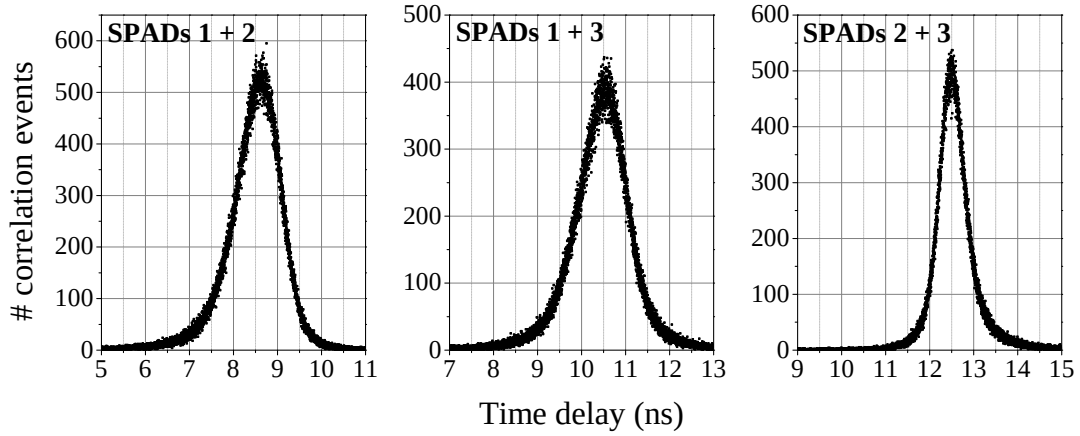

Figure 3.16: **Timing resolution: SPADs.** The three available SPADs were examined in the three possible pairings; the increased width of the first two maxima compared to the third indicates a larger timing jitter in SPAD 1. The deconvolved jitter values are 990 ps, 420 ps and 510 ps FWHM for SPADs 1, 2 and 3 respectively.

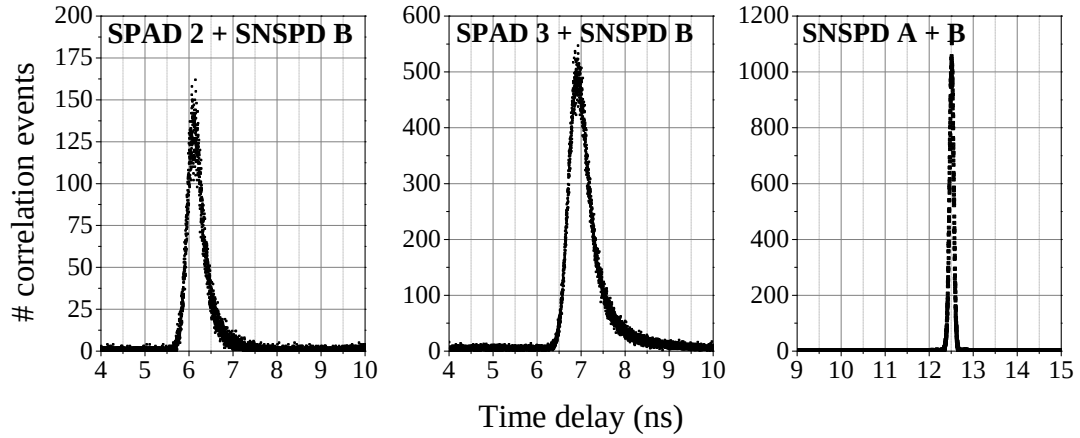

Figure 3.17: **Timing resolution: SPAD and SNSPD.** Histograms are shown with the same horizontal scale as Fig 3.16 to illustrate the low jitter provided by the SNSPD.

3.5 Conclusions and summary

In this project, a two-channel SNSPD system was constructed and characterised at Heriot-Watt University. It was delivered to NPL in December 2009 for use in a single-photon metrology research programme. The target of $\eta_{SDE} = 1$ % at a 1 kHz dark count rate for an input wavelength of 1310 nm was achieved, and the two nanowire devices were characterised as having maximum timing jitters of 84 ps and 88 ps FWHM. The 10 ns reset time, which is typical of devices with this geometry [84], permits count rates up to 100 MHz to be recorded. The air-cooled compressor allows the cryogen-free refrigerator to be operated continuously for weeks, or even months, from a standard 13 A mains power supply. and can support up to eight packaged nanowire devices. The capacity to electrically and optically connect to additional devices has been included in the original build to accommodate extended use of the system in future. The system is shown installed at NPL in Figure 3.18.

The SNSPD system as reported here has been used in the subsequent two chapters to characterise the temporal and spectral properties of quantum photonic sources. Since the construction of this system for NPL in 2009, the Heriot-Watt group have delivered SNSPD systems to the University of Toronto, Canada (2010), University of Bristol, UK (2011) and ID Quantique SA, Switzerland (2012). Additionally, all of the companies commercialising SNSPD technology [106] have adopted the cryogenic refrigeration approach used here in preference to reliance on liquid helium.

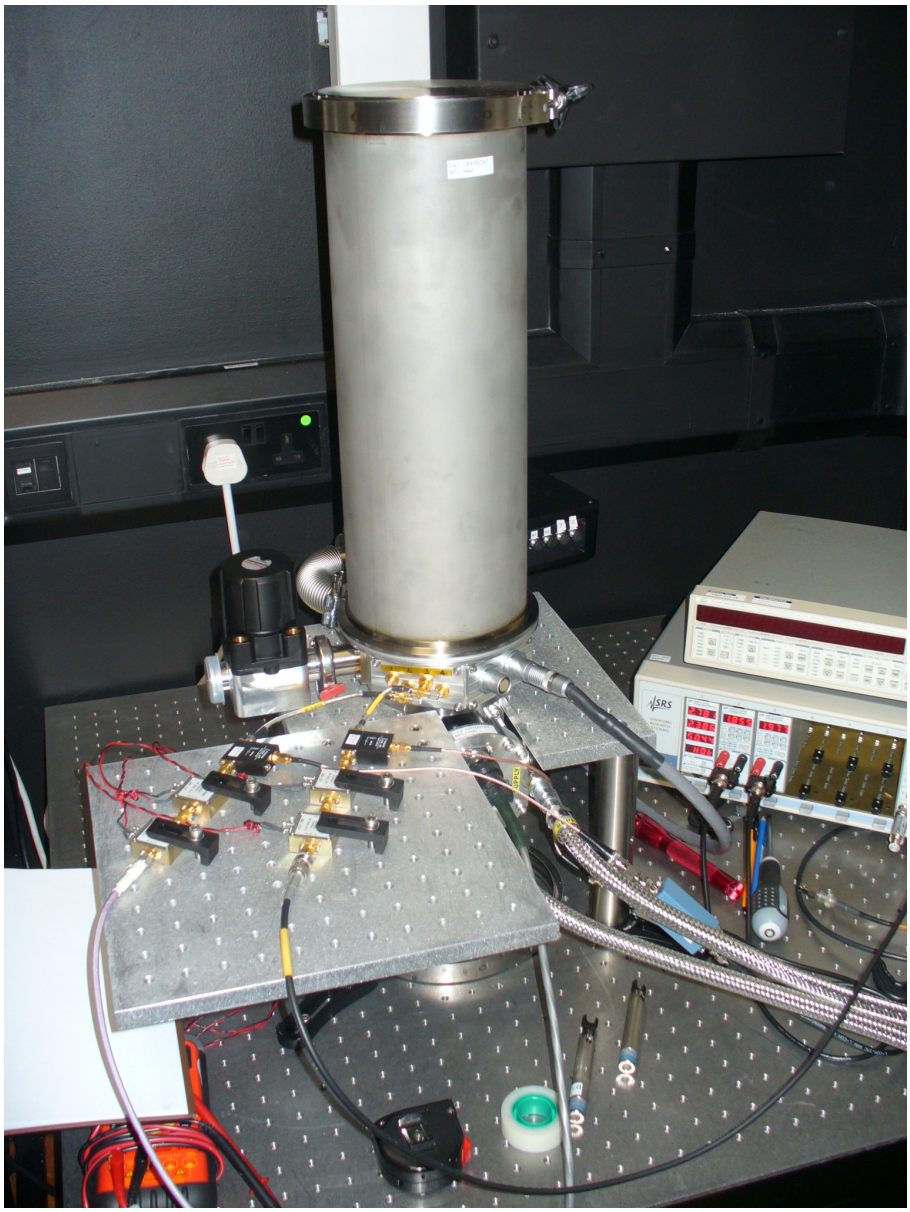

Figure 3.18: **Photograph of SNSPD system at NPL**

Chapter 4

Investigation of quantum dot single-photon sources

4.1 Background and project goals

The purpose of this project was to continue and develop NPL's work on single-photon source characterisation, with a focus on self-assembled quantum dots (QDs) in micropillar cavities. An experimental arrangement to investigate quantum emitters had been set up previously and used to characterise NV centres in diamond [161]. Initial measurements on a QD sample had identified three pillars with strong single-photon emission at wavelengths around 900 nm, and work to date had been carried out using silicon SPADs [187, 197].

Progression of this work involved further characterisation of the three emitters, including an investigation of the impact of pump wavelength on measurements of the second-order correlation function. Additionally, an experiment was designed and constructed to measure Hong-Ou-Mandel interference. It was planned to investigate the impact of detector jitter on interference visibility by comparing results obtained with the SPADs and the SNSPD system. Unfortunately the micropillars were damaged; when extensive efforts to locate comparable replacement micropillars were not successful, an alternative project was pursued (see Chapter 5).

4.2 Experimental arrangement

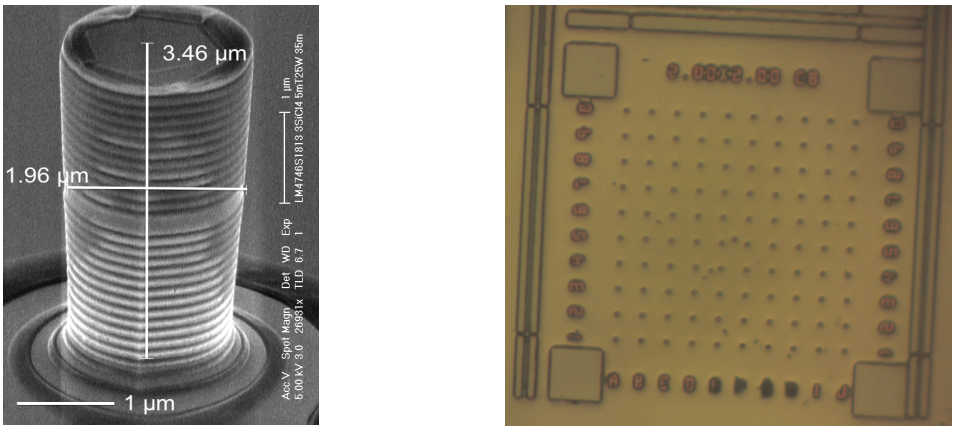

Figure 4.1: **Micropillar cavities containing a layer of QDs.** *(left)* A scanning electron micrograph of a single micropillar shows alternating layers of AlAs and GaAs surrounding a central layer of GaAs which contains InAs QDs. *(right)* An array of 100 micropillars; each array has a unique identifier code and alphanumeric indexing to faciliate repeated measurement of the same pillar.

The cavity structure was designed by Paul Stavrinou at Imperial College, London and grown via molecular beam epitaxy at the National Chiao Tung University, Taiwan. A central layer containing self-assembled InAs/GaAs QDs was sandwiched between two distributed Bragg reflectors, then etched into micropillar cavities by Patrick See (NPL). The distributed Bragg reflectors consisted of alternating layers of AlAs (77.8 nm) and GaAs (65.3 nm), with 30 pairs of layers below and 13 pairs above the central GaAs cavity (195.9 nm) which contained a layer of QDs. Figure 4.1 shows a scanning electron micrograph of a micropillar and a microscope image of a 10 x 10 micropillar array.

The experimental arrangement for isolating a radiative transition from a single emitter is shown in Figure 4.2. The QD sample was mounted in a Helium flow cryostat next to a confocal microscope which was mounted on a translation stage in order to align the focus with specific micropillars. One end of an endlessly single-mode photonic crystal fibre was used as the confocal pinhole, which decoupled the alignment with the micropillars from the rest of the optics and facilitated pump delivery and emission collection in a single mode, regardless of wavelength. This confocal microscope arrangement was reported in Ref [198].

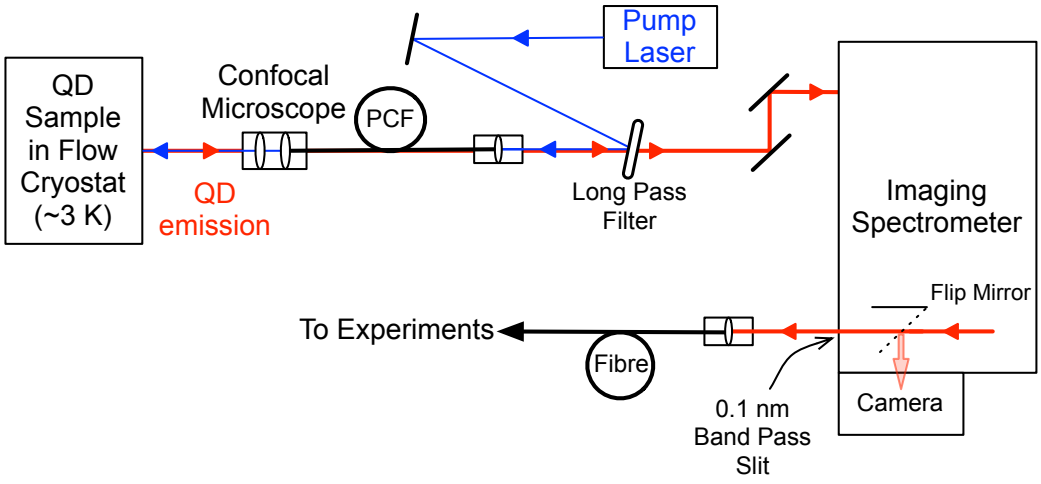

Figure 4.2: **Experimental arrangement of the QD single-photon source.** QDs in a Helium flow cryostat were optically pumped with a range of different pump lasers. The emission was collected via a confocal microscope arrangement that used the photonic crystal fibre (PCF) as the confocal pinhole. The emission was directed into an imaging spectrometer, where a flip mirror allowed the full spectrum to be observed with a camera before directing specific radiative transitions through the 0.1 nm band pass front exit.

The QD sample was optically pumped at normal incidence and the emission was collected with the same optics. A long-pass filter removed any reflected pump before the emission entered a Horiba iHR550 imaging spectrometer (focal length = 0.5 m). In conjunction with a flip mirror and an Andor electron-multiplying charge-coupled device, the spectrometer arrangement could be used to observe a spectral range of $\sim$ 20 nm with a resolution of 0.16 nm [187]. This enabled individual transitions to be identified and directed to the 0.1 nm band pass slit, where the transmitted light was fibre-coupled for delivery to multiple experiments.

4.3 Single-photon source identification

The ideal micropillar would contain a single QD positioned centrally in the cavity layer to optimise coupling to the cavity. Additionally, the exciton emission would be resonant with the cavity at a low temperature to minimise phonon contributions to emission dephasing. To this end, the cavity structure was designed to match the anticipated QD size distribution. Initial characterisation of the sample allowed sections to be selected for their relatively low QD density, to increase the probability

of isolating a single QD. The micropillars were investigated by optically exciting them individually and examining the emission spectrum. Each micropillar exhibits a relatively broad spectral feature; this is a common observation, thought to originate from sub-bandgap or wetting layer emission being filtered by the cavity structure [180]. The large free spectral range of the cavity ($\sim$ 200 THz) means that only one such feature is present in the recorded spectra, the width of which indicates the quality of the cavity as determined by the Q-factor ($Q = \Delta\lambda/\lambda$). In Figure 4.3, the Q-factor was calculated to be 1135.

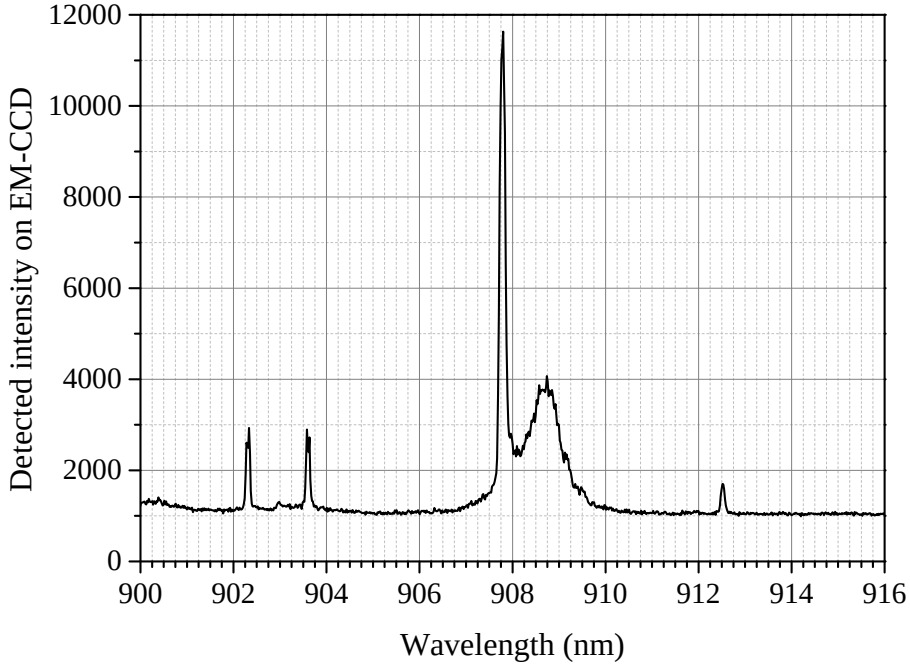

Figure 4.3: **Photoluminescence spectrum from pillar G4.** Sharp spectral features are due to QD transitions, while the wider feature is broadband emission that has been filtered by the cavity. The Q-factor of the cavity $Q = \Delta\lambda/\lambda = 1135$.

The QD and cavity lines can be tuned into resonance by exploiting a difference in the thermal expansion coefficients of the two structures. Figure 4.4 shows the exciton emission from a QD tuned into resonance with the cavity mode, and Figure 4.5 a) shows the emission intensity reaching a maximum as the cryostat temperature is varied. The exciton emission can be identified because its intensity increases linearly with pump power before it saturates, while biexcitons exhibit quadratic behaviour [173]. Figure 4.5 b) shows that the selected transition line is the QD exciton.

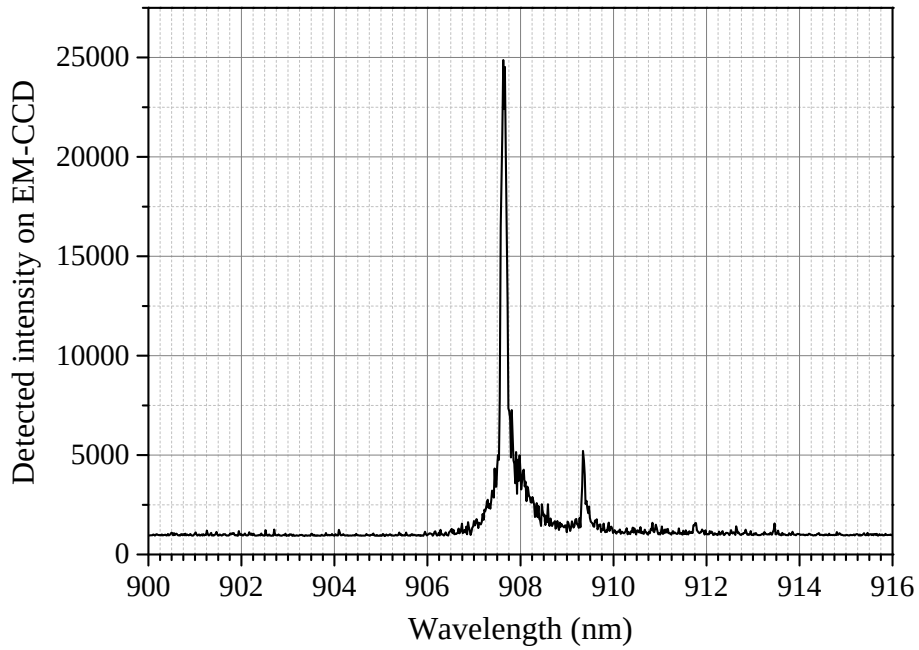

Figure 4.4: **Photoluminescence spectrum from pillar C0.** In this spectrum, the exciton emission from a QD in the pillar has been tuned into resonance with the cavity mode.

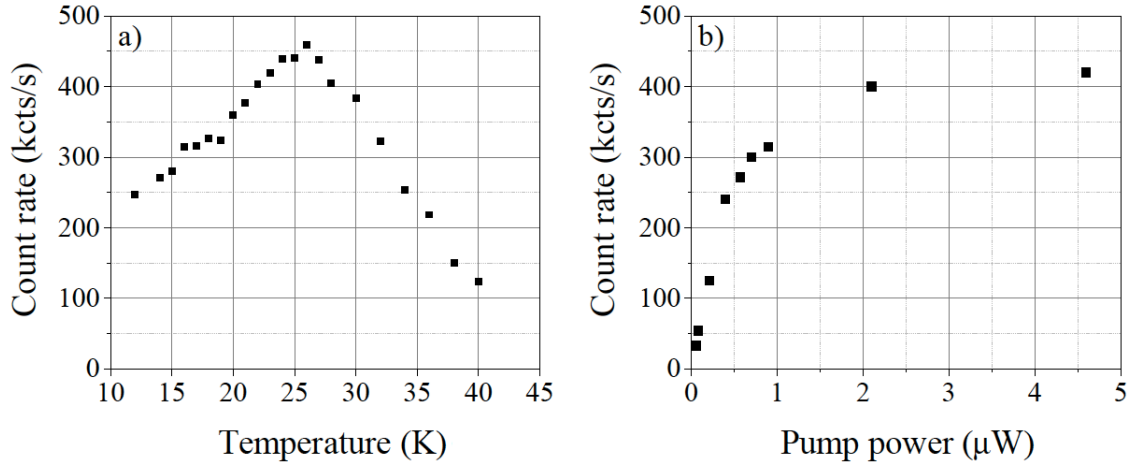

Figure 4.5: **Characterisation of exciton line from pillar C0.** a) Emission intensity versus cryostat temperature with pump power fixed at P = 1 μW. This is the exciton transition, which saturates around 4 μW and is on resonance with the cavity at a temperature of 26 K; b) Emission intensity versus pump power with cryostat temperature fixed at T = 27 K.

4.4 The second-order correlation function

Section 2.2.2 introduced the second-order correlation function $g^{(2)}(\tau)$ and its relation to photon statistics. It is measured with a Hanbury Brown and Twiss interferometer, which correlates the detection events on the two output ports of a beamsplitter. A perfect single-photon source cannot make both detectors fire simultaneously, which prevents correlation events occurring at zero time delay (*i.e.* $g^{(2)}(\tau = 0) = 0$). The lowest measurable value of $g^{(2)}(\tau = 0)$ is increased by imperfect experimental conditions such as detector dark counts, timing jitter and finite time-binning in the correlation process. It is therefore important to optimise the experiment in order to obtain the most accurate data on the performance of the source.

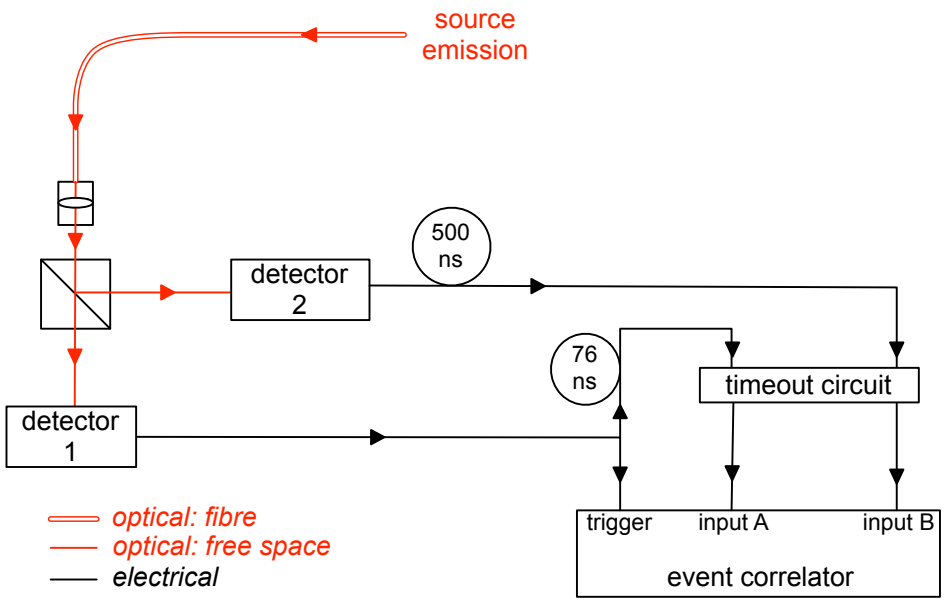

Figure 4.6: **Experimental arrangement - Hanbury Brown and Twiss interferometer.** Light is delivered to a beamsplitter that has a detector at each output port. The detectors are connected to a correlator via fixed time delays to compile a correlation histogram that includes events above and below zero time delay.

The second-order correlation function was measured using the experimental arrangement shown in Figure 4.6. The correlator used was a HP 52210A modulation domain analyser; it was operated in interval measurement mode, which histograms the time delay between events on the two input channels into 445 ps time bins. This is comparable to the jitter of the SPADs, which was measured in Section 3.4 to be

420 ps and 510 ps (FWHM) for the best two detectors. A timeout circuit limited the maximum time delay by generating a false detection event after a set period.

In previous work, the second order correlation function was measured with a CW pump laser [187]; Figure 4.7 shows one of the correlation histograms that were acquired from pillar C0, giving $g^{(2)}(\tau) = 0.13$. In the current work, the same pillar was pumped using a Spectra Physics Tsunami pulsed Ti:Sapphire laser (82 MHz rep rate, wavelength = 800 nm). The resulting periodic photon emission produced a comb of maxima in the correlation histogram that were separated by the 12.2 ns laser repetition period. The absence of a feature at zero time delay is equivalent to the reduction in correlation events in the CW data. The pulsed correlation histogram in Figure 4.8 was analysed to obtain $g^{(2)}(\tau = 0) = 0.12 \pm 0.04$, which agrees with the CW value within uncertainties.

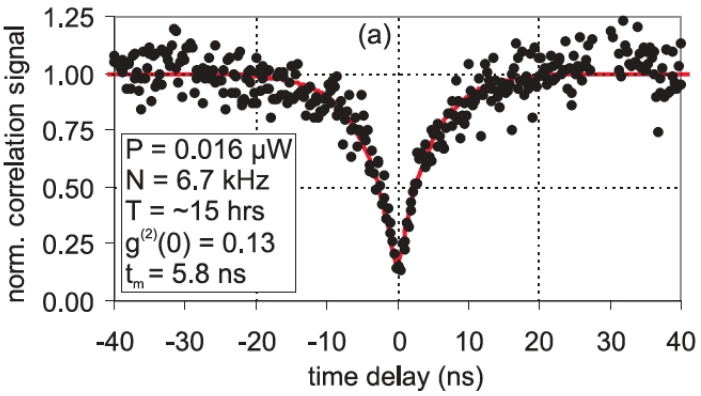

Figure 4.7: **Correlation histogram - Pillar C0, CW pump laser (Source: [187])** The histogram was recorded at a pump power below the saturation point for a period of $\sim$ 15 hrs. The measured value of $g^{(2)}(\tau = 0)$ was 0.13, with no background subtraction.

All initial measurements used above-band pumping, where micropillars are optically excited with sufficient energy to create electron-hole pairs in the bulk semiconductor, which then drift into the QD potential and recombine to produce photons. Improvements in the signal-to-noise level have been reported by exciting QDs near-resonantly [178], which creates electron-hole pairs directly in excited states of the confinement potential. Provided that no nearby QDs have degenerate energy levels, pumping near-resonantly selects a specific QD, which reduces unwanted contributions from other nearby QDs. It also prevents the formation of charged exciton states, which have uneven numbers of electrons and holes, and reduces the commonly-observed

broadband emission surrounding the exciton states [199]. The second-order correlation function of the same pillar was measured under near-resonant excitation by tuning the Ti:Sapphire laser to a wavelength of 880 nm. As before, the emission was collected with two Perkin-Elmer silicon SPADs. The resulting histogram is shown in Figure 4.9, which shows a clear reduction in the background level in the data and gives $g^{(2)}(\tau = 0) = 0.07 \pm 0.05$. While this is lower than the previous measurement, they overlap in their uncertainty bounds. If this project had continued, it would have been desirable to acquire larger data sets under both pump conditions in order to reduce the statistical uncertainties, and to investigate using fitting techniques in order to apply appropriate background subtraction.

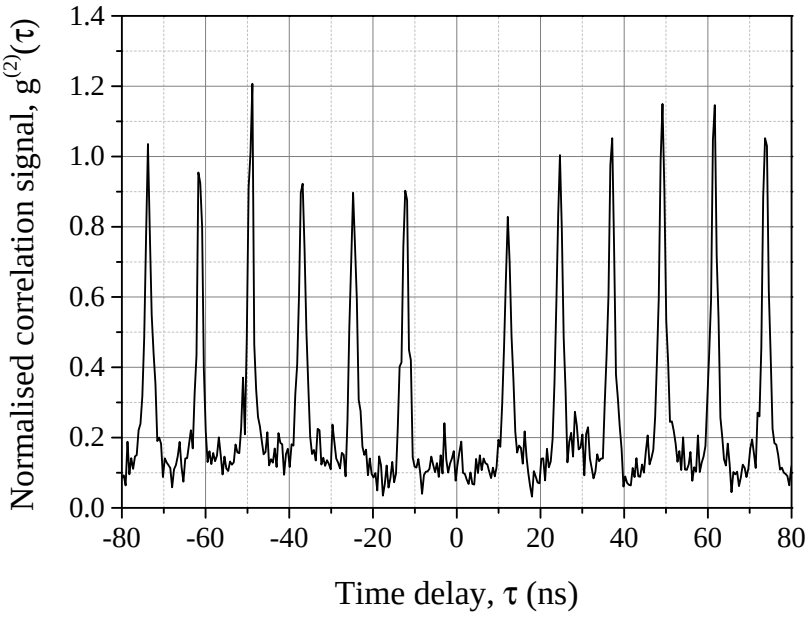

Figure 4.8: **Correlation histogram - Pillar C0, above-band pulsed optical excitation (λ = 800 nm).** Recorded at an average power of 0.044 μW for a period of 15 hrs. Raw data is shown; no background subtraction was applied. A comparison between the maxima and the central region gave $g^{(2)}(\tau = 0) = 0.12 \pm 0.04$.

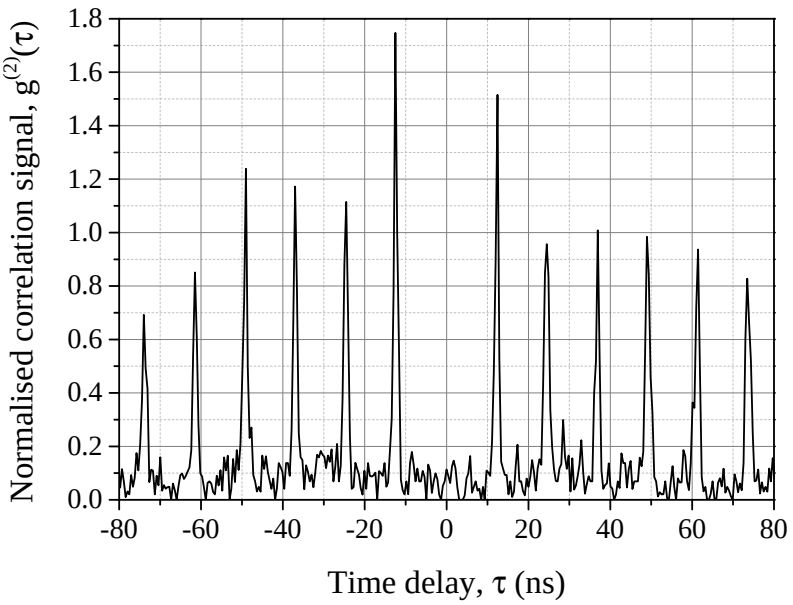

Figure 4.9: **Correlation histogram - Pillar C0, near-resonant pulsed optical excitation (λ = 880 nm).** Recorded at an average power of 20 μW for a period of 53 mins. Raw data is shown; no background subtraction was applied. A comparison between the maxima and the central region gave $g^{(2)}(\tau = 0) = 0.07 \pm 0.05$.

4.5 Two-photon interference experiment

The indistinguishability of two photons can be quantified by measuring two-photon interference with a Hong-Ou-Mandel interferometer (described in Section 2.2.3). In this experiment, two photons overlap at a beamsplitter and the detection events at the output ports are correlated. For indistinguishable photons, two-photon interference prevents correlation events occurring at zero time delay. This is quantified experimentally by measuring the reduction in correlation events as the time delay between the two photons is tuned through zero. An experiment to measure two-photon interference for successive photons from a QD single-photon source was designed and constructed. The QD sample was damaged before this arrangement could be used to characterise single photons; the design of the experiment is presented herein, alongside projected event rates that demonstrate its feasibility.

In order for two-photon interference to occur, it is essential that the two photons arrive simultaneously and overlap spatially at the designated point. It must also be possible to vary the time delay between the two photons, in order to scan through the zero delay point and measure the change in correlation events. It was planned to control the temporal separation between pairs of photons by using pairs of pump pulses with an adjustable delay (Δt_{pair}) to excite the QD sample. The pump pulse delay generator is shown in Figure 4.10; the output from a pulsed laser is divided at a beamsplitter, half of it travels a longer path, then the two beams are recombined to produce pairs of pump pulses. The delay between the two paths was made adjustable by fitting a retroreflector on a translation stage in the long path. This arrangement was carefully aligned to ensure that the coupling efficiency into the output fibre ($\sim$ 75 %) remained constant while translating the retroreflector over a distance of 6 cm, corresponding to a free-space delay adjustment of 0.2 ns. In order to tune fully across the region of photon overlap, the range of adjustment should be at least three times longer than the lifetime of the source; this means that in practise, the delay in the prepared experiment would have needed extending to meet the requirements of the source.

Once a pair of pump pulses has produced a pair of single photons, an arrangement is required to make them overlap. A Mach-Zehnder interferometer (shown in Figure 4.10) was constructed from polarisation maintaining directional couplers for this purpose. A fixed path difference between the arms of the interferometer ($\Delta t_{\text{interferometer}}$) was designed to be within the range of the tuneable pump pulse delay. When the two delays are matched, the two photons overlap at the second directional coupler if the first photon takes the long path and the second photon takes the short path. The photons can also take other combinations of paths through the interferometer, resulting in temporal separations of Δt_{pair} if both photons take the same path, and $2\Delta t_{\text{pair}}$ if the first photon travels the short path and the second photon travels long path. This produces a set of five maxima as shown in Figure 4.11. The time delay Δt_{pair} was initially set to 2.2 ns, then extended to 3.2 ns in order to be approximately three times longer than the typical exciton lifetime. This arrangement is expected to produce distinct correlation maxima, facilitating straightforward analysis of any reduction in correlation events in the region where the photons overlap.

The arrangement in Figure 4.10 was characterised by directly connecting the pulse delay generator to the Mach-Zehnder interferometer and measuring attenuated optical pulses from a Spectra Physics Tsunami Ti:Sapphire laser (modelocked with an 82 MHz repetition rate). Correlation events were detected using the SNSPD and a PicoQuant HydraHarp 400 photon counting module. Figure 4.12 shows the correlation maxima that were observed when the interferometer and pump pulse delays were matched and slightly mismatched. The timing resolution of the SNSPD was beneficial in accurately determining the zero delay point; the illustrated mismatch of 160 ps would have been difficult to discern using SPADs with 420 ps FWHM jitter.

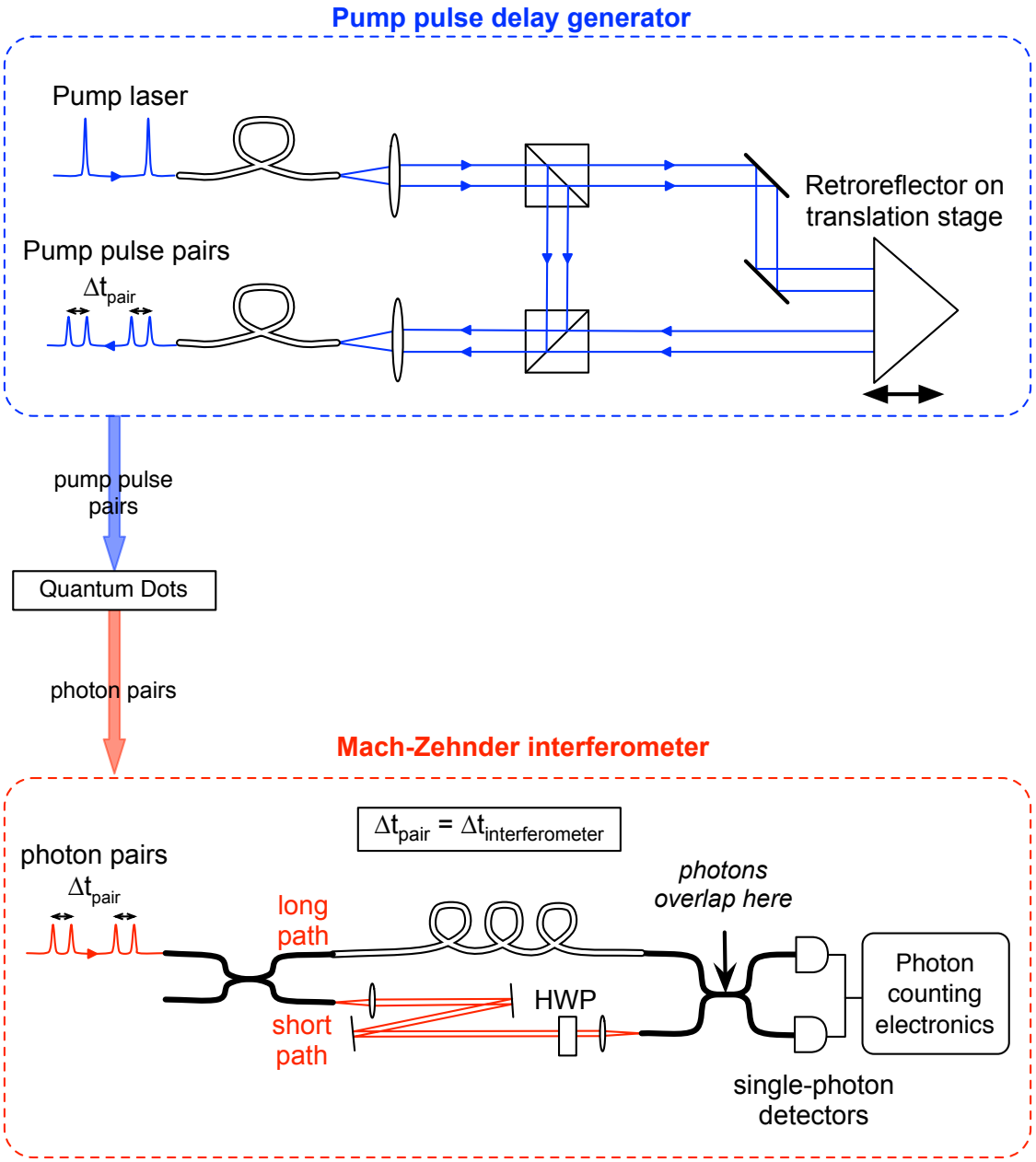

Figure 4.10: **Experiment to measure Hong-Ou-Mandel Interference.** Pairs of pump pulses are generated by dividing each pulse and delaying half of it. The delay is provided by a long path which can be adjusted using a retroreflector on a translation stage. Pump pulse pairs are delivered to the QD sample to produce pairs of single photons, which are delivered to a Mach-Zehnder interferometer that is primarily constructed from polarisation-maintaining optical fibre. The fixed path difference of the interferometer lies in the range of the tuneable pump delay. By scanning the pump pulse delay, the generated photons can overlap at the indicated position. A half-wave plate (HWP) in the short path of the interferometer allows the relative polarisation of the two photons to be adjusted.

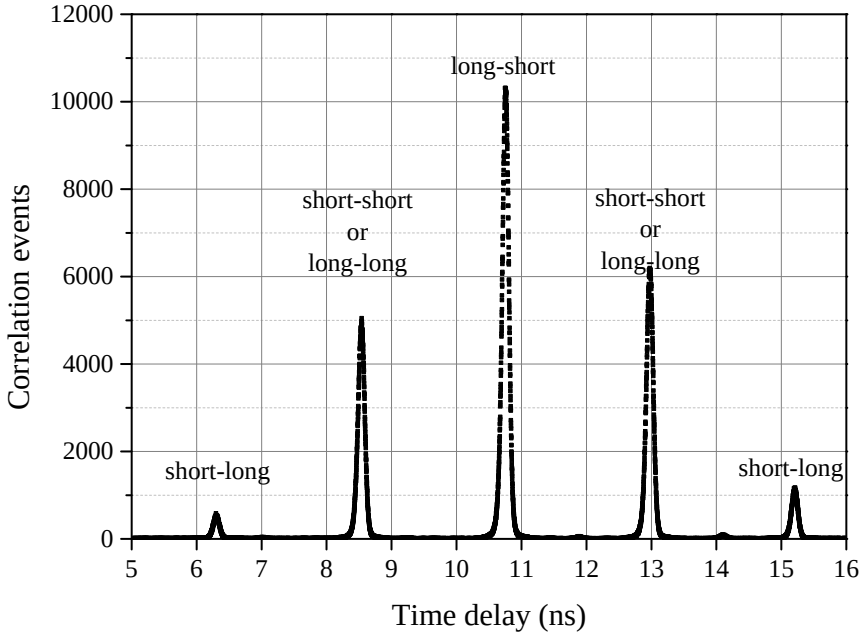

Figure 4.11: **Correlation maxima due to different path combinations through a Mach-Zehnder interferometer.** Photon pairs separated by time Δt_{pair} pass through a fibre Mach-Zehnder interferometer with a path difference $\Delta t_{\text{interferometer}} = \Delta t_{\text{pair}}$ (shown in Figure 4.10). When the first photon follows the long path and the second photon follows the short path, they arrive simultaneously at the second directional coupler; this is recorded as a delay of ∼11 ns due to a fixed temporal offset between the start and stop detectors. Additional maxima occur when the photons do not arrive simultaneously at the second directional coupler, appearing at time delays $\pm\Delta t_{\text{pair}}$ and $\pm 2\Delta t_{\text{pair}}$ because the start detector can be triggered by the first photon to exit or by the delayed photon.

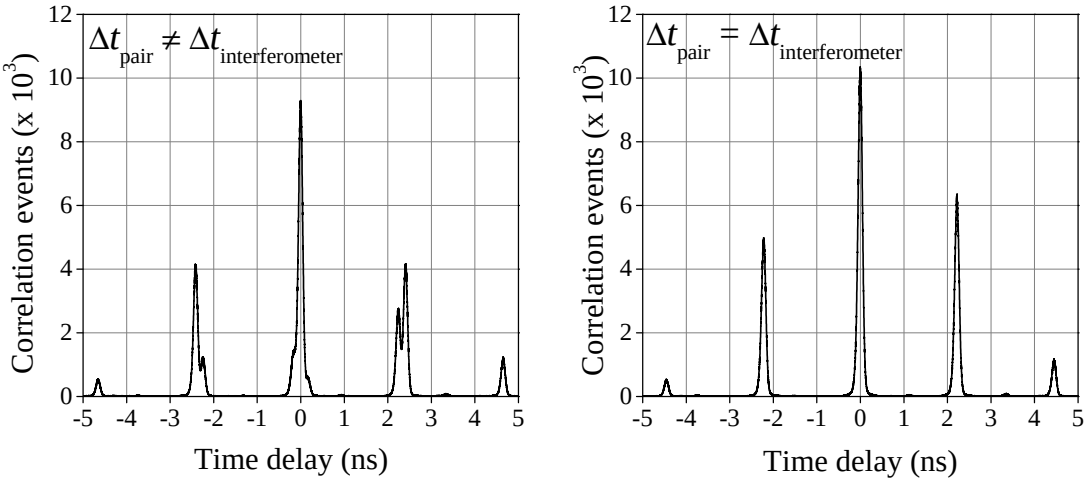

Figure 4.12: **Temporal alignment data from Hong-Ou-Mandel experiment.** A mismatch between the delays of 160 ps is observed to have a significant effect on the correlation histogram; the timing resolution of the SNSPD system provides the ability to align the delays Δt_{pair} and $\Delta t_{\text{interferometer}}$ with this level of accuracy.

In the planned experiment, the rate of correlation events is influenced by both coupling efficiencies and splitting ratios. The splitting ratio of the directional couplers was found to be sensitive to input wavelength, but was confirmed to meet the 50:50 specification at the design wavelength of 905 nm. The ratio was also found to depend on polarisation. In the most extreme case, the power splitting changed from 50:50 to 6:94 when the polarisation was aligned to the fast axis rather than the slow axis. It would be necessary to account for this when planning measurements with rotated polarisation, to ensure that comparable statistics were acquired.

The feasibility of the experiment is demonstrated by projecting the rate of correlation events for distinguishable photons. This is the baseline against which any reduction in correlation events would be measured. The calculation begins with the 82 MHz pump laser, assuming that every pump pulse creates an exciton in the QD, then accounts for all efficiencies and probabilities that affect the transmission from the QD sample to the outputs of the Mach-Zehnder interferometer. The steps can be outlined as follows:

1. Extraction efficiency: The maximum extraction efficiency that has been achieved with single-photon sources based on QDs in micropillar cavities is ~ 40 % [116]. This is the efficiency with which photons emitted by a QD are collected by the first lens. While this quantity was not characterised for the experimental arrangement, it was carefully designed and arranged to be optimal as outlined in Ref [187]. The extraction efficiency was therefore estimated to be 35 %.

2. Transmission efficiency: The efficiency with which photons are transmitted from the first lens to the fibre after the spectrometer (through the experimental arrangement shown in Figure 4.2) was measured to be 11 % [187]. For this experiment, the fibre after the spectrometer is the first fibre in the Mach-Zehnder interferometer shown in Figure 4.10.

3. Probability of consecutive photons: The probability that a pulse contains a photon at the point of entering the interferometer was calculated by dividing the rate of transmitted photons by the laser repetition rate. Applying conditional probability, this value was squared to determine the likelihood of two

consecutive photons being coupled into the interferometer.

4. Probability of correct paths for photon overlap: In order to overlap at the second directional coupler, the first photon must take the long path and the second photon must take the short path. For a coupler with a perfect splitting ratio each of these events occur with 50 % probability, so the probability of both occurring is 25 %.

5. Transmission through the Mach-Zehnder interferometer: The rate of photon overlap events is limited by the least efficient path through the apparatus. This is the free space path, which was characterised to have a transmission efficiency of 82 %.

6. Probability of photons exiting opposite ports: In the case of distinguishable photons, this is 50 %.

7. Probability of detecting a correlation event: This is the square of the detection efficiency.

In addition to real correlation events, background events arise due to correlations between dark counts, and between dark counts and real detection events. Those events that occur in the same temporal region as the maxima shown in Figure 4.11 affect the signal to noise ratio of the measurement. Estimates for the rates of real and background correlation events have been calculated for both SPADs and the SNSPD considering integration over a time bin of 3.2 ns. This is the maximum range that can be integrated over in this experimental arrangement, which is sufficient for exciton lifetimes up to $\sim$ 1 ns. The estimate has been repeated for a smaller time bin for the SNSPD, to indicate the improvement that could be provided by its lower timing jitter. Here, the time bin for integration was deetrmined by combining three times the exciton lifetime measured in Ref [187] (420 ps) with a jitter of 90 ps for each of two SNSPD channels (see Section 3.3.3), to give a time bin of 1.3 ns for integration. In such an experiment, the SNSPD would be operated at a point with low dark counts in order to optimise the signal to noise ratio. The operating point was taken from experimental data for λ = 830 nm in Figure 3.9. The results in

Table 4.1 indicate that in all cases, the rate of real correlation events would be significantly higher than the rate of events arising due to correlations with dark counts, suggesting that data acquisition for the planned experiment would have been feasible. The results also indicate that the ability to integrate over a smaller time bin with the SNSPD would provide a higher ratio of real to dark correlation events.

	SPAD	SNSPD (1)	SNSPD (2)
Detection efficiency (η_{SDE}), %	35	4.5	4.5
Dark count rate (D), Hz	100	20	20
Time bin for integration	3.2	3.2	1.3
Correlation event rate: real, s^{-1}	59	0.97	0.97
Correlation event rate: dark, s^{-1}	1.1×10^{-4}	2.8×10^{-6}	1.1×10^{-6}
Ratio of real to dark correlation events	5.5×10^{5}	3.5×10^{5}	1.1×10^{6}

Table 4.1: **Projected correlation event rates for distinguishable photons in the planned two-photon interference experiment.** Event rates for the SPAD and SNSPD (1) were estimated for integration over a 3.2 ns time bin, and for SNSPD (2) using a time bin of 1.3 ns to indicate the potential improvement due to lower timing jitter.

4.6 Conclusions and summary

The second order correlation function for cavity-enhanced QD exciton emission was characterised at above-band and near-resonant pump wavelengths. A reduction in the background was observed at near-resonant wavelengths, in agreement with results reported in Ref [199]. The signal-to-noise ratio may be further improved by tuning the near-resonant wavelength to the optimum value. Additionally, Ref [199] reported a bunching effect in the maxima closest to $\tau = 0$. The data acquired here also appears to display this trend, so further data acquisition could have yielded interesting results related to this topic.

A Hong-Ou-Mandel interference experiment was designed and constructed. The apparatus was demonstrated to be suitable for the intended experiments by performing test correlation measurements using a pulsed laser as a test source, and by projecting the correlation event rates that could be a achieved with a QD source. The timing resolution of the SNSPD produced well-separated correlation maxima

which facilitated temporal alignment of the setup. The coupling efficiencies and splitting ratios through the interferometer arrangement were carefully characterised and optimised for use in a correlation experiment. Unfortunately, the QD sample was irreparably damaged while preparing for these experiments and efforts to find a suitable replacement were unsuccessful. The experimental work on this project therefore ended at this point.

Chapter 5

Development of a high resolution single-photon spectrometer for telecom wavelengths

5.1 Project motivation

The goal of this project was to improve NPL's facilities for the spectral characterisation of single photons at telecom wavelengths. As discussed in Section 1.1.3, sources at these wavelengths are of commercial interest because they experience the least loss in standard optical fibre. Section 2.3 examined relevant literature and the capabilities of existing spectrometers. A commercial instrument that meets NPL's requirements was not found, so it was undertaken to design and build a custom spectrometer system.

A scanning Fabry-Pérot interferometer (SFPI) can provide higher spectral resolution than the best grating spectrometer and camera arrangements. However, it can only produce spectra that span a relatively short range, as determined by its free spectral range (FSR). This approach was necessary to meet the resolution requirements of the project; a detailed design process took place to optimise the system for the intended measurements.

The SFPI has been designed to characterise two photonic sources that are important in quantum key distribution and quantum computing; quantum dot single-photon sources and attenuated pulsed lasers. The system was designed for a pulsed laser with a 12 GHz linewidth at a wavelength of 1550 nm. The SNSPD system described in Chapter 3 was used to provide telecom wavelength data acquisition with single-photon sensitivity.

Section 5.2 explains how the instrument works and outlines its key parameters. In Section 5.3, the parameters are considered with reference to the two types of source to produce a detailed design. The rest of this chapter reports on the successful construction and characterisation of the new instrument.

5.2 The Scanning Fabry-Pérot Interferometer

A tuneable optical cavity can be used to acquire spectral information by varying the cavity's resonant frequency and recording the transmitted intensity. This is the basis for the operation of the SFPI. Equation 5.1 gives the transmission of a perfect, lossless cavity as a function of cavity length L for a fixed input wavelength λ [15]:

$$T(L) = \frac{1}{1 + \frac{4F^2}{\pi^2}\sin^2(\frac{2\pi nL}{\lambda})} \tag{5.1}$$

where n is the refractive index inside the cavity, F is the cavity finesse (given in Equation 5.3). The form of this equation, plotted in Figure 5.1, has multiple transmission maxima separated by the cavity FSR. The unambiguous range of the system is therefore limited to its FSR; beyond that, the same wavelength can contribute to the transmission multiple times. The FSR depends only on cavity length L, according to Equation 5.2:

$$\mathrm{FSR} = \frac{c}{2L} \tag{5.2}$$

The spectral resolution of the system is determined by the cavity linewidth, $\Delta\nu_{cav}$, which is related to the FSR by the cavity finesse, F:

$$F = \frac{\text{FSR}}{\Delta\nu_{cav}} = \pi\frac{(R_1R_2)^{1/4}}{1-\sqrt{(R_1R_2)}} \tag{5.3}$$

where R_1 and R_2 are the reflectivity of the cavity mirrors. Equation 5.3 can be used to determine the mirror reflectivity required to achieve a specific linewidth, given the cavity FSR. While it is possible to produce very high finesse cavities, the ideal cavity finesse depends on the linewidth of the source. This is because the maximum count rate is limited by selecting a cavity linewidth that is significantly narrower than that of the source; this can be detrimental to the performance of the instrument when characterising weak signals. This trade-off is considered in Section 5.3.2.

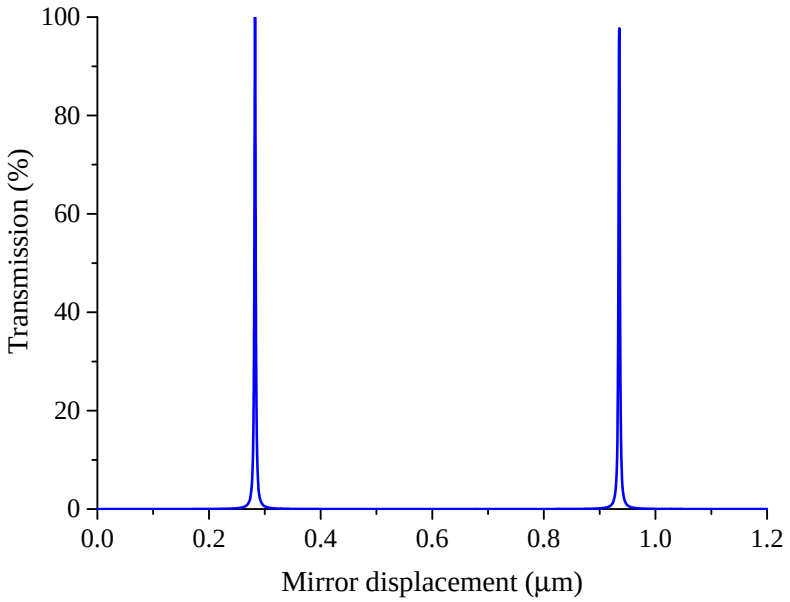

Figure 5.1: **Theoretical transmission function for a perfect, lossless cavity.** Calculated using Equation 5.1 for $\lambda = 1310$ nm, $F = 250$ and $L = 1$ mm.

5.3 Optical cavity design

To optimise the new instrument, each parameter was considered in terms of its impact on planned measurements. This produced the specifications listed below, which are discussed in the following sections.

- FSR = 150 GHz, which necessitates a cavity length $L = 1$ mm.
- Uniform resolution from 1270 nm to 1630 nm, requiring constant mirror reflectivities across this wavelength range.
- Linewidth $\Delta\nu = 600$ MHz; using Equation 5.3 with FSR = 150 GHz gives a required cavity mirror reflectivity of 98.75 % (Cavity finesse $F = 250$).
- Cavity mirrors with a radius of curvature $Rc = 20$ mm. This allows the short cavity length to be realised with bulk optics while minimising the number of transverse modes per FSR.

5.3.1 Free spectral range

The cavity FSR is the maximum spectral range that can be recorded in a single scan; as such, it must be sufficient to span the features of interest. For an attenuated laser source, the required range is several times the laser linewidth. The broadest laser we plan to characterise has a spectral linewidth of 12 GHz, which can be characterised with FSR $\sim$ 60 GHz. Typical emission linewidths from quantum dot sources are significantly narrower (see Table 5.2); they are considered in Section 5.3.2 in the context of determining the required spectral resolution of the instrument.

Quantum dots can exhibit fine structure splitting. To measure the resulting separation between the two spectral features, the FSR must incorporate the full extent of both of them. Recent measurements of fine structure splitting in quantum dots are listed in Table 5.1; they suggest that a FSR $\sim$ 70 GHz should be sufficient for such analysis.

λ(nm)	Reported separation	Range spanned by spectral features	Ref
750	22.9 GHz	70 GHz	[188]
900	14.4 GHz	37 GHz	[190]
920	29 GHz	37 GHz	[191]
910	2.5 GHz	13.5 GHz	[47]
880	3.4 GHz	30 GHz	[46]

Table 5.1: **Reported spectral range of fine structure splitting in QDs.** Both the reported separations and full ranges spanned by the features are listed.

The target FSR was set at 150 GHz to comfortably accommodate pulsed laser and quantum dot characterisation, and provide scope to meet future demands. Equation 5.2 was used to calculate that a 1 mm cavity length would be required to achieve this FSR.

5.3.2 Resolution and operating wavelengths

In order to characterise any source intended for use with optical fibre, the instrument was designed to operate at all wavelengths in the International Telecommunication Union (ITU) bands for wavelength division multiplexing, from 1270 nm to 1630 nm [200, 201]. To provide consistent resolution, the cavity linewidth must be constant across this wavelength range; once the target resolution was determined, a range of quotations for custom coatings were obtained and the design with the smallest variation in reflectivity was selected (detailed in Section 5.3.3).

The spectral resolution of the instrument must be sufficient to characterise quantum dot emission; the linewidths quoted in Table 5.2 indicate that the resolution

λ	QD linewidth			QD type	Ref.
(nm)	μeV	GHz	pm		
750	32	8	15	Aperture-selected (GaAs/AlGaAs)	[188]
914	3.7	0.9	2.5	In micropillar (InAs/GaAs)	[47]
880	10	2.4	6.3	In micropillar (InAs/GaAs)	[46]
1300	43	10.8	61	Aperture-selected (InAs/GaAs)	[165]
1185	70	16.9	79	In photonic crystal cavity (InAs/GaAs)	[202]

Table 5.2: **Reported linewidths from quantum dot exciton emission.**

should be at least $\nu_{cav} = 0.9$ GHz (3.7 μeV). To characterise the spectrum from an attenuated laser, several measurements need to be made across the laser linewidth. A reasonable resolution for a laser with a 12 GHz linewidth would be somewhere in the range from 600 MHz ($\Delta\nu_{laser}/20$) to 150 MHz ($\Delta\nu_{laser}/80$).

Reducing the cavity linewidth relative to that of the source provides higher resolution while reducing the maximum transmitted intensity. It is important to ensure that this does not preclude single-photon data acquisition. In essence, there must be sufficient signal to complete high-quality data acquisition at a much faster scan rate than any drift in the cavity's resonant frequency. A series of quantitative estimates based on this premise were made to assess the feasibility of the instrument prior to construction. These estimates are outlined below:

1. Estimation of maximum count rates for laser and quantum dot sources
2. Comparison of 1. with SNSPD dark count rate (to estimate signal-to-noise)
3. Estimation of scan duration for preliminary and high-quality spectra
4. Estimation of cavity resonant frequency drift rate
5. Comparison of scan rates and drift rate (scan must be faster than drift)

If a pulsed laser is attenuated to the level of one photon per pulse ($\mu = 1$), the photon emission rate equals the repetition rate of the laser, P_{rep}. The resulting count rate, S_{laser}, can be estimated by accounting for the efficiency of transmission through the cavity (η_{cav}), the coupling efficiency into the output fibre ($\eta_{coupling}$), the detection efficiency (η_{SNSPD}), and differences in laser and cavity linewidth ($\Delta\nu$):

$$S_{laser} = P_{rep} \times \eta_{cav} \times \frac{\Delta\nu_{cav}}{\Delta\nu_{laser}} \times \eta_{coupling} \times \eta_{SNSPD} \tag{5.4}$$

Equation 5.4 was used to estimate count rates for laser repetition rates of 80 MHz and 1 GHz, with $\Delta\nu_{laser} = 12$ GHz. A conservative value of $\eta_{SNSPD} = 1$ % was used to represent the SNSPD system detection efficiency at $\lambda = 1550$ nm (see Chapter 3), and the estimated cavity transmission efficiency ($\eta_{cav} = 0.874$) was based on

the optical design described in Section 5.3.3. It was assumed that 70 % coupling into the output fibre would be achievable. The resulting count rate estimates in Table 5.3 all exceed the standard SNSPD dark count rate of 1 kcps by at least a factor of 6, indicating that the targeted resolution values are all suitable for these measurements. In practice, the maximum detectable count rate will be limited by detector dead time to 100 Mcps, and by data acquisition electronics to $\sim$ 10 Mcps. However, the projected maximum count rates in Table 5.3 are considerably lower than this.

	Projected maximum count rate (kcps)	
$\Delta\nu_{cav}$	(P_{rep} = 80 MHz)	(P_{rep} = 1 GHz)
150 MHz	6.1	76.5
600 MHz	24.5	305.9

Table 5.3: **Estimated SFPI count rates for an attenuated laser source.** Projected maximum count rates through the cavity on resonance for a pulsed laser at $\lambda = 1550$ nm. The values for $P_{rep} = 1$ GHz have been scaled to account for the maximum SNSPD count rate of 100 Mcps.

For quantum dot single-photon sources, count rate estimates were based on the sample investigated in Chapter 4. This is reasonable because the photon emission rate is ultimately limited by the lifetime of the radiative transition, and the lifetimes of the QDs investigated are comparable to values reported at telecom wavelengths [165, 166]. These calculations were intended to indicate the feasibility of future experiments; the actual count rates from a QD will depend on the intensity of the pump laser, the collection efficiency and the strength of QD-cavity coupling. Equation 5.5 starts with previously measured count rates from QDs, S_{prev}, and accounts for cavity transmission efficiency, detection efficiency and differences in spectral bandwidth:

$$S_{QD} = S_{prev} \times \eta_{cav} \times \frac{\Delta\nu_{cav}}{\Delta\nu_{prev}} \times \eta_{coupling} \times \frac{\eta_{SNSPD}}{\eta_{SPAD}} \tag{5.5}$$

The count rate estimates in Table 5.4 are based on three quantum dots that were measured with a SPAD ($\eta_{SPAD} = 30$ % at $\lambda = 900$ nm). They are scaled down for $\eta_{SNSPD} = 10$ % based on detector performance at $\lambda = 1310$ nm as this wavelength is

typical of telecom wavelength quantum dots. These count rates are much lower than those for the laser source; it was necessary to select $\Delta\nu_{cav} = 600$ MHz to maximise the count rate within the resolution values under consideration. The SNSPD dark count rate could be reduced at the cost of lower (but not proportionally lower) efficiency, as was discussed in Chapter 3. However, this increases the scan duration, so is only possible if the scan rate remains significantly faster than the drift rate.

The drift in the cavity's resonant frequency was estimated based on a similarly stabilised, 100 mm-long cavity [203]. The system has a 1.5 GHz FSR and 15 MHz resolution, and has a maximum drift rate of 500 kHz/hr. The same level of stability for a cavity which is 1 mm long would result in a drift rate of 50 MHz/hr.

Count rate	$\Delta\nu_{cav}$	QD1 (kcts/s)	QD2 (kcts/s)	QD3 (kcts/s)
S_{prev}		525	112	68
S_{proj}	150 MHz	0.86	0.18	0.11
S_{proj}	600 MHz	3.44	0.73	0.45

Table 5.4: **Estimated SFPI count rates for a QD single-photon source.** Count rates from three quantum dots are adjusted using Equation 5.5 to produce count rate estimates at two cavity resolution values $\Delta\nu_{cav}$.

Scan durations were estimated by considering the number of frequency steps in a scan, the maximum count rate and the desired number of counts to be recorded at the point of maximum intensity, n:

$$\text{Scan duration} = \#\text{ frequency steps} \times \left(\frac{n}{\text{max. count rate}} + 1\text{ sec}\right) \tag{5.6}$$

At each step, an additional second is added to allow for actuator settling and data processing. For a preliminary fast scan, 500 counts at the point of highest intensity ($n = 500$) should allow features of interest to be located; this has an associated statistical uncertainty $\sqrt{n}/n = 4.5$ %. To scan across the 150 GHz FSR in frequency intervals equal to the cavity resolution (600 MHz) requires 250 steps. For high quality data, $n = 10000$ reduces the statistical uncertainty to 1 % in the frequency interval containing the highest signal. Scan durations were calculated for 80 frequency steps, which is reasonable because the region of interest is likely to be smaller than the full FSR. The scan duration estimates for a range of projected count rates are given in Table 5.5.

Experiment	Count rate (kcts/s)	Fast scan (250 ch) duration	Fast scan (250 ch) $\frac{\text{scan rate}}{\text{drift rate}}$	High-quality scan (80 ch) duration	High-quality scan (80 ch) $\frac{\text{scan rate}}{\text{drift rate}}$
QD (low rate)	0.45	8.8 min	2046	31 min	186
QD (high rate)	3.44	4.8 min	3772	5.2 min	1106
80 MHz laser	24.5	4.3 min	4234	1.9 min	3068
1 GHz laser	305.9	4.2 min	4313	1.4 min	4183

Table 5.5: **Estimated scan durations for laser and QD sources, and a comparison of estimated scan and drift rates.** The data acquisition scan rate is compared with the estimated drift rate of the cavity for four different experimental scenarios.

Scan rates were obtained by dividing the spectral range of each scan by the corresponding scan duration estimate. Comparison with the estimated cavity drift rate (see Table 5.5) shows that the slowest scan rate is 186 times faster than the anticipated drift rate. This demonstrates that at 600 MHz resolution, the SFPI system should be stable enough to characterise quantum dot sources at the single-photon level.

5.3.3 Mirror geometry and transverse modes

A number of mirror geometries were considered for the design of the 1 mm cavity. A planar cavity (Figure 5.2 a) is generally impractical because it becomes unstable if the incoming light is slightly off-axis or the mirrors are not perfectly parallel. In theory, a confocal resonator (Figure 5.2 b) is ideal because it is robust to misalignment. Additionally, the need for careful mode matching is eliminated by the degeneracy between transverse and longitudinal modes. However, for $L = 1$ mm this would require very small mirrors with a 1 mm radius of curvature (Rc), which cannot be produced with standard mirror fabrication techniques.

One solution is to use a non-confocal cavity (Figures 5.2 c-e). The short cavity length can be achieved with both a larger mirror diameter (D) and radius of curvature (R) than the confocal design, while retaining its robustness to misalignment. The drawback is that mode matching is essential due to the presence of non-degenerate transverse modes. Keeping the number of these modes to a minimum was a key consideration to facilitate coupling all of the light into the lowest-order transverse mode (TEM_{00}). It was found that a symmetric cavity has fewer additional modes

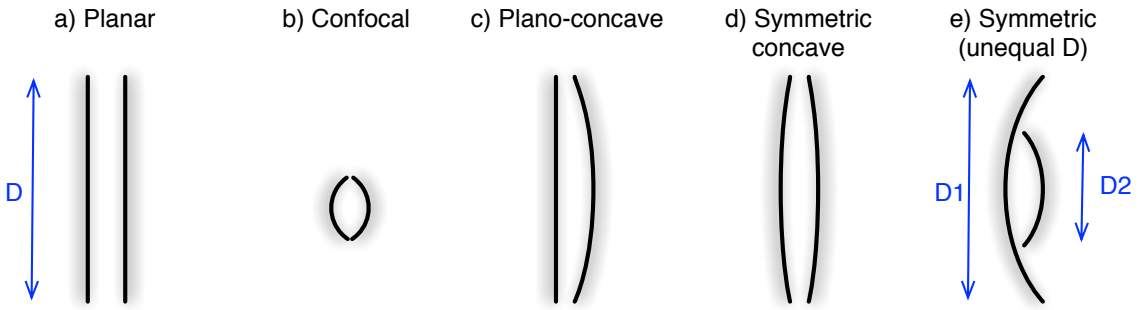

Figure 5.2: **Consideration of cavity mirror geometries.** Planar, confocal, plano-concave and symmetric cavities are illustrated, all with the same mirror separation. The diameter of the optics, D, is limited by the combination of curvature and fixed mirror separation in all cases except the planar arrangement. Diagram e) shows that smaller radius of curvature can be used without causing the mirrors to touch when one mirror has a smaller diameter than the other (D2 < D1).

than a plano-concave cavity of the same length (14 compared to 20 modes when $Rc = 50$ mm), and that a smaller radius of curvature results in fewer additional transverse modes. A small radius of curvature also improves the stability criterion for a Gaussian resonator [$g_1 g_2 = (1 - \frac{L}{Rc_1})(1 - \frac{L}{Rc_2})$], moving it away from the edge of stability $g_1 g_2 = 1$. For a given cavity length, a smaller radius of curvature can be used if one of the mirror diameters is reduced. This is illustrated in Figures 5.2 d and 5.2 e. Table 5.6 gives mirror diameters (D1, D2) that allow a range of Rc values to be achieved, down to the smallest value that could be manufactured. $Rc =$ 20 mm was selected in order to minimise the additional transverse modes per FSR.

Rc (mm)	D1 (mm)	D2 (mm)	Modes per FSR	Beam waist in cavity (μm)	Stability $g_1 g_2$
50	18	8.5	14	44.8	0.96
40	17	4	13	42.4	0.95
30	15	4	11	39.4	0.93
20	12	4	8	35.5	0.90

Table 5.6: **Diameters of cavity optics for symmetric cavities with different mirror curvatures** Rc**.** Practical mirror diameters (D1, D2) for a 1 mm cavity are listed with the number of additional transverse modes per FSR and the stability criterion.

The design of the cavity mirrors is shown in Figure 5.3. A combination of diameter and curvature was selected such that a 1 mm cavity is formed when the edges of the two mirrors are in the same plane. The chamfer on the smaller mirror allows this

to be achieved without the two optics coming into contact with each other. Figure 5.4 shows how the cavity is constructed; the re-entrant mirror is mounted on a ring of actuators on a back plate, while a spacer piece and another ring of actuators are attached to the external mirror. The two halves fit together to produce a 1 mm cavity as shown in Figure 5.5.

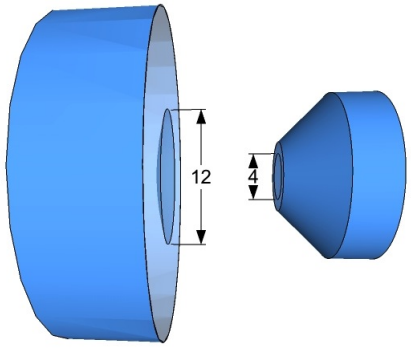

Figure 5.3: **Cavity optics (1).** The external and internal mirrors have spherically-curved mirror surfaces (Rc = 20 mm) with 12 mm and 4 mm diameters respectively.

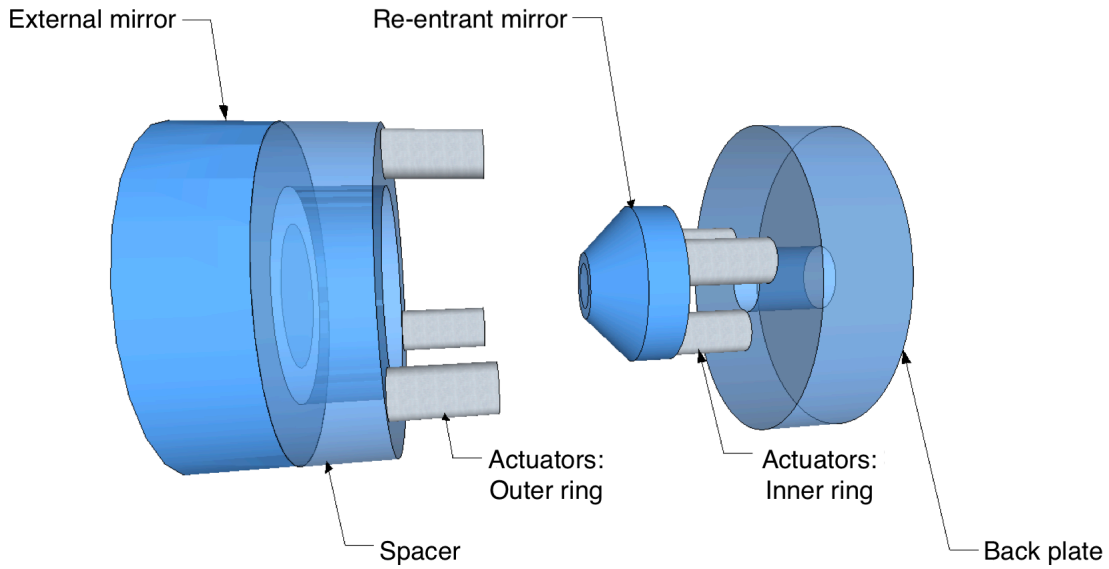

Figure 5.4: **Cavity optics (2).** The external mirror is optically contacted to a spacer piece. The outer ring of actuators is attached to a cylindrical spacer, which stabilises the cavity mirror separation. The re-entrant mirror is mounted on the inner ring of actuators, which are attached to a back plate.

The glass components were custom made by IC Optical Systems Ltd. The spacer and re-entrant mirror were manufactured simultaneously to ensure they were of equal thickness, in order to position the edges of the mirrors in the same plane.

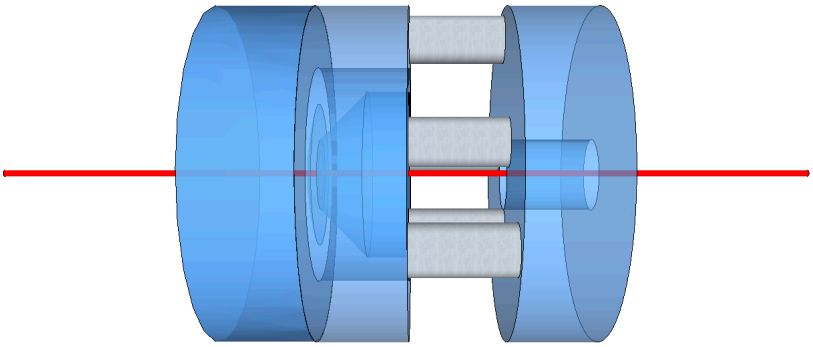

Figure 5.5: **Cavity optics (3).** The re-entrant mirror is inserted inside the spacer and the outer ring of actuators is epoxied to the back plate. This arrangment forms a 1 mm cavity between the external and re-entrant mirrors.

With this condition met, the manufacturing tolerance on the length of the cavity was $\pm$ 0.15 mm. The cavity length could also be affected by differences between the inner and outer ring of actuators or epoxy thicknesses. A shorter cavity length is a benefit as this extends the FSR. The cavity would need to be 1 mm longer than planned to reach the minimum FSR of 70 GHz defined in Section 5.3.1. It was concluded that this is unlikely with 8 mm-long actuators and sub-mm layers of epoxy, so the design should comfortably produce a cavity with a useful FSR.

The dielectric cavity mirrors were coated to have a reflectivity $R = (98.75 \pm 0.25)$ % to achieve the 600 MHz design resolution, and the back surfaces were anti-reflection coated ($R < 0.1$ %) to minimise loss. The uncertainty in reflectivity translates to $\pm$ 120 MHz in resolution; this was the best possible specification that could be achieved across such a wide range of wavelengths. The coatings were designed and produced by LaserOptik GmbH. The cavity is housed in a vacuum chamber to increase its stability (see Section 5.4), so light passing through the cavity also travels through two optical flats that form the vacuum chamber windows. The maximum transmission through the cavity assembly in the vacuum chamber was calculated by combining the losses at each interface and using Equation 5.7 [204] to calculate the circulating intensity inside the cavity:

$$\frac{I_{circulating}}{I_{incident}} = \frac{T}{[1 - Re^{-2\alpha_o L}]^2} \tag{5.7}$$

where R is the reflectivity of both cavity mirrors, the transmission $T = 1 - R$, and $2\alpha_o L$ is the round trip loss, which is 0.06 % (due to the absorption in the mirror coatings). The calculation, detailed in Table 5.7, produces a maximum transmission of 87.4 %.

Stage	%(input)
1) Loss entering vacuum chamber ($R = 0.4$ % per window surface)	99.2
2) Loss at AR coating entering cavity ($R = 0.1$ %)	99.1
3) Build-up inside cavity (x 72.9) $\times$ cavity transmission (1.22 %)	88.2
4) Loss at AR coating exiting cavity ($R = 0.1$ %)	88.1
5) Loss exiting vacuum chamber ($R = 0.4$ % per window surface)	87.4

Table 5.7: **Estimated transmission through SFPI on resonance.** Calculations include loss at the vacuum chamber windows.

5.4 Cavity stability and tuning

The resonant frequency of the cavity depends only on its length, so $\Delta L/L = \Delta\nu/\nu$. While stabilisation is relatively straightforward for a fixed-length cavity where the mirrors can be positioned permanently, it is a greater challenge to build a system that can tune the cavity length and maintain stability at each position. The stabilisation and tuning elements of the design are described in the following sections.

5.4.1 Path length stabilisation

Temperature is a major cause of path length instability. Its impact can be reduced in three ways; stabilising the temperature, optimising the cavity design and increasing the thermal time constant of the system to slow down any remaining variation. A two-layer temperature control system with servo feedback based on thermistors was used to stabilise the cavity temperature. The outer layer provides a buffer to external fluctuations, allowing the inner layer to achieve a higher level of stability. The configuration and testing of this system is detailed in Section 5.5.

Two aspects of the design reduce the impact of temperature on cavity length. The first is the use of two rings of actuators (shown in Figure 5.4). While only the inner ring of actuators is used to change the cavity length, any thermal expansion that is also experienced by the outer ring of actuators moves the back plate instead of the cavity mirror. Secondly, all glass components were made of Zerodur which has a very low coefficient of thermal expansion (CTE). The benefit can be demonstrated by comparing the effect of a 100 mK temperature change on fused silica (CTE = $52 \times 10^{-8}\ K^{-1}$ [205]) and Zerodur (CTE = $(0 \pm 2) \times 10^{-8}\ K^{-1}$ [206]). For a specific frequency ν and temperature change ΔT, the change in frequency is:

$$\Delta\nu = \nu \times \mathrm{CTE} \times \Delta T. \tag{5.8}$$

In the operating wavelength range from 1270 nm to 1630 nm, the change in resonant frequency ($\Delta\nu$) induced by $\Delta T = 100$ mK ranges from 370 kHz to 470 kHz for Zerodur, while for fused silica it ranges from 9.6 MHz to 12.2 MHz. A potential source of drift was thus eliminated with the choice of Zerodur for all glass components.

The thermal time constant of the system was increased by mounting the cavity optics in a PTFE cage inside a steel vacuum chamber. The vacuum assembly is shown in Figure 5.6; viewport flanges at each end of the chamber provide a clear optic axis, and there are ports for a vacuum pump, angle valve and electrical feedthrough. An ion pump was chosen for its vibration-free operation. The vacuum chamber was customised so the window flanges were positioned 2 degrees off-normal relative to the optic axis. This reduces the risk of parasitic etalon formation without introducing appreciable astigmatism.

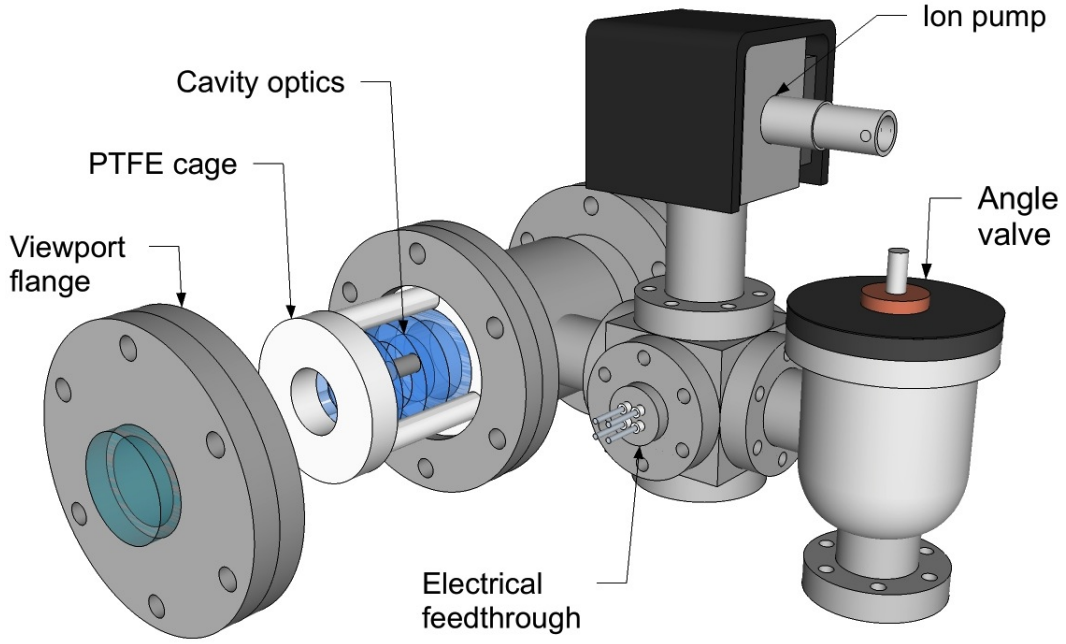

Figure 5.6: **Vacuum system for housing cavity optics.** The cavity optics are mounted in a vacuum chamber inside a PTFE cage. The chamber is initially evacuated via the angle valve, then the vacuum is maintained with the ion pump. An electrical feedthrough provides voltage to the actuators, and viewport flanges along the optic axis allow light to be coupled to the cavity inside.

An additional benefit of housing the cavity optics in a vacuum chamber is the elimination of variations in optical path length due to pressure-induced refractive index fluctuations. To show this, the dependence of refractive index on pressure was calculated for a range of pressures according to [207] with dry air, T = 20 ^{o}C and $\lambda = 1310$ nm. A linear fit yielded the relation

$$\frac{dn}{dP} = 3 \times 10^{-9} \text{ Pa}^{-1}, \tag{5.9}$$

which means that the fractional variation in refractive index is

$$\frac{\Delta n}{n} = \frac{3 \times 10^{-9} \Delta P}{n}. \tag{5.10}$$

If the maximum temperature fluctuation is 100 mK about a central value of 293 K, and the cavity is housed in a chamber that is evacuated to 10^{-5} mbar (=10^{-3} Pa), this produces a change in pressure of

$$\Delta P = P_f - P_i = \frac{P_i T_f}{T_i} - P_i \approx 3.4 \times 10^{-7} \text{ Pa}. \tag{5.11}$$

From Equation 5.10, this results in a fractional variation in refractive index (and therefore in path length) on the order of 10^{-15}, which is equivalent to a frequency variation of 0.2 Hz about a central wavelength of 1310 nm. This is therefore negligible in path length stability considerations.

5.4.2 Tuning the cavity length

The cavity length is varied by changing the voltage on the inner ring of actuators, which moves the re-entrant mirror. In order to produce spectra that utilise the cavity's range and resolution, the minimum requirement is the ability to move the mirror across at least one FSR in steps corresponding to the cavity linewidth. The selected actuators extend by 3.2 μm over 100 V, which spans > 4 FSRs across the operating wavelength range.

To change the resonance by a specific amount ($\Delta\lambda$) within one FSR requires a mirror movement (ΔL) given by:

$$\Delta L = \frac{\mathrm{n}\Delta\lambda}{2}, \tag{5.12}$$

where n is the longitudinal mode number (i.e. $\mathrm{n} = \frac{2L}{\lambda}$) and $\Delta\lambda = \frac{\lambda^2 \times \mathrm{FSR}}{c}$. To change the resonant frequency in 600 MHz increments requires steps from 2.5 nm to 3.3 nm across the operating wavelength range. Assuming that the actuators have a roughly linear response, these steps require a voltage increment ~ 80 mV. The ideal voltage source would therefore provide stable increments of < 10 mV over at least 25 V, in order to characterise the resolution of the instrument in addition to making resolution-limited spectral measurements across the full FSR.

5.5 System construction and characterisation

5.5.1 Construction details

The cavity optics were carefully assembled to minimise deviation from the planned cavity length. The spacer piece and external mirror were optically contacted to remove the length uncertainty due to epoxy at one interface. The actuators, back plate and re-entrant mirror were assembled (as shown in Figure 5.4) using thin layers of vacuum epoxy in a purpose-built alignment jig that held the elements concentrically. The vacuum system was assembled and baked without the cavity mounted inside. It held vacuum at $< 1 \times 10^{-8}$ mbar with a leak rate $< 1 \times 10^{-9}$ mbar l/s. With its integrity confirmed, the cavity optics were mounted in a PTFE cage and inserted as shown in Figure 5.6. The same vacuum level was achieved when the system was evacuated and baked out again, indicating that any outgassing from the cavity is slow compared to the speed of the ion pump.

For each of the two separate layers of temperature control, a bridge circuit containing a thermistor (Figure 5.7) was set up to produce a temperature-dependent error signal. This was fed into the proportional-integral (PI) servo circuit shown in Figure 5.7. The inner layer was the vacuum chamber, which was wrapped in heater wire

then insulating foam. The outer layer was a separate enclosure formed from a box lined with foam and thin sheet copper mounted with heater mats. Initially, the two layers were set up and optimised individually. When they were operated together, the gain of the inner layer was reduced due to the stabilisation of the outer housing. The final optimised configuration stabilised the temperature to ± 1 mK and ± 5 mK for the chamber and housing respectively. Figure 5.8 shows the variation over 24 hours. While the housing temperature was visibly disturbed by the presence of people in the lab during the day, the chamber temperature remained stable.

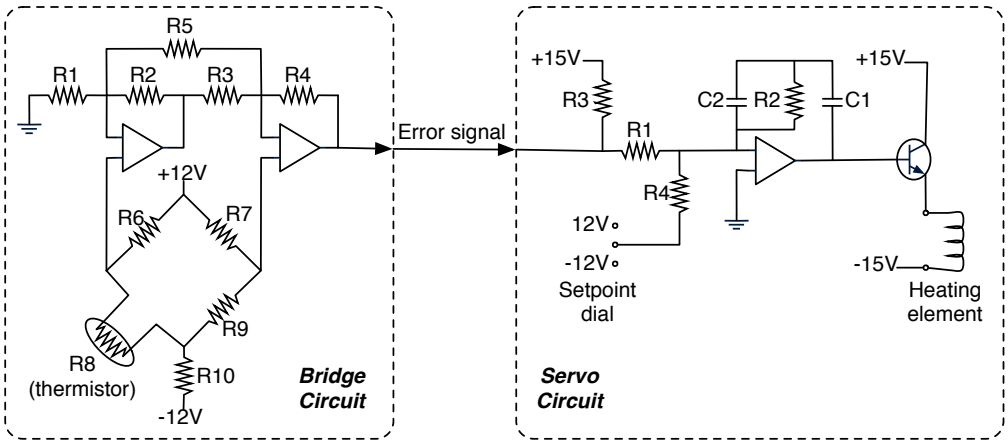

Figure 5.7: **Temperature controller circuits.** The bridge circuit makes a stable measurement of the voltage across the bridge and applies a gain of 211. The proportional-integral servo circuit supplies current to a heater element such that the temperature settles at the set point value. The feedback loop elements (C1, C2, R1, R2) were optimised separately for the temperature control of the vacuum chamber and the outer housing.

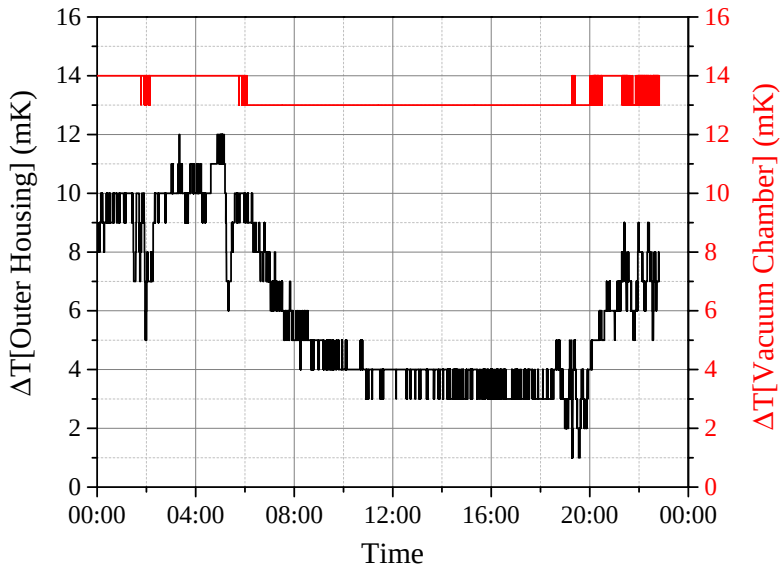

Figure 5.8: **Temperature stabilisation data**. ΔT[vacuum chamber] remains stable to ± 1 mK while ΔT[outer housing] varies across 10 mK in a 24 hour period.

5.5.2 Beam delivery and cavity transmission

Figure 5.9 shows the experimental arrangement of the SFPI system. Light from a fibre-coupled source is collimated with one lens then focused into the cavity with a second lens. The transmission is similarly collected into another fibre and delivered to the SNSPD. This arrangement makes it straightforward to characterise a range of different sources. Selecting the collimating and focusing lenses with a simple ratio of beam waists does not account for the thickness or curvature of the cavity mirror. ABCD matrices were used to propagate a Gaussian beam from the delivery fibre to the cavity waist. It was found that the position of the beam waist moves ~ 2.2 mm further away from the fibre due to passing through the cavity mirror, which is significant in a 1 mm cavity. Lenses were selected based on the calculations, positioning the beam waist at the centre of the cavity with the correct magnification.

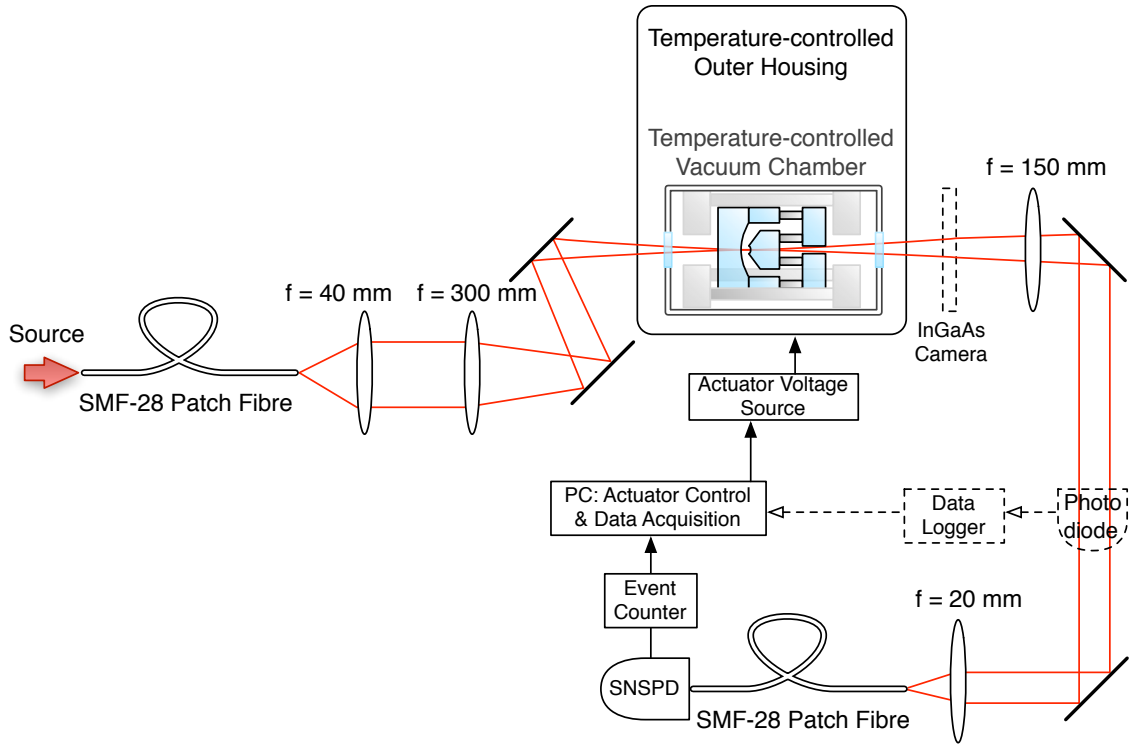

Figure 5.9: **Experimental arrangement for SFPI measurements.** Light is delivered and collected with FC/PC SMF-28 patch fibres. The beam is coupled to the cavity using free space optics, and the transmission is collected into another fibre to facilitate delivery to the SNSPD or other detector.

The TEM_{00} mode was located by observing the cavity transmission at the exit of the outer housing with an InGaAs camera The photodiode signal was then monitored as the cavity mirror was scanned across 2 FSRs. A repeating pattern of transmission features was observed, indicating coupling to different transverse modes; this signal was used as a guide to optimise coupling into the TEM_{00} mode. The maximum transmission on resonance was 74 %, measured at the entrance and exit of the outer housing, which is lower than the projection of 87.4 % from Section 5.3.3. The light exiting the cavity was coupled into the output fibre with 65 % efficiency. It should be possible to improve this to 80 %, given the clean spatial mode exiting the cavity. The percentage of the transmitted light that was coupled into the TEM_{00} mode was estimated by comparing signal amplitudes to be 89 %. Improvements in the mode matching may be achieved by fine tuning the input beam parameters, while improvements in transmission measurements may be observed by increasing the cavity stability.

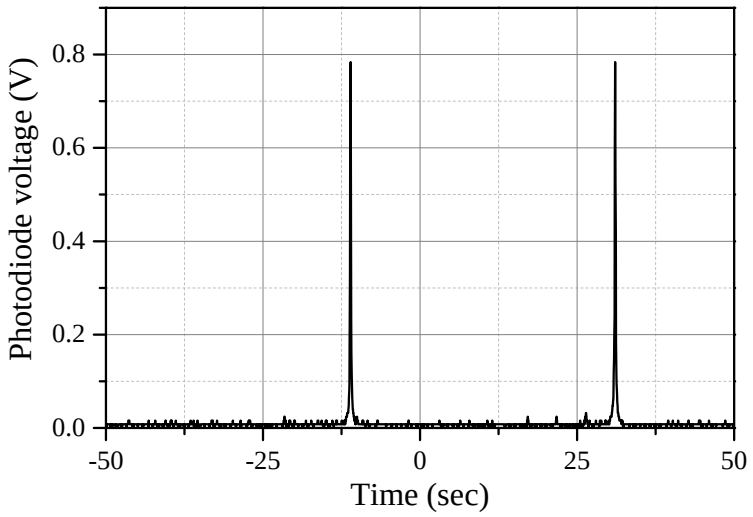

Figure 5.10: **Optimised coupling to TEM_{00} cavity mode.** This plot shows the photodiode signal measured at the position indicated in Figure 5.9 while the actuator voltage was linearly scanned. The observed transmission profile matches well with the theory shown in Figure 5.1.

Figure 5.10 shows the optimised transmission through the cavity as the actuators were scanned. The observation of one clear maximum per FSR with minimal signal in between indicates that the light is mainly coupled into the TEM_{00} cavity mode. This measurement was made at the exit of the cavity before the light was coupled

into the output fibre. While coupling into this fibre incurs some signal loss, it also improves the quality of the transmitted signal because the TEM_{00} has the best spatial overlap with the end of the fibre and therefore couples in more efficiently than higher-order transverse modes. This is illustrated in Figure 5.11, which shows measurements of cavity transmission at the cavity exit and at the fibre exit for a signal containing some higher-order elements in order to display the improvement.

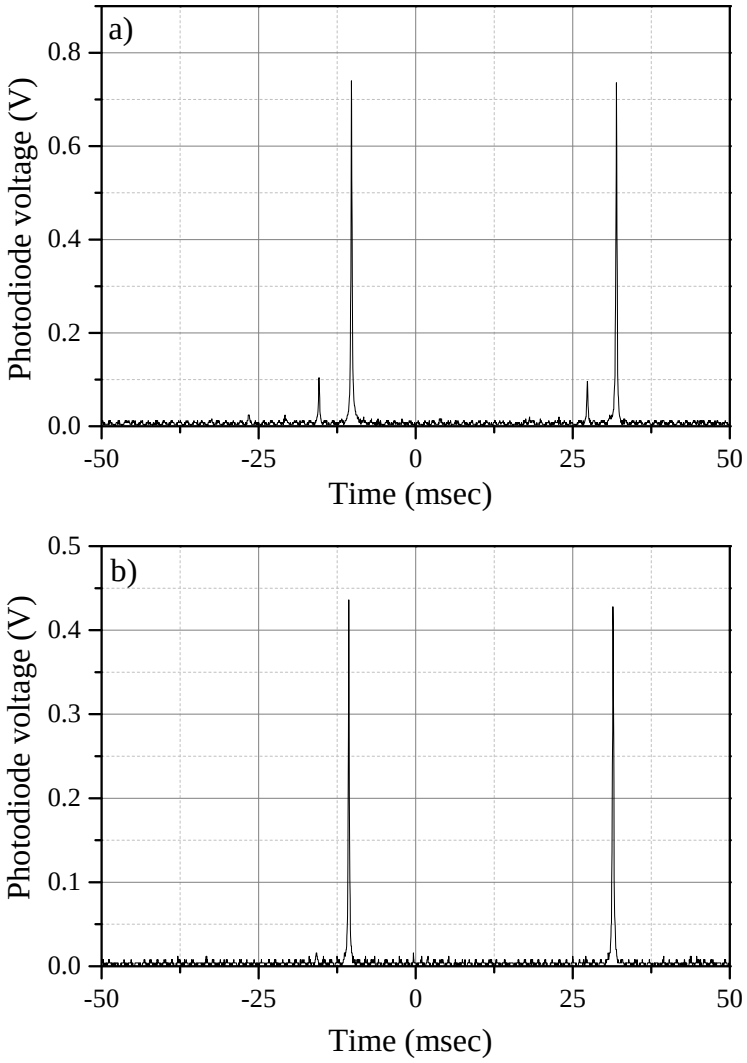

Figure 5.11: **Demonstration of spatial filtering due to output fibre.** a) Transmitted intensity at the cavity exit with sub-optimal alignment to demonstrate that coupling into a higher-order transverse mode produces an additional spectral feature; b) The same transmitted signal after passing through the output fibre; spatial filtering increases the proportion of the signal that originates from the TEM_{00} mode.

5.5.3 Stability and drift

The stability of the cavity was investigated by applying a constant voltage to the actuators and monitoring the transmitted intensity as a function of time. The actuators were positioned such that the cavity transmitted half the maximum intensity, to allow both the magnitude and direction of variation to be observed. Due to unexpectedly high noise in the output from the voltage source intended for cavity length control, which had a range of 100 V, a more stable voltage supply with a 20 V range was used in the initial characterisation. The transmitted intensity was significantly disturbed by mechanical vibration; this was observed when gently tapping on the bench near the cavity. To reduce this disturbance, the system was mounted on a passive isolation stage that provided 40 dB of attenuation at frequencies up to 100 Hz. This improved the stability of the signal, but gentle tapping and acoustic vibration still affected the transmitted intensity. The stability of the cavity is therefore likely to be improved by additional isolation.

Figure 5.12 shows the drift in the cavity resonance over time at three levels of incident power. Initial measurements with 10 mW incident on the cavity showed a clear, rapid drift; the incident power was then systematically reduced to determine

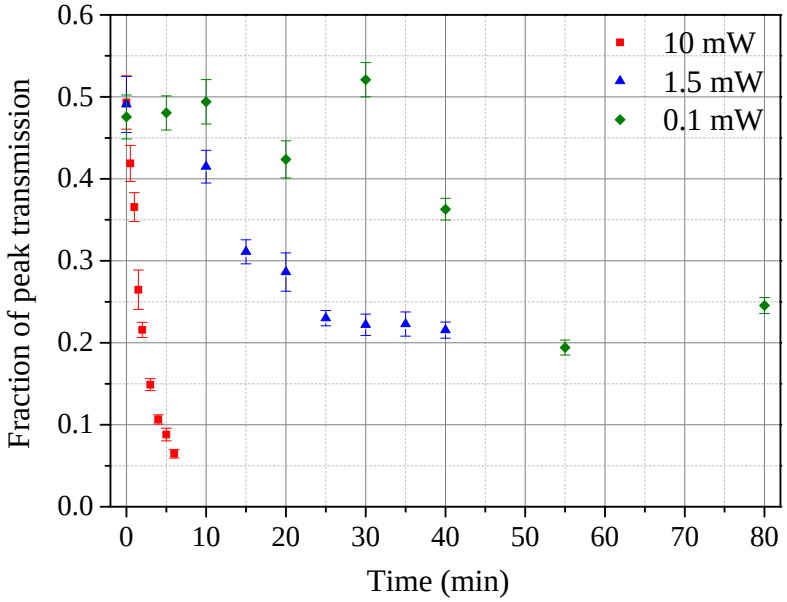

Figure 5.12: **Drift in cavity transmission over time.** From a starting position at half the maximum transmitted intensity, the transmission was observed to drop over time at a rate that appears to be connected to the laser power coupled into the cavity.

a suitable level for characterisation measurements. The drift direction indicated that the resonant frequency was increasing, which means that the cavity length was decreasing. At an incident power of 0.1 mW, the signal no longer exhibited a clear drift in one direction, indicating that the power circulating in the cavity was no longer the main cause of variation within the first 30 minutes, which is the longest estimated scan duration in Table 5.5.

The change in drift rate with incident power suggests that it is due to a heating effect. A reduction in cavity length could be caused by expansion of the dielectric coatings, or of the re-entrant mirror; expansion of the spacer would increase the cavity length. With 10 mW coupled into the cavity, the circulating power is 729 mW, of which 73 μW (0.01 %) is absorbed by the coating [208]. Typical dielectric mirror coatings such as Al_2O_3 and Ta_2O_5 have thermal expansion coefficients of 5.4×10^{-6} K^{-1} and 3.1×10^{-8} K^{-1} respectively [209]. The Zerodur mirror substrate has a much lower coefficient of thermal expansion ($(0 \pm 2) \times 10^{-8}$ K^{-1} [206]) and is only exposed to the transmitted power, which is considerably smaller than circulating power; it is therefore more likely that the drift originates in the coatings.

It was determined by scanning the mirror over the cavity resonance that a change in optical path length of $\sim$ 3 nm would be required to produce the observed drop in transmission from 50 % to 10 % of the maximum intensity. While the power absorbed in the coating can be estimated, the impact on a multilayer dielectric stack is not straightforward. The change in temperature caused by the absorbed radiation depends on the heat capacity of the coating materials and the thermal conductivity to the wider structure. This temperature change then affects both the physical thickness and refractive index of the dielectric layers. For example, the dependence of refractive index on temperature for Al_2O_3 is $\sim 10^{-5}$ K^{-1} [210], an order of magnitude larger than the coefficient of thermal expansion. This suggests that refractive index plays a larger role than expansion in thermally-induced cavity changes. In addition to affecting the optical path length, variation in refractive index can change the contrast between successive layers which affects their reflectivity and could change the overall depth that the light penetrates into the stack. The high peak intensity that is absorbed by the coating at the centre of the beam spot

(~ 4 Wcm^{-2}) also raises the possibility of transverse variation in refractive index causing thermal lensing, which could affect the efficiency of coupling to the TEM_{00} mode. Modelling this system is a complex task that is compounded by the lack of information regarding the coating design and materials; this would necessitate making assumptions about key parameters. As this system is intended for measurements at low photon flux, measurements proceeded using an incident power below 0.1 mW to give a more representative indication of cavity performance while providing a large enough signal for alignment and characterisation measurements.

5.5.4 Free spectral range and actuator linearisation

The FSR was measured using a Tunics tuneable CW laser (linewidth ~ 150 kHz, tuning range: 1270 nm to 1350 nm). The actuators were grounded while the frequency of the laser was tuned across four successive transmission maxima at wavelengths around 1310 nm. The laser frequency at which each maximum occurred was recorded three times using a Burleigh WA-1500 wavemeter, approaching the maximum from the same side each time. The fractional uncertainty in the wavemeter measurements ($\pm 2 \times 10^{-6}$) was propagated through to a calculation of the frequency spacing of the maxima. The resulting FSR is (119.0 $\pm$ 0.4) GHz, which corresponds to a cavity length of (1.260 $\pm$ 0.004) mm. This is 26 % longer than the 1 mm design specification, which falls outside of the manufacturing tolerances. One possible explanation is that the vacuum epoxy used to assemble the cavity had an unexpectedly large effect on cavity length. The maximum length within manufacturing tolerances is 1.15 mm, so if the glue layer on the outer ring of actuators was 0.11 mm thicker than that on the inner ring, that would account for the difference.

The nonlinear response of the actuators was characterised by scanning the actuator voltage while the laser wavelength was fixed and recording the voltages at which transmission maxima were observed. These features are separated by one FSR; data at different wavelengths were related using accurate wavelength measurements. Seven series of transmission maxima at wavelengths around 1310 nm are shown in Figure 5.13. A fifth-order polynomial provided the best fit to the low-voltage data points. This function was used to convert voltage to mirror displacement.

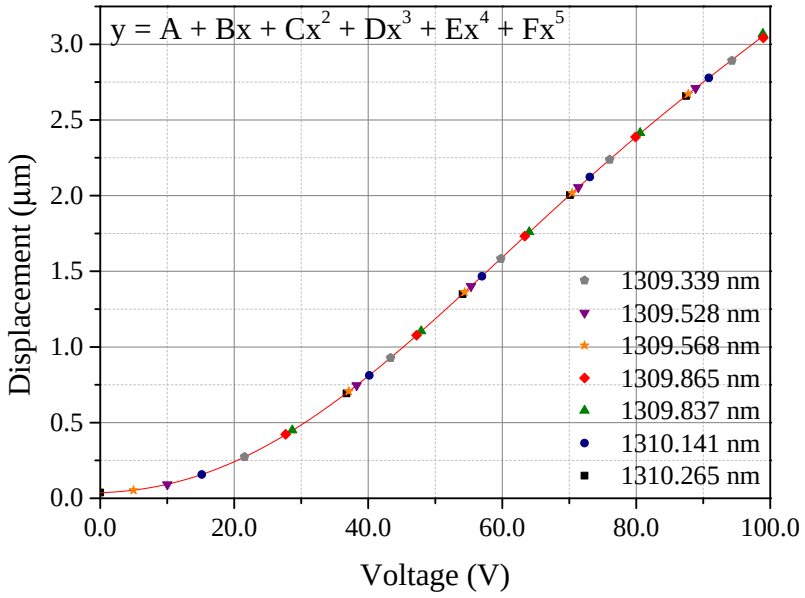

Figure 5.13: **Actuator linearisation data.** A fifth-order polynomial fit provided the best match to the low-voltage data points. The coefficients are: A = (3.7 ± 0.4)×10^{-8}, B = (1.4 ± 0.8)×10^{-9}, C = (3.7 ± 0.5)×10^{-10}, D = (5 ± 1)×10^{-12}, E = (-1.1 ± 0.1)×10^{-13}, F = (4.4 ± 0.5)×10^{-16}.

5.5.5 Hysteresis

The impact of drift and hysteresis on the cavity transmission can be assessed by scanning the actuator voltage up, down and up again across the same resonance. If drift is the dominant source of variation, the three scans will move successively in one direction; if hysteresis dominates, the second scan will differ in position significantly, while the first and third will be more comparable.

Figure 5.14 shows the transmitted intensity as the actuator voltage was continuously scanned over the resonance three times. Each pass across the resonance took ~ 3.5 min. The data show clear hysteresis, with minimal drift over the 10 minute measurement period indicated by the close similarity between the two scans in the same direction. Further investigation would be necessary in order to conclusively determine the extent of the hysteresis that occurs when the actuators are scanned in both directions. In the short term, hysteresis was avoided by performing all scans in the direction of increasing voltage.

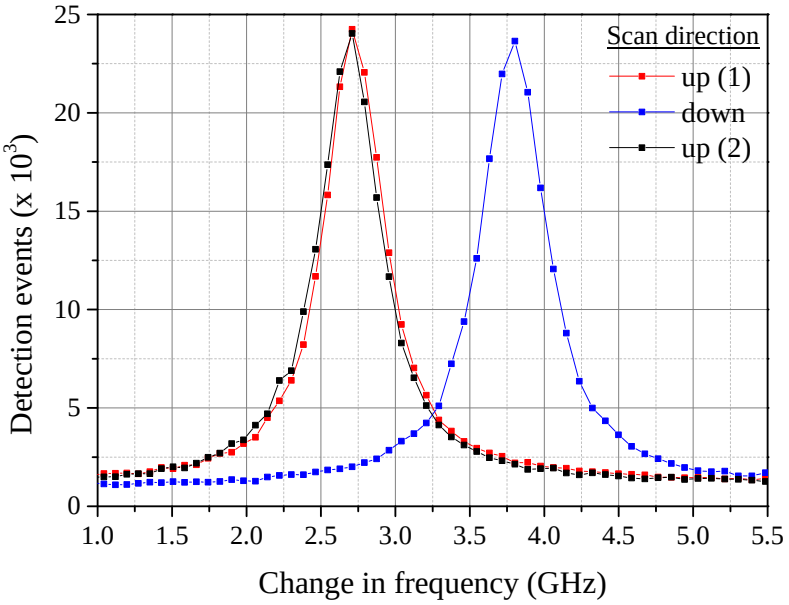

Figure 5.14: **SFPI scans testing for drift and hysteresis.** The actuator voltage was increased, decreased then increased again across the same cavity resonance to produce the three maxima in this plot. The similarity between the 'up' scans (with increasing voltage) indicates that the drift was negligible over the scan duration, while the different position of the 'down' scan (decreasing voltage) indicates significant hysteresis.

5.6 SFPI resolution at the single-photon level

To test the performance of the new SFPI, a RIO Orion CW single frequency external cavity laser ($\lambda = 1543$ nm) was set up in series with a HP 8158B variable optical attenuator (range: up to 60 dB) to produce the projected count rates given in Table 5.5. The laser was selected to have a linewidth narrower than that of the cavity to ensure that the transmission was limited by the cavity resolution. The transmitted intensity was measured using the SNSPD as the cavity's resonant frequency was scanned over the laser frequency.

Fast and high-quality scans as defined in Section 5.3.2 were carried out at a range of count rates, with the actuators stepped linearly in voltage then converted to frequency based on the fit in Figure 5.13. The instrument resolution was obtained by fitting Equation 5.13 to the data; this is a modified version of Equation 5.1 incorporating a scale factor (A), a constant background (B) and a phase factor (C).

$$T(L) = \frac{A}{1 + \frac{4F^2}{\pi^2}\sin^2(\frac{2\pi nL}{\lambda} + C)} + B \tag{5.13}$$

Figure 5.15 shows the fast scans at each count rate. Using the durations from Table 5.5, the signal is lost in the noise at the lowest level. This could be improved with longer acquisition times, and may be partly due to an unexpectedly high dark count rate. Figure 5.16 illustrates that the dark count rate can have a significant impact on the signal to noise level. However, this variation in dark count rate will not have caused a comparable change in efficiency; Figure 5.17 shows that the dark counts vary more strongly as a function of SNSPD bias current than system detection efficiency.

Figures 5.18 - 5.20 show the high quality scans that were conducted at the three higher count rates. Each maximum is in the same position, indicating that there was no significant drift during the data acquisition period. Fits to these data indicate that the resolution is fairly consistent, but some asymmetry is observed at the lowest count rate. This could be caused by the slower scan rate being closer to the drift rate.

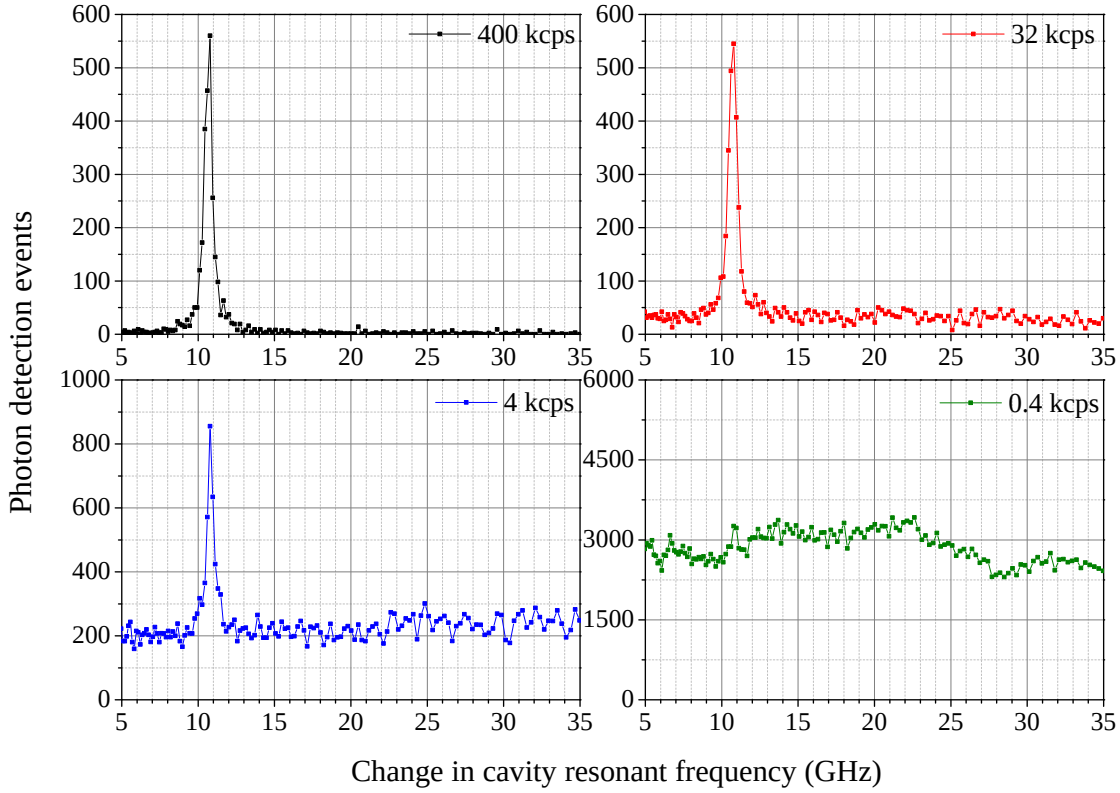

Figure 5.15: **Fast scan tests at 4 different levels of photon flux.** Plots correspond to 400 kcps, 32 kcps, 4 kcps, 0.4 kcps. The lowest signal level is lost in the background.

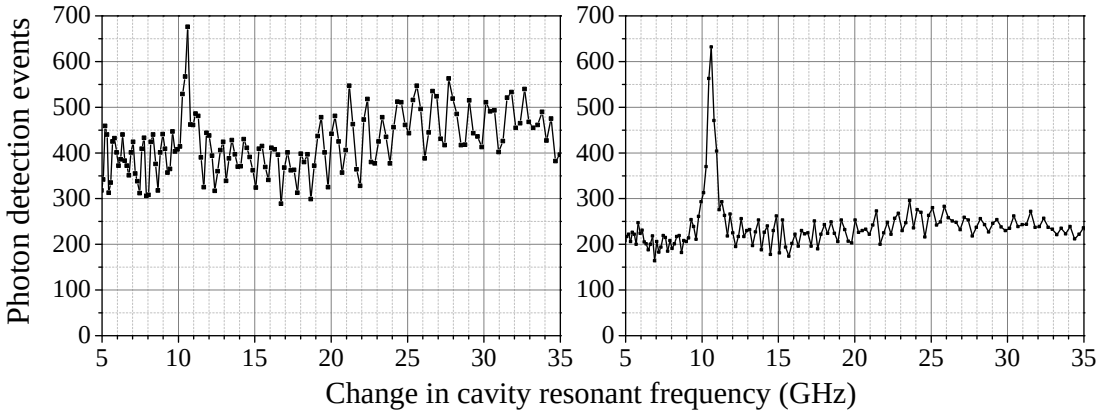

Figure 5.16: **Impact of dark count rate on cavity scan data.** Cavity scans measuring the same level of incident light with the SNSPD operating at a dark count rate of ~ 3 kHz *(left)* and ~ 1.5 kHz *(right)*.

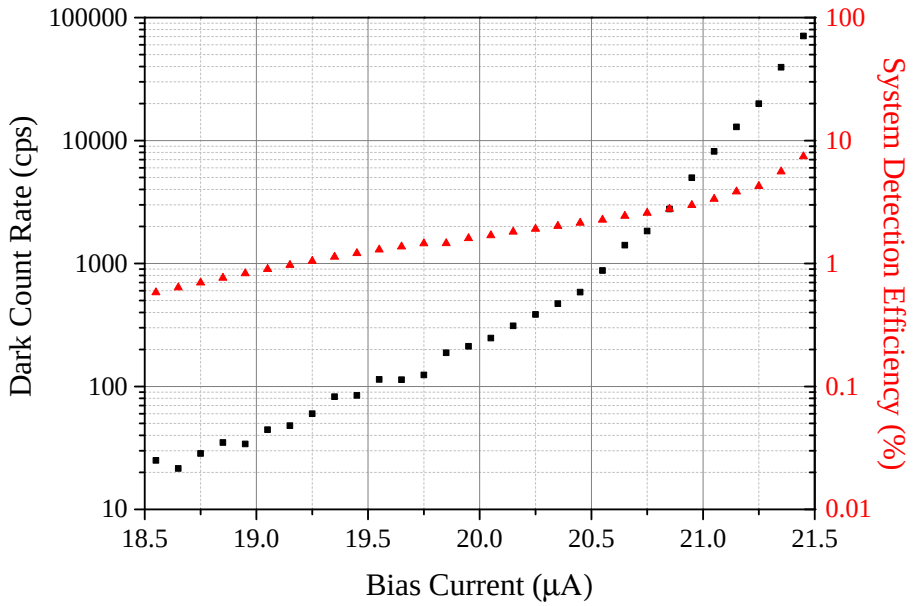

Figure 5.17: **SNSPD efficiency and dark count rate versus bias current.** The dark count rate varies faster with bias current than the system detection efficiency; consequently, a change in operating temperature that causes a noticeable rise in dark count rate may not significantly affect the efficiency.

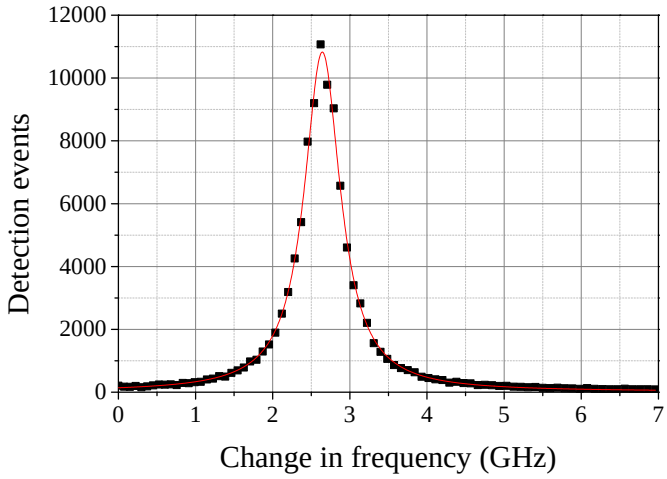

Figure 5.18: **Resolution vs photon flux (1).** Count rate = 440 kcps. Data acquired in 2 min 4 sec, cavity linewidth = (569 ± 3) MHz

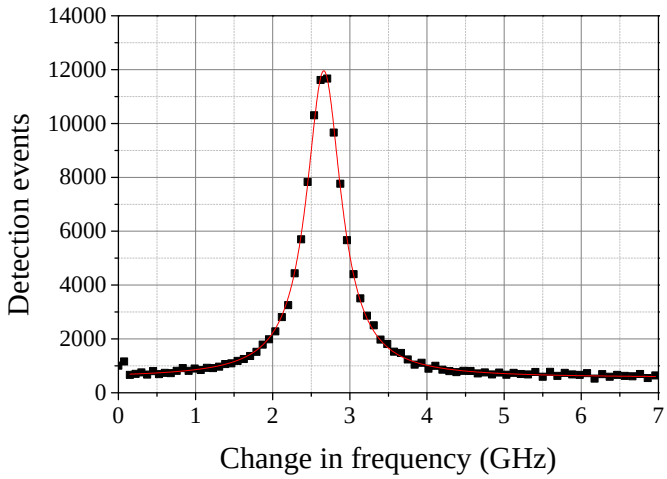

Figure 5.19: **Resolution vs photon flux (2).** Count rate = 32 kcps. Data acquired in 2 min 12 sec, cavity linewidth = (546 ± 2) MHz

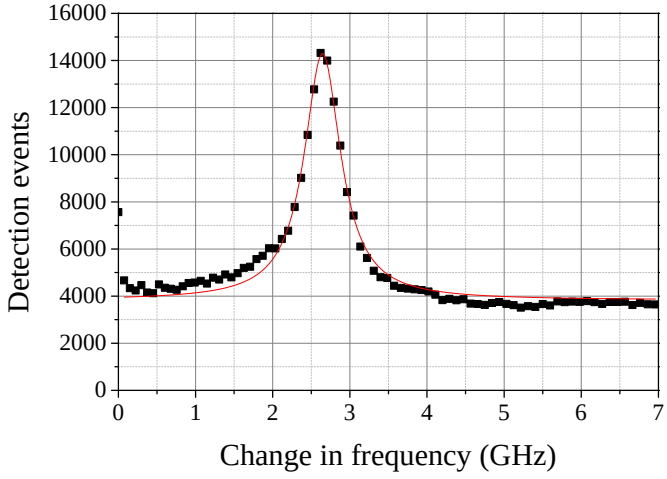

Figure 5.20: **Resolution vs photon flux (3).** Count rate = 4 kcps. Data acquired in 5 min 6 sec, cavity linewidth = (576 ± 6) MHz.

5.7 Summary and future work

To summarise, a SFPI system has been designed and built for the characterisation of telecom-wavelength single-photon sources, and has been demonstrated to work down to a level of 4 kcps. The design resolution and FSR were 600 MHz and 150 GHz respectively; the constructed system was measured to have a resolution of ~ 550 MHz at 1310 nm, and a FSR = (119.0 ± 0.4) GHz. While the cavity is longer than the design value, it is still ample to meet the spectral range requirements outlined in Section 5.3.1.

A total transmission of 74 % was observed between the entrance and the exit of the cavity housing. As the calculated maximum possible transmission is 87.4 %, there may be scope to increase the transmitted intensity by improving the cavity stability or the mode matching of the incoming beam with the cavity mode. The percentage of the transmitted light that was coupled into the TEM_{00} mode was estimated to be 89 %. The light exiting the cavity was coupled into the output fibre with 65 % efficiency, giving an overall transmission from the exit of the delivery fibre to the exit of the output fibre of ~ 48 %. It should be possible to increase this value by improving the coupling into the output fibre.

Other measurements that would contribute to a more complete characterisation of the cavity include determining the upper limit on source intensity that does not cause appreciable drift in the cavity length, and investigating the settling time of the actuators in order to potentially increase the data acquisition speed, which reduces the exposure of the measurements to resonant frequency drift. Measurements of the cavity linewidth for input wavelengths from 1270 nm to 1630 nm would provide data on how constant the resolution is over the intended operating range. Finally, a thorough investigation of scan and drift rates might elucidate the reason for the asymmetry in Figure 5.20 and better define the instrument's operational limits.

With the SFPI system thoroughly characterised, it will be possible to use it to perform high-resolution spectroscopy on a range of sources, in order to assess their suitability for applications in quantum photonics.

Chapter 6

Conclusions

The commercialisation of quantum technologies such as QKD makes it imperative that a clear framework of measurement standards is developed for single-photon devices [9]. Furthermore, the current disparity between single-photon device performance and the requirements of quantum computing is fuelling intensive research efforts that would benefit from optimised characterisation techniques. The purpose of the work presented in this thesis is to contribute to the development of single-photon metrology at NPL with a view to meeting these measurement needs.

The focus of the presented research was on devices that are compatible with telecom wavelengths, namely the superconducting nanowire single-photon detector (SNSPD) and self-assembled semiconductor quantum dot (QD) single-photon sources. This is because wavelengths that experience the least loss in optical fibre have the greatest potential to be integrated into commercial quantum systems. Following the loss of a key QD sample, work on single-photon metrology at telecom wavelengths continued with an alternative project in which an instrument was developed for high-resolution spectral characterisation at the single-photon level.

NPL identified the SNSPD as a promising emerging technology; consequently, the first project in this EngD involved the construction and characterisation of a SNSPD system. It was constructed at Heriot-Watt University under the supervision of Dr. Robert Hadfield, then delivered to NPL in December 2009 [211]. As described in Chapter 3, the two-channel system was confirmed to provide excellent timing resolution ($<$ 90 ps FWHM), low dark counts and system detection efficiencies

that compared well with other systems reported around the same time ($\sim$ 1% at 1 kHz dark count rate for an input wavelength of 1310 nm). A comparison with the existing single-photon detectors at NPL (see Section 3.4) demonstrated the significant improvement in timing resolution provided by the new SNSPD system, which was then used in measurements presented in Chapters 4 and 5.

As the main candidate for single-photon production at telecom wavelengths [34], measurements on QD single-photon sources are an important part of metrology for commercial photonic systems. The sample investigated in this work and Ref [187] contained QDs with emission wavelengths around 900 nm and provided valuable experience of working with QDs in advance of having the detectors for similar investigations at telecom wavelengths. The techniques can be transferred to telecom wavelengths by using optics with different coatings and appropriate detectors. In this work, the impact of pump wavelength on measurements of the second-order correlation function was investigated. In accordance with recent literature [178], preliminary results indicated that a significant improvement could be achieved by exciting the quantum dots near-resonantly, exciting electron-hole pairs within the quantum dot potential, as opposed to exciting the sample above-band and producing charge carriers in the bulk material and wetting layer. Values of $g^{(2)}(\tau = 0) = 0.12 \pm 0.04$ for above-band and $g^{(2)}(\tau = 0) = 0.07 \pm 0.05$ for near-resonant pumping were made before sample damage prevented further measurements.

Apparatus for conducting a Hong-Ou-Mandel experiment comparable to that presented in [124] was constructed and characterised in order to make further measurements on the QD sample. The operation of the arrangement was tested using an attenuated pulsed laser as a source. The excellent timing resolution of the SNSPD enabled the temporal overlap of the two photon paths to be accurately characterised (see Section 4.5). Unfortunately, the planned experiment was not carried out due to damage to the QD sample.

This setback necessitated a change of emphasis. An alternative goal was formulated, namely the design and construction of a high-resolution single-photon spectrometer for telecom wavelengths. The system is a temperature-stabilised scanning

Fabry Pérot interferometer (SFPI); broadband optical coatings provide consistent resolution across the range of wavelengths used in telecoms wavelength-division multiplexing (1270 nm to 1630 nm). The system met the measurement requirements outlined in the design process; it has a free spectral range of (119.0 ± 0.4) GHz and resolution of (576 ± 6) MHz at a wavelength of 1310 nm and single-photon count rate of 4 kcps.

The development and operation of this SFPI instrument is likely to be of interest to the research community investigating photonic sources at telecom wavelengths. While systems with higher resolutions and smaller spectral ranges have been reported at wavelengths around 900 nm [46, 47], this instrument has been specifically designed to focus on the needs of source characterisation for quantum photonic technologies. The SFPI will be used in investigations of the spectral stability of laser pulses during QKD encoding processes. It will also be useful for investigations into the fine-structure splitting of QD transitions, and work on tuning multiple transitions to the point of degeneracy in order to generate entangled photon states.

The work presented in this thesis will be useful to future investigations of photonic sources at telecom wavelengths. The SNSPD system provides a means of detecting telecom wavelength emission, which would be necessary in investigations of QD samples to locate suitable single-photon emitters. It is also planned to use the SNSPD system in investigations of the effect of encoding processes on the spectral profile of optical pulses for use in QKD.

In conjunction with the presented arrangement for a Hong-Ou-Mandel experiment, the SNSPD system opens up the possibility of investigating the impact of timing jitter on the visibility of two-photon interference. Recent publications that use CW rather than pulsed excitation schemes have suggested that their results would be improved with better timing resolution [212]. Upon location of a single-photon source with a sufficient level of indistinguishability, this setup could also be used to generate polarisation-entangled photon pairs.

While the benefits of the constructed SNSPD system to NPL have been clearly demonstrated, this technology has seen immense improvements in performance over

the duration of this EngD. While 1 % system detection efficiency at telecom wavelengths was common in 2009, many similar systems now report efficiencies in excess of 23 % [73, 92, 93] which would make the acquisition of correlation histograms faster by more than a factor of 400. Additionally, developments in the last year have shown amorphous W-Si nanowires in cavity structures to yield another jump in system detection efficiencies to greater than 90 % [75], albeit at a lower operating temperature. The SNSPD is therefore likely to feature prominently in the quantum photonics experiments of the near future. The system at NPL has been constructed to facilitate straightforward upgrades to other fibre-coupled nanowire devices requiring comparable operating environments.

The technology for developing QD single-photon sources has also seen considerable progress in recent years. While micropillar cavities provide a significant improvement over QDs in bulk material, the stochastic positioning of self-assembled QDs makes locating a suitable source a time-consuming process. Control over the size [170], position [174] and even the shape of QDs [175] has now been demonstrated, providing considerable scope for the development of samples with higher yields of single-photon sources. Additionally, tapered nanowire cavities have been shown to improve the spatial mode of the emitted light such that coupling efficiencies have been greatly improved [116]. The opportunity to work with QD samples developed with current state-of-the-art techniques could therefore provide a straightforward route to performing some of the experiments described above and optimising single-photon characterisation techniques.

This work has provided NPL with two important capabilities for benchmarking components for next-generation quantum photonics. Firstly, the SNSPD system provides the capability to detect telecom-wavelength single photons with excellent timing resolution. Secondly, the SFPI instrument facilitates the characterisation of telecom-wavelength photonic sources at the single-photon level with excellent spectral resolution. Given the rapid progress in the performance of SNSPDs and single-photon sources over the last four years, it will be very interesting to see what the next four bring in terms of advances in quantum optics, development of quantum photonic devices and new commercial products for real world use.

References

[1] N. Gisin, G. Ribordy, W. Tittel, and H. Zbinden. "Quantum cryptography". *Rev. Mod. Phys.* **74**, 145 (2002).

[2] T. D. Ladd, F. Jelezko, R. Laflamme, Y. Nakamura, C. Monroe, and J. L. O'Brien. "Quantum computers". *Nature* **464**, 45 (2010).

[3] V. Giovannetti, S. Lloyd, and L. Maccone. "Advances in quantum metrology". *Nature Photon.* **5**, 222 (2011).

[4] ID Quantique: `http://www.idquantique.com/`
QuintessenceLabs `http://qlabsusa.com/`
MagiQ: `http://www.magiqtech.com/`
Single Quantum: `www.singlequantum.com`.

[5] T. Wilk, S. C. Webster, A. Kuhn, and G. Rempe. "Single-atom single-photon quantum interface". *Science* **317**, 488–490 (2007).

[6] D. Fattal, E. Diamanti, K. Inoue, and Y. Yamamoto. "Quantum teleportation with a quantum dot single photon source". *Phys. Rev. Lett.* **92**, 37904 (2004).

[7] J. L. O'Brien, A. Furusawa, and J. Vuckovic. "Photonic quantum technologies". *Nature Photon.* **3**, 687–695 (2009).

[8] E. Knill, R. Laflamme, and G. J. Milburn. "A scheme for efficient quantum computation with linear optics". *Nature* **409**, 46–52 (2001).

[9] T. Länger and G. Lenhart. "Standardization of quantum key distribution and the ETSI standardization initiative ISG-QKD". *New J. Phys.* **11**, 055051 (2009).

[10] Office for National Statistics. "Statistical bulletin: Retail sales, January 2013". `http://www.ons.gov.uk/ons/rel/rsi/retail-sales/january-2013/stb-rsi-january-2013.html`.

[11] R. L. Rivest, A. Shamir, and L. Adleman. "A method for obtaining digital signatures and public-key cryptosystems". *Commun. ACM* **21**, 120–126 (1978).

[12] V. Scarani, H. Bechmann-Pasquinucci, N. Cerf, M. Dusek, N. Lütkenhaus, and M. Peev. "The security of practical quantum key distribution". *Rev. Mod. Phys.* **81**, 1301 (2009).

[13] M. A. Nielsen and I. L. Chuang. *Quantum computation and quantum information* (Cambridge university press, 2000).

[14] C. H. Bennett and G. Brassard. *Proceedings of IEEE International Conference on Computers, Systems and Signal Processing.* In , vol. 175 (Bangalore, India, 1984).

[15] M. Fox. *Quantum Optics: An Introduction.* Oxford Master Series in Physics (Oxford University Press, Oxford, 2006).

[16] H. Takesue, S. W. Nam, Q. Zhang, R. H. Hadfield, T. Honjo, K. Tamaki, and Y. Yamamoto. "Quantum key distribution over a 40-dB channel loss using superconducting single-photon detectors". *Nature Photon.* **1**, 343–348 (2007).

[17] A. R. Dixon, Z. L. Yuan, J. F. Dynes, A. W. Sharpe, and A. J. Shields. "Gigahertz decoy quantum key distribution with 1 Mbit/s secure key rate". *Opt. Express* **16**, 18790 (2008).

[18] D. Stucki, N. Walenta, F. Vannel, R. Thew, N. Gisin, H. Zbinden, S. Gray, C. Towery, and S. Ten. "High rate, long-distance quantum key distribution over 250 km of ultra low loss fibres". *New J. Phys.* **11**, 075003 (2009).

[19] G. Brassard, N. Lutkenhaus, T. Mor, and B. C. Sanders. "Limitations on practical quantum cryptography". *Phys. Rev. Lett.* **85**, 1330–3 (2000).

[20] H.-K. Lo, X. Ma, and K. Chen. "Decoy state quantum key distribution". *Phys. Rev. Lett.* **94**, 230504 (2005).

[21] X.-B. Wang. "Beating the photon-number-splitting attack in practical quantum cryptography". *Phys. Rev. Lett.* **94**, 230503 (2005).

[22] T. Schmitt-Manderbach, H. Weier, M. Fürst, R. Ursin, F. Tiefenbacher, T. Scheidl, J. Perdigues, Z. Sodnik, C. Kurtsiefer, J. G. Rarity, A. Zeilinger, and H. Weinfurter. "Experimental demonstration of free-space decoy-state quantum key distribution over 144km". *Phys. Rev. Lett.* **98**, 010504 (2007).

[23] A. Beveratos, R. Brouri, T. Gacoin, A. Villing, J. P. Poizat, and P. Grangier. "Single photon quantum cryptography". *Phys. Rev. Lett.* **89**, 187901 (2002).

[24] P. M. Intallura, M. B. Ward, O. Z. Karimov, Z. L. Yuan, P. See, A. J. Shields, P. Atkinson, and D. A. Ritchie. "Quantum key distribution using a triggered quantum dot source emitting near 1.3 μm". *Appl. Phys. Lett.* **91**, 161103 (2007).

[25] E. Waks, K. Inoue, C. Santori, D. Fattal, J. Vuckovic, G. S. Solomon, and Y. Yamamoto. "Secure communication quantum cryptography with a photon turnstile". *Nature* **420**, 762 (2002).

[26] E. Meyer-Scott, Z. Yan, A. MacDonald, J.-P. Bourgoin, H. Hübel, and T. Jennewein. "How to implement decoy-state quantum key distribution for a satellite uplink with 50-dB channel loss". *Phys. Rev. A* **84**, 062326 (2011).

[27] A. K. Ekert. "Quantum cryoptography based on Bell's theorem". *Phys. Rev. Lett.* **67**, 661 (1991).

[28] H.-K. Lo, M. Curty, and B. Qi. "Measurement-device-independent quantum key distribution". *Phys. Rev. Lett.* **108**, 130503 (2012).

[29] P. Villoresi, J. T, F. Tamburini, M. Aspelmeyer, C. Bonato, R. Ursin, C. Pernechele, V. Lucen, G. Bianco, A. Zeilinger, and C. Barbieri. "Experimental verification of the feasibility of a quantum channel between space and earth". *New J. Phys.* **10**, 033038 (2008).

[30] N. Gisin and R. Thew. "Quantum communication". *Nature Photon.* **1**, 166 (2007).

[31] N. Sangouard, C. Simon, J. Minář, H. Zbinden, H. de Riedmatten, and N. Gisin. "Long-distance entanglement distribution with single-photon sources". *Phys. Rev. A* **76**, 050301 (2007).

[32] L. Lydersen, C. Wiechers, C. Wittmann, D. Elser, J. Skaar, and V. Makarov. "Hacking commercial quantum cryptography systems by tailored bright illumination". *Nature Photon.* **4**, 5–8 (2010).

[33] Y. H. Shih. "Entangled biphoton source: Property and preparation". *Rep. Prog. Phys.* **66**, 1009–1044 (2003).

[34] J. L. O'Brien. "Optical quantum computing". *Science* **318**, 1567–1570 (2007).

[35] A. Politi, J. C. Matthews, and J. L. O'Brien. "Shors quantum factoring algorithm on a photonic chip". *Science* **325**, 1221–1221 (2009).

[36] E. Martín-López, A. Laing, T. Lawson, R. Alvarez, X.-Q. Zhou, and J. L. O'Brien. "Experimental realization of Shor's quantum factoring algorithm using qubit recycling". *Nature Photon.* **6**, 773 (2012).

[37] M. Varnava, D. Browne, and T. Rudolph. "How good must single photon sources and detectors be for efficient linear optical quantum computation?". *Phys. Rev. Lett.* **100**, 60502 (2008).

[38] S. Cova, M. Ghioni, F. Zappa, I. Rech, A. Gulinatti, and P. Maccagnani. "Silicon single photon avalanche diodes situation and prospect". *Proc. SPIE* **6583**, 658302 (2007).

[39] M. D. Eisaman, J. Fan, A. Migdall, and S. V. Polyakov. "Invited review article single-photon sources and detectors". *Rev. Sci. Instrum.* **82**, 071101 (2011).

[40] R. H. Hadfield. "Single-photon detectors for optical quantum information applications". *Nature Photon.* **3**, 696–705 (2009).

[41] C. Roberts (2013). Corning Inc., *private communication*.

[42] A. J. Shields. "Semiconductor quantum light sources". *Nature Photon.* **1**, 215–223 (2007).

[43] M. B. Ward, O. Z. Karimov, D. C. Unitt, Z. L. Yuan, P. See, D. G. Gevaux, A. J. Shields, P. Atkinson, and D. A. Ritchie. "On-demand single-photon source for 1.3 μm telecom fiber". *Appl. Phys. Lett.* **86**, 201111 (2005).

[44] R. Hanbury Brown and R. Twiss. "Correlation between photons in two coherent beams of light". *Nature* **177**, 27–32 (1956).

[45] C. K. Hong, Z. Y. Ou, and L. Mandel. "Measurement of subpicosecond time intervals between two photons by interference". *Phys. Rev. Lett.* **59**, 2044 (1987).

[46] R. Hafenbrak, S. M. Ulrich, P. Michler, L. Wang, A. Rastelli, and S. O. G. "Triggered polarization-entangled photon pairs from a single quantum dot up to 30K". *New J. Phys.* **9**, 315 (2007).

[47] S. Ates, S. Ulrich, S. Reitzenstein, A. Löffler, A. Forchel, and P. Michler. "Post-selected indistinguishable photons from the resonance fluorescence of a single quantum dot in a microcavity". *Phys. Rev. Lett.* **103**, 1–4 (2009).

[48] R. B. Patel, A. J. Bennett, I. Farrer, C. A. Nicoll, D. A. Ritchie, and A. J. Shields. "Two-photon interference of the emission from electrically tunable remote quantum dots". *Nature Photon.* **4**, 632–635 (2010).

[49] R. E. Warburton, A. McCarthy, A. M. Wallace, S. Hernandez-Marin, R. H. Hadfield, S. W. Nam, and G. S. Buller. "Subcentimeter depth resolution using a single-photon counting time-of-flight laser ranging system at 1550nm wavelength". *Opt. Lett.* **32**, 2266 (2007).

[50] W. E. Moerner and M. Orrit. "Illuminating single molecules in condensed matter". *Science* **283**, 1670–1676 (1999).

[51] A. Divochiy, F. Marsili, D. Bitauld, A. Gaggero, R. Leoni, F. Mattioli, A. Korneev, V. Seleznev, N. Kaurova, O. Minaeva, G. Gol'tsman, K. Lagoudakis, M. Benkhaoul, F. Lévy, and A. Fiore. "Superconducting nanowire photon-number-resolving detector at telecommunication wavelengths". *Nature Photon.* **2**, 302 (2008).

[52] J. Y. Cheung, C. J. Chunnilall, E. R. Woolliams, N. P. Fox, J. R. Mountford, J. Wang, and P. J. Thomas. "The quantum candela a re-definition of the standard units for optical radiation". *J. Mod. Opt.* **54**, 373 (2007).

[53] C. M. Natarajan, M. Härtig, R. Warburton, G. S. Buller, R. H. Hadfield, B. Baek, S. W. Nam, S. Miki, M. Fujiwara, M. Sasaki, and Z. Wang. "Superconducting nanowire single-photon detectors for quantum communication applications". *Quantum Communication and Quantum Networking: Lecture Notes of the Institute for Computer Sciences, Social Informatics and Telecommunications Engineering* **36**, 225–232 (2010).

[54] G. Knoll. *Radiation Detection and Measurement* (John Wiley & Sons, 2010).

[55] S. Cova, A. Longoni, and A. Andreoni. "Towards picosecond resolution with single-photon avalanche diodes". *Rev. Sci. Instrum.* **52**, 408 (1981).

[56] M. A. Itzler, R. Ben-Michael, C.-F. Hsu, K. Slomkowski, A. Tosi, S. Cova, F. Zappa, and R. Ispasoiu. "Single photon avalanche diodes for 1.5 μm photon counting applications". *J. Mod. Opt.* **54**, 283–304 (2007).

[57] O. Thomas, Z. L. Yuan, J. F. Dynes, A. W. Sharpe, and A. J. Shields. "Efficient photon number detection with silicon avalanche photodiodes". *Appl. Phys. Lett.* **97**, 031102 (2010).

[58] Z. Yan, D. R. Hamel, A. K. Heinrichs, X. Jiang, M. A. Itzler, and T. Jennewein. "An ultra low noise telecom wavelength free running single photon detector using negative feedback avalanche diode". *Rev. Sci. Instrum.* **83**, 073105 (2012).

[59] S. Takeuchi, J. Kim, Y. Yamamoto, and H. H. Hogue. "Development of a high-quantum-efficiency single-photon counting system". *Appl. Phys. Lett.* **74**, 1063 (1999).

[60] J. Kim, S. Takeuchi, Y. Yamamoto, and H. H. Hogue. "Multiphoton detection using visible light photon counter". *Appl. Phys. Lett.* **74**, 902 (1999).

[61] E. Waks, K. Inoue, W. K. Oliver, E. Diamanti, and Y. Yamamoto. "High-efficiency photon-number detection for quantum information processing". *IEEE J. Sel. Top. Quant. Electron.* **9**, 1502 (2003).

[62] M. Albota and F. Wong. "Efficient single-photon counting at 1.55 μm by means of frequency upconversion". *Opt. Lett.* **29**, 1449 (2004).

[63] A. P. VanDevender and P. G. Kwiat. "High efficiency single photon detection via frequency up-conversion". *J. Mod. Opt.* **51**, 1433–1445 (2004).

[64] J. S. Pelc, L. Ma, C. R. Phillips, Q. Zhang, C. Langrock, O. Slattery, X. Tang, and M. M. Fejer. "Long-wavelength-pumped upconversion single-photon detector at 1550 nm: Performance and noise analysis". *Opt. Express* **19**, 21445–21456 (2011).

[65] G. Gol'tsman, O. Okunev, G. Chulkova, A. Lipatov, A. Semenov, K. Smirnov, B. Voronov, A. Dzardanov, C. Williams, and R. Sobolewski. "Picosecond superconducting single-photon optical detector". *Appl. Phys. Lett.* **79**, 705 (2001).

[66] B. Cabrera, R. M. Clarke, P. Colling, A. J. Miller, S. Nam, and R. W. Romani. "Detection of single infrared, optical, and ultraviolet photons using superconducting transition edge sensors". *Appl. Phys. Lett.* **73**, 735–737 (1998).

[67] D. Rosenberg, A. E. Lita, A. J. Miller, and S. W. Nam. "Noise-free high-efficiency photon-number-resolving detectors". *Phys. Rev. A* **71**, 61803 (2005).

[68] T. Gerrits, B. Calkins, N. Tomlin, A. E. Lita, A. Migdall, R. Mirin, and S. W. Nam. "Extending single-photon optimized superconducting transition edge sensors beyond the single-photon counting regime". *Opt. Express* **20**, 23798–23810 (2012).

[69] D. Fukuda, G. Fujii, T. Numata, K. Amemiya, A. Yoshizawa, H. Tsuchida, H. Fujino, H. Ishii, T. Itatani, S. Inoue, and T. Zama. "Titanium-based transition-edge photon number resolving detector with 98% detection efficiency with index-matched small-gap fiber coupling". *Opt. Express* **19**, 870–5 (2011).

[70] A. E. Lita, A. J. Miller, and S. W. Nam. "Counting near infrared single photons with 95 percent efficiency". *Opt. Express* **16**, 3032 (2008).

[71] E. A. Dauler, A. J. Kerman, B. S. Robinson, J. K. Yang, B. Voronov, G. Gol'tsman, S. A. Hamilton, and K. K. Berggren. "Photon-number-resolution with sub-30-ps timing using multi-element superconducting nanowire single photon detectors". *J. Mod. Opt.* **56**, 364–373 (2009).

[72] X. Hu, E. A. Dauler, R. J. Molnar, and K. K. Berggren. "Superconducting nanowire single-photon detectors integrated with optical nano-antennae". *Opt. Express* **19**, 17–31 (2011).

[73] X. Hu, T. Zhong, J. White, E. A. Dauler, F. Najafi, C. Herder, F. Wong, and K. K. Berggren. "Fiber-coupled nanowire photon counter at 1550 nm with 24% system detection efficiency". *Opt. Lett.* **34**, 3607–3609 (2009).

[74] V. B. Verma, F. Marsili, S. Harrington, A. E. Lita, R. P. Mirin, and S. W. Nam. "A three-dimensional polarization-insensitive superconducting nanowire avalanche photodetector". *Appl. Phys. Lett.* **101**, 251114 (2012).

[75] F. Marsili, V. B. Verma, J. A. Stern, S. Harrington, A. E. Lita, T. Gerrits, I. Vayshenker, B. Baek, M. D. Shaw, R. P. Mirin, and S. W. Nam. "Detecting single infrared photons with 93% system efficiency". *Nature Photon.* **7**, 210–214 (2013).

[76] S. Miki, M. Fujiwara, M. Sasaki, and Z. Wang. "Development of SNSPD system with Gifford-McMahon cryocooler". *IEEE Trans. Appl. Supercond.* **19**, 332–335 (2009).

[77] M. A. Itzler, X. Jiang, M. Entwistle, K. Slomkowski, A. Tosi, F. Acerbi, F. Zappa, and S. Cova. "Advances in InGaAsP-based avalanche diode single photon detectors". *J. Mod. Opt.* **58**, 174–200 (2011).

[78] A. D. Semenov, R. S. Nebosis, Y. P. Gousev, M. A. Heusinger, and K. F. Renk. "Analysis of the nonequilibrium photoresponse of superconducting films to pulsed radiation by use of a two-temperature model". *Phys. Rev. B* **52**, 581 (1995).

[79] A. Kadin and M. Johnson. "Nonequilibrium photon-induced hotspot a new mechanism for photodetection in ultrathin metallic films". *Appl. Phys. Lett.* **69**, 3938 (1996).

[80] A. Semenov, Gol'tsman, and A. Korneev. "Quantum detection by current carrying superconducting film". *Physica C* **351**, 349 (2001).

[81] F. Marsili, F. Bellei, F. Najafi, A. E. Dane, E. A. Dauler, R. J. Molnar, and K. K. Berggren. "Efficient single photon detection from 500 nm to 5 μm wavelength". *Nano Lett.* **12**, 4799 (2012).

[82] M. K. Akhlaghi, H. Atikian, A. Eftekharian, M. Loncar, and A. H. Majedi. "Reduced dark counts in optimised geometries for superconducting nanowire single photon detectors". *Opt. Express* **20**, 23610 (2012).

[83] B. Baek, A. E. Lita, V. Verma, and S. W. Nam. "Superconducting a-WSi nanowire single-photon detector with saturated internal quantum efficiency from visible to 1850 nm". *Appl. Phys. Lett.* **98**, 251105 (2011).

[84] S. Miki, M. Fujiwara, M. Sasaki, B. Baek, A. J. Miller, R. H. Hadfield, S. W. Nam, and Z. Wang. "Large sensitive-area NbN nanowire superconducting single-photon detectors fabricated on single-crystal MgO substrates". *Appl. Phys. Lett.* **92**, 61116 (2008).

[85] A. Verevkin, J. Zhang, R. Sobolewski, A. Lipatov, O. Okunev, G. Chulkova, A. Korneev, K. Smirnov, G. Gol'tsman, and A. Semenov. "Detection efficiency of large-active-area NbN single-photon superconducting detectors in the ultraviolet to near-infrared range". *Appl. Phys. Lett.* **80**, 4687 (2002).

[86] A. J. Kerman, E. A. Dauler, J. K. W. Yang, K. M. Rosfjord, V. Anant, K. K. Berggren, G. Gol'tsman, and B. M. Voronov. "Constriction-limited detection efficiency of superconducting nanowire single-photon detectors". *Appl. Phys. Lett.* **90**, 101110 (2007).

[87] R. H. Hadfield, P. Dalgarno, J. O'Connor, E. Ramsay, R. J. Warburton, E. J. Gansen, B. Baek, M. J. Stevens, R. P. Mirin, and S. W. Nam. "Submicrometer photoresponse mapping of nanowire superconducting single-photon detectors". *Appl. Phys. Lett.* **91**, 241108 (2007).

[88] F. Mattioli, M. Ejrnaes, A. Gaggero, A. Casaburi, R. Cristiano, S. Pagano, and R. Leoni. "Large area single photon detectors based on parallel configuration NbN nanowires". *J. Vac. Sci. Technol. B* **30**, 031204 (2012).

[89] D. Rosenberg, A. J. Kerman, R. J. Molnar, and E. A. Dauler. "High-speed and high-efficiency superconducting nanowire single photon detector array". *Opt. Express* **21**, 1440–1447 (2013).

[90] K. M. Rosfjord, J. K. W. Yang, E. A. Dauler, A. J. Kerman, V. Anant, B. M. Voronov, G. Gol'tsman, and K. K. Berggren. "Nanowire single-photon detector with an integrated optical cavity and anti-reflection coating". *Opt. Express* **14**, 527 (2006).

[91] B. Baek, J. A. Stern, and S. W. Nam. "Superconducting nanowire single-photon detector in an optical cavity for front-side illumination". *Appl. Phys. Lett.* **95**, 191110 (2009).

[92] S. Miki, M. Takeda, M. Fujiwara, M. Sasaki, and Z. Wang. "Compactly packaged superconducting nanowire single-photon detector with an optical cavity for multichannel system". *Opt. Express* **17**, 23557–23564 (2009).

[93] M. G. Tanner, C. M. Natarajan, V. Pottapenjara, J. O'Connor, R. J. Warburton, R. H. Hadfield, B. Baek, S. W. Nam, S. Dorenbos, E. Ureña, T. Zijlstra, T. Klapwijk, and V. Zwiller. "Enhanced telecom wavelength single-photon detection with NbTiN superconducting nanowires on oxidized silicon". *Appl. Phys. Lett.* **96**, 221109 (2010).

[94] S. Dorenbos, E. Reiger, N. Akopian, U. Perinetti, V. Zwiller, T. Zijlstra, and T. Klapwijk. "Superconducting single photon detectors with minimised polarisation dependence". *Appl. Phys. Lett.* **93**, 161102 (2008).

[95] A. Korneev, Y. Vachtomin, O. Minaeva, A. Divochiy, K. Smirnov, O. Okunev, G. Gol'tsman, C. Zinoni, N. Chauvin, L. Balet, F. Marsili, D. Bitauld, B. Alloing, L. Lianhe, A. Fiore, L. Lunghi, A. Gerardino, M. Halder, C. Jorel, and H. Zbinden. "Single-photon detection system for quantum optics applications". *IEEE J. Sel. Top. Quant. Electron.* **13**, 944 (2007).

[96] F. Marsili, D. Bitauld, A. Fiore, A. Gaggero, F. Mattioli, R. Leoni, M. Benkhaoul, and F. Lévy. "High efficiency NbN nanowire superconducting single photon detectors fabricated on MgO substrates from a low temperature process". *Opt. Express* **16**, 3191 (2008).

[97] M. G. Tanner, L. S. E. Alvarez, W. Jiang, R. J. Warburton, Z. H. Barber, and R. H. Hadfield. "A superconducting nanowire single photon detector on lithium niobate". *Nanotechnology* **23**, 505201 (2012).

[98] C. Schuck, W. H. P. Pernice, and H. X. Tang. "NbTiN superconducting nanowire detectors for visible and telecom wavelengths single photon counting on Si_3N_4 photonic circuits". *Appl. Phys. Lett.* **102**, 051101 (2013).

[99] V. Anant, A. J. Kerman, E. A. Dauler, J. K. W. Yang, K. M. Rosfjord, and K. K. Berggren. "Optical properties of superconducting nanowire single-photon detectors". *Opt. Express* **16**, 10750 (2008).

[100] E. Driessen, F. Braakman, E. Reiger, S. Dorenbos, V. Zwiller, and M. de Dood. "Impedance model for the polarization-dependent optical absorption of superconducting single-photon detectors". *Eur. Phys. J. Appl. Phys.* **47**, 10701 (2009).

[101] J. Yang, A. Kerman, E. Dauler, V. Anant, K. Rosfjord, and K. Berggren. "Modeling the electrical and thermal response of superconducting nanowire single-photon detectors". *IEEE Trans. Appl. Supercond.* **17**, 581 –585 (2007).

[102] A. J. Kerman, E. A. Dauler, W. Keicher, J. K. W. Yang, K. K. Berggren, G. Gol'tsman, and B. Voronov. "Kinetic-inductance-limited reset time of

superconducting nanowire photon counters". *Appl. Phys. Lett.* **88**, 111116 (2006).

[103] E. A. Dauler, B. S. Robinson, A. J. Kerman, J. K. W. Yang, K. M. Rosfjord, V. Anant, B. M. Voronov, G. Gol'tsman, and K. K. Berggren. "Multi-element superconducting nanowire single-photon detector". *IEEE Trans. Appl. Supercond.* **17**, 279 (2007).

[104] E. A. Dauler, M. J. Stevens, B. Baek, R. J. Molnar, S. A. Hamilton, R. P. Mirin, S. W. Nam, and K. K. Berggren. "Measuring intensity correlations with a two-element superconducting nanowire single-photon detector". *Phys. Rev. A* **78**, 53826 (2008).

[105] F. Marsili, F. Najafi, E. Dauler, F. Bellei, X. Hu, M. Csete, R. J. Molnar, and K. K. Berggren. "Single-photon detectors based on ultranarrow superconducting nanowires". *Nano Lett.* **11**, 2048–2053 (2011).

[106] PhotonSpot: `www.photonspot.com`
Scontel: `www.scontel.ru`
Single Quantum: `www.singlequantum.com`.

[107] B. Lounis and M. Orrit. "Single-photon sources". *Rep. Prog. Phys.* **68**, 1129 (2005).

[108] M. Oxborrow and A. G. Sinclair. "Single-photon sources". *Contemporary Physics* **46**, 173 (2005).

[109] S. Scheel. "Single-photon sources - an introduction". *J. Mod. Opt.* **56**, 141 (2009).

[110] A. Kuhn and D. Ljunggren. "Cavity-based single-photon sources". *Contemporary Physics* **51**, 289–313 (2010).

[111] A. J. Bennett, D. C. Unitt, P. See, A. J. Shields, P. Atkinson, K. Cooper, and D. A. Ritchie. "Electrical control of the uncertainty in the time of single photon emission events". *Phys. Rev. B* **72**, 033316 (2005).

[112] M. Hennrich, T. Legero, A. Kuhn, and G. Rempe. "Vacuum-stimulated Raman scattering based on adiabatic passage in a high-finesse optical cavity". *Phys. Rev. Lett.* **85**, 4872–4875 (2000).

[113] A. Kuhn, M. Hennrich, and G. Rempe. "Deterministic single-photon source for distributed quantum networking". *Phys. Rev. Lett.* **89**, 67901 (2002).

[114] M. Pelton, C. Santori, J. Vuckovic, B. Zhang, G. S. Solomon, J. Plant, and Y. Yamamoto. "Efficient source of single photons a single quantum dot in a micropost microcavity". *Phys. Rev. Lett.* **89**, 233602 (2002).

[115] M. Mücke, J. Bochmann, C. Hahn, A. Neuzner, C. Nölleke, A. Reiserer, G. Rempe, and S. Ritter. "Generation of single photons from an atom-cavity system". *Phys. Rev. A* **87**, 063805 (2013).

[116] J. Claudon, J. Bleuse, N. S. Malik, M. Bazin, P. Jaffrennou, N. Gregersen, C. Sauvan, P. Lalanne, and J. M. Gerard. "A highly efficient single-photon source based on a quantum dot in a photonic nanowire". *Nature Photon.* **4**, 174 (2010).

[117] C. Söller, O. Cohen, B. Smith, I. A. Walmsley, and C. Silberhorn. "High-performance single-photon generation with commercial-grade optical fiber". *Phys. Rev. A* **83**, 1–4 (2011).

[118] R. Loudon. *The quantum theory of light.* Oxford science publications (Oxford University Press, 2000).

[119] C. Becher, A. Kiraz, P. Michler, A. Imamoglu, W. V. Schoenfeld, P. M. Petroff, L. Zhang, and E. Hu. "Nonclassical radiation from a single self-assembled InAs quantum dot". *Phys. Rev. B* **63**, 121312 (2001).

[120] H. J. Kimble, M. Dagenais, and L. Mandel. "Photon antibunching in resonance fluorescence". *Phys. Rev. Lett.* **59**, 691 (1977).

[121] J. F. Clauser. "Experimental distinction between the quantum and classical field-theoretic predictions for the photoelectric effect". *Phys. Rev. D* **9**, 853 (1974).

[122] P. Maunz, D. L. Moehring, S. Olmschenk, K. C. Younge, D. N. Matsukevich, and C. Monroe. "Quantum interference of photon pairs from two remote trapped atomic ions". *Nature Phys.* **3**, 538 (2007).

[123] B. Darquie, M. P. A. Jones, J. Dingjan, J. Beugnon, S. Bergamini, Y. Sortais, G. Messin, A. Browaeys, and P. Grangier. "Controlled single-photon emission from a single trapped two-level atom". *Science* **309**, 454–456 (2005).

[124] R. B. Patel, A. J. Bennett, K. Cooper, P. Atkinson, C. A. Nicoll, D. A. Ritchie, and A. J. Shields. "Postselective two-photon interference from a continuous nonclassical stream of photons emitted by a quantum dot". *Phys. Rev. Lett.* **100**, 1–4 (2008).

[125] S. Fasel, O. Alibart, S. Tanzilli, P. Baldi, A. Beveratos, N. Gisin, and H. Zbinden. "High-quality asynchronous heralded single-photon source at telecom wavelength". *New J. Phys.* **6**, 163 (2004).

[126] D. Fattal, K. Inoue, J. Vuckovic, C. Santori, G. S. Solomon, and Y. Yamamoto. "Entanglement formation and violation of bells inequality with a semiconductor single photon source". *Phys. Rev. Lett.* **92**, 37903 (2004).

[127] H. Bachor and T. C. Ralph. *A guide to experiments in quantum optics* (Wiley-VCH Verlag, 2004), 2nd edn.

[128] A. Kiraz, M. Ehrl, T. Hellerer, O. Müstecaphoğlu, C. Bräuchle, and A. Zumbusch. "Indistinguishable photons from a single molecule". *Phys. Rev. Lett.* **94**, 1–4 (2005).

[129] C. Santori, D. Fattal, J. Vuckovic, G. S. Solomon, and Y. Yamamoto. "Indistinguishable photons from a single-photon device". *Nature* **419**, 594–597 (2002).

[130] O. Kuzucu, M. Fiorentino, M. Albota, F. Wong, and F. Kärtner. "Two-photon coincident-frequency entanglement via extended phase matching". *Phys. Rev. Lett.* **94**, 4–7 (2005).

[131] J. Fulconis, O. Alibart, W. Wadsworth, and J. Rarity. "Quantum interference with photon pairs using two micro-structured fibres". *New J. Phys.* **9**, 276 (2007).

[132] M. Jofre, A. Gardelein, G. Anzolin, W. Amaya, J. Capmany, R. Ursin, L. Penate, D. Lopez, J. L. San Juan, J. A. Carrasco, F. Garcia, F. J. Torcal-Milla, L. M. Sanchez-Brea, E. Bernabeu, J. M. Perdigues, T. Jennewein, J. P. Torres, M. W. Mitchell, and V. Pruneri. "Fast optical source for quantum key distribution based on semiconductor optical amplifiers". *Opt. Express* **19**, 3825–3834 (2011).

[133] D. C. Burnham and D. L. Weinberg. "Observation of simultaneity in parametric production of optical photon pairs". *Phys. Rev. Lett.* **25**, 84 (1970).

[134] C. K. Hong and L. Mandel. "Experimental realization of a localized one-photon state". *Phys. Rev. Lett.* **56**, 58–60 (1986).

[135] G. Brida, I. P. Degiovanni, M. Genovese, A. Migdall, F. Piacentini, S. V. Polyakov, and I. Ruo Berchera. "Experimental realization of a low-noise heralded single-photon source". *Opt. Express* **19**, 1484–92 (2011).

[136] P. Mosley, J. Lundeen, B. Smith, P. Wasylczyk, A. U'Ren, C. Silberhorn, and I. A. Walmsley. "Heralded generation of ultrafast single photons in pure quantum states". *Phys. Rev. Lett.* **100**, 1–4 (2008).

[137] M. Fiorentino, S. M. Spillane, R. G. Beausoleil, T. D. Roberts, P. Battle, and M. W. Munro. "Spontaneous parametric down-conversion in periodically poled KTP waveguides and bulk crystals". *Opt. Express* **15**, 7479–7488 (2007).

[138] T. B. Pittman, B. C. Jacobs, and J. D. Franson. "Single photons on pseudo-demand from stored parametric down-conversion". *Phys. Rev. A* **66**, 42303 (2002).

[139] A. L. Migdall, D. Branning, and S. Castelletto. "Tailoring single-photon and multiphoton probabilities of a single-photon on-demand source". *Phys. Rev. A* **66**, 053805 (2002).

[140] J. Rarity, J. Fulconis, J. Duligall, W. Wadsworth, and P. Russell. "Photonic crystal fiber source of correlated photon pairs". *Opt. Express* **13**, 534–544 (2005).

[141] C. Liang, K. F. Lee, M. Medic, P. Kumar, R. H. Hadfield, and S. W. Nam. "Characterization of fiber-generated entangled photon pairs with superconducting single-photon detectors.". *Opt. Express* **15**, 1322–7 (2007).

[142] E. Goldschmidt, M. Eisaman, J. Fan, S. V. Polyakov, and A. Migdall. "Spectrally bright and broad fiber-based heralded single-photon source". *Phys. Rev. A* **78**, 1–4 (2008).

[143] S. Dyer, B. Baek, and S. W. Nam. "High-brightness, low-noise, all-fiber photon pair source". *Opt. Express* **17**, 10290 (2009).

[144] C. K. Law and H. J. Kimble. "Deterministic generation of a bit-stream of single-photon pulses". *J. Mod. Opt.* **44**, 2067–2074 (1997).

[145] J. McKeever, A. Boca, A. D. Boozer, R. Miller, J. R. Buck, A. Kuzmich, and H. J. Kimble. "Deterministic generation of single photons from one atom trapped in a cavity". *Science* **303**, 1992– (2004).

[146] M. Keller, B. Lange, K. Hayasaka, W. Lange, and H. Walther. "Continuous generation of single photons with controlled waveform in an ion-trap cavity system". *Nature* **431**, 1075–1078 (2004).

[147] C. Brunel, B. Lounis, P. Tamarat, and M. Orrit. "Triggered source of single photons based on controlled single molecule fluorescence". *Phys. Rev. Lett.* **83**, 2722–2725 (1999).

[148] P. Michler, A. Kiraz, C. Becher, W. V. Schoenfeld, P. M. Petroff, L. Zhang, E. Hu, and A. Imamoglu. "A quantum dot single-photon turnstile device". *Science* **290**, 2282 (2000).

[149] C. Kurtsiefer, S. Mayer, P. Zarda, and H. Weinfurter. "Stable solid-state source of single photons". *Phys. Rev. Lett.* **85**, 290 (2000).

[150] F. Diedrich and H. Walther. "Nonclassical radiation of a single stored ion". *Phys. Rev. Lett.* **58**, 203 (1987).

[151] M. Hijlkema, B. Weber, H. P. Specht, S. C. Webster, A. Kuhn, and G. Rempe. "A single-photon server with just one atom". *Nature Phys.* **3**, 253 (2007).

[152] H. G. Barros, A. Stute, T. E. Northup, C. Russo, P. O. Schmidt, and R. Blatt. "Deterministic single-photon source from a single ion". *New J. Phys.* **11**, 103004 (2009).

[153] B. B. Blinov, D. L. Moehring, L.-M. Duan, and C. Monroe. "Observation of entanglement between a single trapped atom and a single photon". *Nature* **428**, 153 (2004).

[154] H. P. Specht, J. Bochmann, M. Mücke, B. Weber, E. Figueroa, D. L. Moehring, and G. Rempe. "Phase shaping of single-photon wave packets". *Nature Photon.* **3**, 469 (2009).

[155] S. Kang, S. Lim, M. Hwang, W. Kim, J. Kim, and K. An. "Controlled generation of single photons in a coupled atom-cavity system at a fast repetition rate". *Opt. Express* **19**, 2440–2447 (2011).

[156] T. Basche, W. E. Moerner, M. Orrit, and H. Talon. "Photon antibunching in the fluorescence of a single dye molecule trapped in a solid". *Phys. Rev. Lett.* **69**, 1516 (1992).

[157] B. Lounis and W. E. Moerner. "Single photons on demand from a single molecule at room temperature". *Nature* **407**, 491 (2000).

[158] R. Lettow, Y. L. A. Rezus, A. Renn, G. Zumofen, E. Ikonen, and V. Sandoghdar. "Quantum interference of tunably indistinguishable photons from remote organic molecules". *Phys. Rev. Lett.* **104**, 123605 (2010).

[159] A. Gruber, A. Dräbenstedt, C. Tietz, L. Fleury, J. Wrachtrup, and C. von Borczyskowski. "Scanning confocal optical microscopy and magnetic resonance on single defect centres". *Science* **276**, 2012 (1997).

[160] R. Brouri, A. Beveratos, J. P. Poizat, and P. Grangier. "Photon antibunching in the fluorescence of individual color centers in diamond". *Opt. Lett.* **25**, 1294 (2000).

[161] R. Hubbard, Y. B. Ovchinnikov, J. Y. Cheung, N. Fletcher, R. Murray, and A. G. Sinclair. "Measurements of statistical properties of single photons emitted by a solitary NV centre in synthetic diamond". *J. Mod. Opt.* **54**, 441 (2007).

[162] A. Beveratos, R. Brouri, T. Gacoin, J. P. Poizat, and P. Grangier. "Nonclassical radiation from diamond nanocrystals". *Phys. Rev. A* **64**, 61802 (2001).

[163] T. M. Babinec, B. J. M. Hausmann, M. Khan, Y. Zhang, J. R. Maze, P. R. Hemmer, and M. Lončar. "A diamond nanowire single-photon source". *Nat. Nanotechnol.* **5**, 195 (2010).

[164] J. P. Hadden, J. P. Harrison, A. C. Stanley-Clarke, Y.-L. Marseglia, D. Ho, B. R. Patton, J. L. O'Brien, and J. G. Rarity. "Strongly enhanced photon collection from diamond defect centres under microfabricated integrated solid immersion lenses". *Appl. Phys. Lett.* **97**, 241901 (2010).

[165] C. Zinoni, B. Alloing, C. Monat, V. Zwiller, L. Li, A. Fiore, L. Lunghi, A. Gerardino, H. de Riedmatten, H. Zbinden, and N. Gisin. "Time-resolved and antibunching experiments on single quantum dots at 1300 nm". *Appl. Phys. Lett.* **88**, 131102 (2006).

[166] M. B. Ward, T. Farrow, P. See, Z. L. Yuan, O. Z. Karimov, A. J. Bennett, A. J. Shields, P. Atkinson, K. Cooper, and D. A. Ritchie. "Electrically driven telecommunication wavelength single-photon source". *Appl. Phys. Lett.* **90**, 063512 (2007).

[167] X. Xu, F. Brossard, K. Hammura, D. Williams, B. Alloing, L. Li, and A. Fiore. "Plug and play single photons at 1.3 μm approaching gigahertz operation". *Appl. Phys. Lett.* **93**, 21124 (2008).

[168] D. Leonard, M. Krishnamurthy, C. M. Reaves, S. P. Denbaars, and P. M. Petroff. "Direct formation of quantum-sized dots from uniform coherent islands of InGaAs on GaAs surfaces". *Appl. Phys. Lett.* **63**, 3203–3205 (1993).

[169] S. Malik, C. Roberts, R. Murray, and M. Pate. "Tuning self-assembled InAs quantum dots by rapid thermal annealing". *Appl. Phys. Lett.* **71**, 1987 (1997).

[170] V. B. Verma, M. J. Stevens, K. L. Silverman, N. L. Dias, A. Garg, J. J. Coleman, and R. P. Mirin. "Photon antibunching from a single lithographically defined InGaAs GaAs quantum dot". *Opt. Express* **19**, 4182–4187 (2011).

[171] F. Yang and B. T. Cunningham. "Enhanced quantum dot optical down-conversion using asymmetric 2D photonic crystals". *Opt. Express* **19**, 3908–3918 (2011).

[172] K. De Greve, L. Yu, P. L. McMahon, J. S. Pelc, C. M. Natarajan, N. Y. Kim, E. Abe, S. Maier, C. Schneider, M. Kamp, S. Höfling, R. H. Hadfield, A. Forchel, M. M. Fejer, and Y. Yamamoto. "Quantum-dot spin-photon entanglement via frequency downconversion". *Nature* **491**, 421 (2012).

[173] C. Santori, M. Pelton, G. S. Solomon, Y. Dale, and Y. Yamamoto. "Triggered single photons from a quantum dot". *Phys. Rev. Lett.* **86**, 1502 (2001).

[174] H. Z. Song, T. Usuki, S. Hirose, K. Takemoto, Y. Nakata, and N. Yokoyama. "Site-controlled photoluminescence at telecommunication wavelength from InAsInP quantum dots". *Appl. Phys. Lett.* **86**, 113118 (2005).

[175] A. Mohan, M. Felici, P. Gallo, B. Dwir, A. Rudra, J. Faist, and E. Kapon. "Polarization-entangled photons produced with high-symmetry site-controlled quantum dots". *Nature Photon.* **4**, 302–306 (2010).

[176] Z. Yuan, B. E. Kardynal, R. M. Stevenson, A. J. Shields, C. J. Lobo, K. Cooper, N. S. Beattie, D. A. Ritchie, and M. Pepper. "Electrically driven single-photon source". *Science* **295**, 102–105 (2002).

[177] J. M. Gerard and B. Gayral. "InAs quantum dots: Artificial atoms for solid-state cavity-quantum electrodynamics". *Physica E* **9**, 131 (2001).

[178] A. J. Bennett, D. C. Unitt, P. Atkinson, D. A. Ritchie, and A. J. Shields. "High-efficiency single-photon sources based on InAs/GaAs quantum dots in pillar microcavities". *Physica E* **26**, 391 (2005).

[179] E. M. Purcell. "Spontaneous emission probabilities at radio frequencies". *Phys. Rev.* **69**, 681 (1946).

[180] A. J. Bennett, D. Unitt, P. Atkinson, D. A. Ritchie, and A. J. Shields. "High performance single photon sources from photolithographically defined pillar microcavities". *Opt. Express* **13**, 50 (2005).

[181] A. Kiraz, P. Michler, C. Becher, B. Gayral, A. Imamoglu, L. Zhang, E. Hu, W. V. Schoenfeld, and P. M. Petroff. "Cavity-quantum electrodynamics using a single InAs quantum dot in a microdisk structure". *Appl. Phys. Lett.* **78**, 3932–3934 (2001).

[182] B. Alloing, C. Zinoni, V. Zwiller, L. Li, C. Monat, M. Gobet, G. Buchs, A. Fiore, E. Pelucchi, and E. Kapon. "Growth and characterisation of single quantum dots emitting at 1300nm". *Appl. Phys. Lett.* **86**, 101908 (2005).

[183] M. Herscher. "The spherical mirror Fabry-Perot interferometer". *Appl. Opt.* **7**, 951–966 (1968).

[184] A. Mandelis. "Focus on spectroscopy". *Phys. Today* **65**, 58–61 (2012).

[185] E. B. Flagg, A. Muller, J. W. Robertson, S. Founta, D. G. Deppe, M. Xiao, W. Ma, G. J. Salamo, and C. K. Shih. "Resonantly driven coherent oscillations in a solid-state quantum emitter". *Nature Phys.* **5**, 203–207 (2009).

[186] A. Muller, W. Fang, J. Lawall, and G. S. Solomon. "Emission spectrum of a dressed exciton-biexciton complex in a semiconductor quantum dot". *Phys. Rev. Lett.* **101**, 027401 (2008).

[187] R. Hubbard. *Solid-State Single-Photon Sources : Quantum Dots and the Nitrogen-Vacancy Centre in Diamond*. Ph.D. thesis, Imperial College, University of London (2009).

[188] D. Gammon, E. S. Snow, B. V. Shanabrook, D. S. Katzer, and D. Park. "Fine structure splitting in the optical spectra of single GaAs quantum dots". *Phys. Rev. Lett.* **76**, 3005–3008 (1996).

[189] H. Kim, D. Sridharan, T. C. Shen, G. S. Solomon, and E. Waks. "Strong coupling between two quantum dots and a photonic crystal cavity using magnetic field tuning". *Opt. Express* **19**, 2589–2598 (2011).

[190] R. M. Stevenson, R. M. Thompson, A. J. Shields, I. Farrer, B. E. Kardynal, D. A. Ritchie, and M. Pepper. "Quantum dots as a photon source for passive quantum key encoding". *Phys. Rev. B* **66**, 2–5 (2002).

[191] R. Young, R. M. Stevenson, A. J. Shields, P. Atkinson, K. Cooper, D. A. Ritchie, K. Groom, A. Tartakovskii, and M. Skolnick. "Inversion of exciton level splitting in quantum dots". *Phys. Rev. B* **72**, 113305 (2005).

[192] P. van Veldhoven, N. Chauvin, A. Fiore, and R. Nötzel. "Low density 1.55 μm InAs/InGaAs/InP (100) quantum dots enabled by an ultrathin GaAs interlayer". *Appl. Phys. Lett.* **95**, 113110 (2009).

[193] B. Baek, L. Ma, A. Mink, X. Tang, and S. W. Nam. "Detector performance in long-distance quantum key distribution using superconducting nanowire single-photon detectors". *Proc. SPIE* **7320**, 73200D (2009).

[194] R. H. Hadfield, M. J. Stevens, S. M. Gruber, A. J. Miller, R. E. Schwall, R. P. Mirin, and S. W. Nam. "Single photon source characterization with a superconducting single photon detector". *Opt. Express* **13**, 10846 (2005).

[195] C. M. Natarajan. *Superconducting Nanowire Single-Photon Detectors for Advanced Photon-Counting Applications*. Ph.D. thesis, Heriot-Watt University (2011).

[196] C. M. Natarajan, M. G. Tanner, and R. H. Hadfield. "Superconducting nanowire single-photon detectors - physics and applications". *Supercond. Sci. Technol.* **25**, 063001 (2012).

[197] G. Lepert. *Cavity Quantum Electrodynamics and Wave-Particle Duality*. MSc, Imperial College London (2008).

[198] R. Hubbard, Y. B. Ovchinnikov, J. Hayes, D. J. Richardson, Y. J. Fu, S. D. Lin, P. See, and A. G. Sinclair. "Wide spectral range confocal microscope based on endlessly single-mode fiber". *Opt. Express* **18**, 18811–9 (2010).

[199] C. Santori, D. Fattal, J. Vuckovic, G. S. Solomon, and Y. Yamamoto. "Single-photon generation with InAs quantum dots". *New J. Phys.* **6**, 89 (2004).

[200] ITU. "ITU-T recommendation G.694.1: Spectral grids for WDM applications: DWDM frequency grid". Tech. Rep., International Telecommunication Union (2002).

[201] ITU. "ITU-T recommendation G.694.2: Spectral grids for WDM applications: CWDM frequency grid". Tech. Rep., International Telecommunication Union (2003).

[202] T. Tawara, H. Kamada, T. Tanabe, T. Sogawa, H. Okamoto, P. Yao, P. Pathak, and S. Hughes. "Cavity-QED assisted attraction between a cavity mode and an exciton mode in a planar photonic-crystal cavity". *Opt. Express* **18**, 2719 (2010).

[203] S. Webster. *NPL Low Drift Etalon Product Manual*. National Physical Laboratory (2002).

[204] A. E. Siegman. *Lasers* (University Science Books, 1986).

[205] "HPFS fused silica standard grade product sheet". Tech. Rep., Corning Incorporated (2003).

[206] "TIE-37: Thermal expansion of Zerodur". Tech. Rep., Schott (2006).

[207] Kaye and Laby. "Tables of physical & chemical constants (16th edition 1995) 2.5.7 Refractive index of gases. Kaye & Laby online." (2005). Version 1.0.

[208] LaserOptik GmbH (2012). *Private communication.*

[209] D. R. M. Crooks, G. Cagnoli, M. M. Fejer, G. Harry, J. Hough, B. T. Khuri-Yakub, S. Penn, R. Route, S. Rowan, P. H. Sneddon, I. O. Wygant, and G. G. Yaralioglu. "Experimental measurements of mechanical dissipation associated with dielectric coatings formed using SiO_2, Ta_2O_5 and Al_2O_3". *Classical and Quantum Gravity* **23**, 4953 (2006).

[210] E. S. Zouboulis and M. Grimsditch. "Refractive index and elastic properties of single-crystal corundum up to 2100 K". *J. Appl. Phys.* **70**, 772 (1991).

[211] C. R. Fitzpatrick, C. M. Natarajan, R. E. Warburton, G. S. Buller, B. Baek, S. W. Nam, S. Miki, Z. Wang, M. Sasaki, A. G. Sinclair, and R. H. Hadfield. "A superconducting nanowire single-photon detector system for single-photon source characterization". *Proc. SPIE* **7681**, 76810H (2010).

[212] A. J. Bennett, D. C. Unitt, A. J. Shields, P. Atkinson, and D. A. Ritchie. "Influence of exciton dynamics on the interference of two photons from a microcavity single-photon source". *Opt. Express* **13**, 7772–8 (2005).